

Universidade Estadual de Campinas

Instituto de Química

SAULO DO AMARAL CARMINATI

SURFACE MODIFICATION OF METAL OXIDE PHOTOELECTRODES FOR ENHANCED WATER SPLITTING EFFICIENCY

MODIFICAÇÃO DA SUPERFÍCIE DE FOTOELETRODOS DE ÓXIDOS METÁLICOS NA MELHORA DA EFICIÊNCIA DA QUEBRA DA MOLÉCULA DE ÁGUA

Campinas 2020

SAULO DO AMARAL CARMINATI

SURFACE MODIFICATION OF METAL OXIDE PHOTOELECTRODES FOR ENHANCED WATER SPLITTING EFFICIENCY

MODIFICAÇÃO DA SUPERFÍCIE DE FOTOELETRODOS DE ÓXIDOS METÁLICOS NA MELHORA DA EFICIÊNCIA DA QUEBRA DA MOLÉCULA DE ÁGUA

Tese de Doutorado apresentada ao Instituto de Química da Universidade Estadual de Campinas como parte dos requisitos exigidos para a obtenção do título de Doutor em Ciências

Doctor´s Thesis presented to the Institute of Chemistry of the University of Campinas as part of the requirements to obtain the title of Doctor in Sciences.

Supervisor: Dra. Ana Flavia Nogueira

O arquivo digital corresponde à versão final da Tese defendida pelo aluno Saulo do Amaral Carminati e orientada pela Profa. Dra. Ana Flavia Nogueira

CAMPINAS

2020

Ficha catalográfica
Universidade Estadual de Campinas
Biblioteca do Instituto de Química
Simone Luiz Alves - CRB 8/9094

C212s

Carminati, Saulo do Amaral, 1989-
Surface modification of metal oxide photoelectrodes for enhanced water splitting efficiency / Saulo do Amaral Carminati. – Campinas, SP : [s.n.], 2020.

Orientador: Ana Flavia Nogueira.
Tese (doutorado) – Universidade Estadual de Campinas, Instituto de Química.

1. Óxidos metálicos. 2. Fotólise da água. 3. Hematita. 4. Grafeno. I. Nogueira, Ana Flavia, 1973-. II. Universidade Estadual de Campinas. Instituto de Química. III. Título.

Informações para Biblioteca Digital

Título em outro idioma: Modificação da superfície de fotoeletrodos de óxidos metálicos na melhora da eficiência da quebra da molécula de água
Palavras-chave em inglês:
Metallic oxides
Water photolysis
Hematite
Graphene
Área de concentração: Química Inorgânica
Titulação: Doutor em Ciências
Banca examinadora:
Ana Flavia Nogueira [Orientador]
Lucia Helena Mascaro Sales
Luiz Henrique Dall'Antonia
Juliano Alves Bonacin
Pablo Sebastian Fernandez
Data de defesa: 09-12-2020
Programa de Pós-Graduação: Química

Identificação e informações acadêmicas do(a) aluno(a)
- ORCID do autor: https://orcid.org/0000-0001-8429-8788
- Currículo Lattes do autor: http://lattes.cnpq.br/3422971929227801

BANCA EXAMINADORA

Profa. Dra. Ana Flavia Nogueira (Orientadora)

Profa. Dra. Lucia Helena Mascaro Sales (IQ/UFSCar)

Prof. Dr. Luiz Henrique Dall'Antonia (IQ/UEL)

Prof. Dr. Juliano Alves Bonacin (IQ/UNICAMP)

Prof Dr. Pablo Sebastian Fernandez (IQ/UNICAMP)

A Ata da defesa assinada pelos membros da Comissão Organizadora consta no SIGA/Sistema de Fluxo de Dissertação/Tese e na Secretaria do Programa da Unidade.

Este exemplar corresponde à redação final da Tese de Doutorado defendida pelo aluno **Saulo do Amaral Carminati**, aprovado pela Comissão Julgadora em 09 de dezembro de 2020.

Dedication

To my parents, relatives and friends,

for all their love and support throughout my life.

Acknowledgements

First and foremost, I would like to express my sincere gratitute and appreciation to my supervisor Prof. Ana Flávia Nogueira for accepting me in her group and for all opportunities she provided me during these last 8 years. One thing she taught me and I will always carry with me is to overcome my obstacles and stay above my comfort zone, this is what give you strength to never give up on your goals. Her guidance will undoubtedly play an important role in my future carrer.

My family, which is my love and support. The feeling of having all of you gives me the certain that you represent who I have become in life and the core values I have got.

My deep acknowledgment to my abroad supervisor Prof. Frank E. Osterloh for the best experience and the opportunity to learn the importance of collaborating with different groups. In addition, I also thank my labmates from UC-Davis for the friendship and good times, Alex, Ben, Emilyn, Léo, Rachel, Renato, Ruirui, Xiaoqing, Zeqiong, Zongkai.

A special thanks to my labmates from LNES during this whole time spending together. Andreia, Bruno Ito, Bruno Regata, Bonato, Caio, Carioco, Douglas, Eduar, Eduardo, Emre, Felipe, Flávio, Fran, Gabriela, Ivo, Isabela, Jeann, João Benedetti, João Paulo, Kaká, Lucas, Marco, Marina, Matheus, Nicolau, Raphael, Rodrigo, Saionara, Sivakumar, Stephanie, Wesley, Willian, Terézio. Working with you makes the hard work much easier.

I acknowledge Prof. Flávio Leandro de Souza for his collaboration and the strong support during my master and doctorate.I thank my labmates and friends from UFABC, specially my dear friend Aryanne. My thanks to collaborators from PUC-Rio, Prof. Fernando Lázaro and André Barbosa.

My acknowledgement to LNNano (CNPEM) for providing access to TEM microscope, resulting in recent publications.

And last but not least I acknowledge all collaborators and friends from the Chemistry Institute of UNICAMP, Prof. Juliano, Prof. Pablo, Prof. Claudia, Bott, Miguel, Pãmyla and employees.

This study was financed by the brazilian agency Fundação de Amparo à Pesquisa do Estado de São Paulo (FAPESP #grant 2015/23775-3 and 2016/23178-8).

This study was financed in part by the Coordenação de Aperfeiçoamento de Pessoal de Nível Superior - Brasil (CAPES) – Finance Code 001.

Resumo

Dentre muitos semicondutores estudados para a separação fotoeletroquímica da água, a hematita (α-Fe_2O_3) é considerada um semicondutor promissor para uso como fotoanodo devido às suas propriedades vantajosas, como abundância, absorção de luz na região do visível, estabilidade em meio alcalino e baixa toxicidade. Entretanto, este semicondutor apresenta várias desvantagens, como o curto comprimento de difusão dos buraco, lenta cinética de oxidação da água e baixa mobilidade dos portadores minoritários, o que leva a uma rápida recombinação dos portadores de carga. No intuito de superar essas deficiências, a modificação da superfície de filmes de α-Fe_2O_3 com grafeno, um ótimo material com propriedades condutoras, mostra ser uma alternativa promissora. Para isso, os fotoanodos de α-Fe_2O_3 foram modificados com grafeno de camada única (SLG – *single layer graphene*) e uma investigação detalhada sobre a melhora das propriedades fotoeletroquímicas foi abordada. O grafeno foi sintetizado por deposição química a vapor (CVD) e transferido para a superfície do fotoanodo de α-Fe_2O_3. O papel do grafeno como sobreposição no desempenho fotoeletroquímico do fotoanodo de α-Fe_2O_3/SLG foi investigado através do estudo da dinâmica dos portadores de carga combinando as técnicas de espectroscopia de absorção transiente (TAS) e espectroscopia de fotovoltagem de superfície (SPS).

Na segunda parte, será discutida a incorporação do hexacianoferrato de cobalto (Co-NC-Fe) como eletrocatalisador com diferentes estados de oxidação do ferro (Fe^{II} e Fe^{III}) em fotoanodos de α-Fe_2O_3. Uma investigação detalhada usando técnicas *in-situ* (UV-Vis e FTIR) foi realizada para entender os aspectos fundamentais das reações químicas durante a caracterização em pH neutro. Os fotoanodos de α-Fe_2O_3/Co-NC-Fe apresentaram um maior desempenho fotoeletroquímico em comparação com os materiais individuais, onde verificou-se a dependência dos estados de oxidação dos materiais em diferentes potenciais aplicados.

Na terceira parte e última parte, o vanadato de bismuto ($BiVO_4$) foi o semicondutor usado para a reação de evolução de oxigênio (OER). O $BiVO_4$ tem atraído enorme atenção para aplicações fotocatalíticas devido às suas muitas vantagens como semicondutor para OER. Entretanto, a rápida recombinação dos pares elétron-buraco ainda é uma de suas maiores desvantagens. Para contornar essa desvantagem, foram utilizados passivadores de superfície para então melhorar a separação de cargas. A incorporação de SnO_2 como uma camada fina de revestimento sobre a superfície de $BiVO_4$ para a evolução de O_2 foi realizada. O material $BiVO_4$@SnO_2 apresentou efeito benéfico na evolução de O_2 em relação ao material puro, resultando em 490 µmol após 6h de irradiação. As análises de TAS e SPS indicam uma eficiente separação e transporte de portadores de carga por meio da passivação da superfície do $BiVO_4$, mostrando resultados promissores para estudos futuros.

Abstract

Among many semiconductors studied for photoelectrochemical (PEC) water splitting, hematite (α-Fe_2O_3) has emerged as a promising candidate as photoanode due to its advantageous properties such as abundance, visible light absorption, stability in alkaline media and non-toxicity. Despite these many advantages, α-Fe_2O_3 presents several drawbacks such as short diffusion length of minority carriers, sluggish water oxidation kinetics and low minority carriers mobility, leading to fast charge carrier recombination. In the first part, to overcome these shortcomings, α-Fe_2O_3 photoanodes were modified with single layer graphene (SLG) and a detailed investigation on improved photoelectrochemical (PEC) properties has been addressed. The role of the SLG as overlayer on enhanced PEC performance of α-Fe_2O_3/SLG photoanodes was investigated. Herein, the charge carrier dynamics were investigated combining transient absorption spectroscopy (TAS) and surface photovoltage spectroscopy (SPS).

In the second part, it is discussed the incorporation of cobalt hexacyanoferrate (Co-NC-Fe) with different iron oxidation states (Fe^{II} and Fe^{III}) on α-Fe_2O_3 nanorods photoanodes. Co-NC-Fe which has an analogous structure to Prussian Blue (PB), has shown good electrocatalytic activity owing to its both fundamental and practical perspectives. A detailed investigation using *in-situ* techniques (UV-Vis and FTIR) was carried out to understand the fundamental aspects of chemical reactions during PEC characterization under neutral pH. The α-Fe_2O_3/Co-NC-Fe photoanodes showed higher photoelectrochemical performance as well as photocurrent density, compared to the individual materials which was found to be dependent of the oxidation states of the materials at different applied potentials.

In the third part, bismuth vanadate ($BiVO_4$) was the semiconductor for oxygen evolution reaction (OER). $BiVO_4$ has attracted substantial attention for photocatalytic applications owing to its many advantages as semiconductor for OER. Despite promising characteristics, the fast electron-hole pairs recombination is still one of its biggest drawbacks. The use of conformal layers in order to minimize such limitation and to improve charge separation was the aim of this work. Herein, the incorporation of SnO_2 as a conformal coating layer over the $BiVO_4$ surface for O_2 evolution was carried out. The $BiVO_4$@SnO_2 photocatalyst showed the beneficial effect in O_2 evolution compared to the pristine material, resulting in 490 µmol after 6h of irradiation. TAS and SPS measurements indicate enhanced charge carrier separation and transport by passivating $BiVO_4$ with SnO_2 thin layer, showing promising results for further studies.

List of Figures

Figure 1: a) Local temperatures in 2019 relative to the average temperature to the period 1951-1980 and b) annual total CO_2 emissions by world region. **23**

Figure 2: Global greenhouse gas emissions in 2014, segmented by sector and by leading countries. Data provided by CAIT (Climate Data Explorer). **24**

Figure 1.1: Thermodynamics of a) uphill and b) downhill processes in photocatalysis. **27**

Figure 1.2: Schematic illustration of a) a particulate semiconductor water splitting, b) b) oxidation and reduction of water taking place at single particle and c) PEC water splitting cell depiciting the photoanode (left) and the Pt wire as counter electrode (right). **29**

Figure 1.3: Band energy positions diagram of most semiconductors in contact with aqueous electrolyte at pH = 0 relative to NHE. The redox potentials of HER and OER are compared to the VB and BC position of the semiconductors. **30**

Figure 1.4: Overall outlook of the photocatalytic water splitting process. The numbers indicate the preferential order for succesfull overal water splitting. **31**

Figure 1.5: Energy diagram of α-Fe_2O_3 and the electrolyte under a) isolated and b) equilibrated conditions. After reaching equilibrium, space charge layer is created. ...**32**

Figure 1.6: Schematic illustration of energy diagrams of α-Fe_2O_3 photoanodes at a) 0.55 V_{RHE} and b) 1.3 V_{RHE}. Purple arrow indicate charge carrier recombination; r-SS indicates recombination surface states. **34**

Figure 1.7: The uni cell (left) of αFe_2O_3 illustrates the octahedral face-sharing Fe_2O_9 dimers forming a long chain tn the c direction. The electrostatic repulsion of the Fe^{3+} cations is detailed in the right. **35**

Figure 1.8: a) Polycrystalline nanosized α-Fe_2O_3 and b) α-Fe_2O_3 nanorods vertically oriented onto de FTO substrate. **37**

Figure 1.9: Electronic bands of an n-type semiconductor as a photoelectrode at different applied bias. **38**

Figure 1.10: a) Schematic PEC system with energy diagram of device based on α-Fe_2O_3 photoanode. The illustration depicts photoexcitation of α-Fe_2O_3 and subsequent processes prior to OER and HER taking place, b) schematic illustration of the

difference between an ideal PEC performance of α-Fe_2O_3 and a real photoanode where main factors dominate the J x V profile. **40**

Figure 1.11: Photocurrent density-pH diagram of α-Fe_2O_3 photoanode under AM 1.5G illumination. **43**

Figure 1.12: Sequential water splitting processes occuring at different time scales. All steps are connected and should be effectively integrated for successful overal water splitting. **44**

Figure 1.13: Schematic illustration of the energy diagrams and processes associated with photogenerated charge carriers in α-Fe_2O_3 photoanodes under illumination and at different applied potentials i) 0.5 V vs RHE, ii) 1.1 V vs RHE and iii 1.6 V vs RHE. **45**

Figure 1.14: Schematic illustration of a) pump-probe transient absorption spectroscopy and b) generation of transient species after short pulse excitation. **46**

Figure 1.15: a) Measurement configuration of SPS plot with b) negative and positive signals and c) a typical spectra (photovoltage signal (△CPD) versus the photon energy (eV)) of α-Fe_2O_3 films with different thickness. **48**

Figure 2.1: Bidimensional structure of graphene monolayer, arranged in an atomic-scale hexagonal lattice made of carbon and b) bands structure of pure, n-type and p-type graphene. **51**

Figure 2.2: Synthesis of rGO from graphite, after GO reduction process. **52**

Figure 2.3: Schematic illustration of hydrothermal synthesis of α-Fe_2O_3 nanorod films onto FTO substrate. **55**

Figure 2.4: Transient absorption spectrometer used for charge carrier dynamics experiments. **58**

Figure 2.5: a) X-ray diffraction patterns of S1, S2 S3 and S4 samples and of the FTO substrate (* denotes the FTO substrate peaks) and b) photographs of S1, S2, S3 and S4 films. **59**

Figure 2.6: Top-view FEG-SEM images of a) S1, b) S2, c) S3 and d) S4 α-Fe_2O_3 samples. **60**

Figure 2.7: Cross-section images of a) S1, b) S2, c) S3 and d) S4 samples depicting their thicknesses. **61**

Figure 2.8: Photocurrent density (mA cm^{-2}) vs V_{RHE} (I-V curves) applied potential of a) S1, b) S2, c) S3 and d) S4 α-Fe_2O_3 photoanodes and e) schematic illustration of front and back illumination on nanorod-based films. **62**

Figure 2.9: a) C 1s deconvolution show C-C bonds with the expected energy of 284.52 eV and 285.98 eV (C-O bonds are due to adsorbed carbonic gas and other carbon oxide residues), b) O 1s does not show any more complex oxidation states and c) XPS full spectrum (survey) of graphene (CVD) film on copper foil. **63**

Figure 2.10: a) FEG-SEM top-view image of α-Fe_2O_3/SLG photoanode; b-c) cross sectional profile FEG-SEM image of the vertically oriented α-Fe_2O_3; d) cross sectional profile FEG-SEM image of the α-Fe_2O_3/SLG photoanode with e-f) EDX mapping spectra (spectrum 1 and 2); g) cross sectional profile FEG-SEM image of the α-Fe_2O_3/SLG photoanode with h-i) EDX mapping spectra (spectrum 3 and 4) **64**

Figure 2.11: a) Raman spectra of α-Fe_2O_3 (black), graphene (red) and α-Fe_2O_3/graphene (blue) films; XPS scans of α-Fe_2O_3 (black) and Fe_2O_3/SLG films (red) of b) Fe 2p core level with pronounced peaks for orbital split of Fe $2p_{1/2}$ and $2p_{3/2}$, c) O 1s and d) survey spectra. **66**

Figure 2.12: a) Photocurrent density vs time measurement at 1.23 V_{RHE} under chopped illumination of graphene onto FTO substrate; b) photocurrent density (mA cm^{-2}) vs. potential curves and c) long-term photocurrent stability over time of α-Fe_2O_3 and α-Fe_2O_3/graphene photoanodes under illumination. All measurements were performed in 1 M NaOH solution (pH = 13.6); d) Nyquist plots in the dark of FTO and SLG deposited on FTO; e) Nyquist and f) Mott-Schottky plots obtained by EIS of α-Fe_2O_3 and α-Fe_2O_3/SLG photoanodes The Mott-Schottky measurements were performed at 1-100 kHz frequency in the dark. **67**

Figure 2.13: a) IPCE plots of α-Fe_2O_3 and α-Fe_2O_3/SLG photoanodes at 1.23 V_{RHE} in 1 M NaOH aqueous solution; transient absorption kinetic decays of b) α-Fe_2O_3 photoanode as a function of applied bias, c) α-Fe_2O_3 and α-Fe_2O_3/SLG photoanodes under 1.2 V_{RHE} of applied bias and d) SPS spectra of α-Fe_2O_3 and α-Fe_2O_3/SLG photoanodes under vacuum conditions. **70**

Figure 2.14: a) Schematic illustration of the PEC cell and b) the charge carrier separation that takes place at the α-Fe_2O_3/SLG photoanode surface. **71**

Figure 3.1: a) Representation of the face-centered cubic unit cell of the Co-NC-Fe ($KCo[Fe(CN)_6]$) and b) schematic view of the crystal structure of low and high vacancy ratio with valence/spin-states. **75**

Figure 3.2: Layer-by-layer method to synthesize α-Fe_2O_3/Co-NC-Fe photoanodes with Fe atoms in their II and III oxidation states; b) illustration of the α-Fe_2O_3 nanorods modified with Co-NC-Fe nanocubes covering their surface. **79**

Figure 3.3: Top-view and cross sectional FEG-SEM images of (a-b) Fe_2O_3, (c-d) α-Fe_2O_3/Co^{II}-NC-Fe^{II} and (e-f) α-Fe_2O_3/Co^{II}-NC-Fe^{III}, respectively. The red and blue marks depict the Fe_2O_3 nanorods and Co-NC-Fe nanocubes, respectively. **81**

Figure 3.4: XPS a) Survey spectra of α-Fe_2O_3/Co-NC-Fe photoanodes and b) Fe 2p; Co 2p of c) α-Fe_2O_3/Co^{II}-NC-Fe^{II} and d) α-Fe_2O_3/Co^{II}-NC-Fe^{III} photoanodes.. .....**83**

Figure 3.5: a) Current-potential profiles of FTO|Co^{II}-NC-Fe^{II} and FTO|Co^{II}-NC-Fe^{III} electrodes in phosphate buffer solution (0.1M KPi); *in-situ* UV-Vis measurements of b) Co^{II}-NC-Fe^{II} and c) Co^{II}-NC-Fe^{III} films. The inset shows the as obtained spectra as a function of applied bias (vs Ag/AgCl). **84**

Figure 3.6: α-Fe_2O_3, α-Fe_2O_3/Co^{II}-NC-Fe^{II} and α-Fe_2O_3/Co^{II}-NC-Fe^{III} electrodes in 0.1 M KPi: a) current-potential profile in the dark and under irradiation and b) under intermittent irradiation.The measurements were performed at a scan rate of 10 mVs^{-1}. **86**

Figure 3.7: Chopped-light chronoamperometry measurements of a) α-Fe_2O_3/Co^{II}-NC-Fe^{II} and b) α-Fe_2O_3/Co^{II}-NC-Fe^{III} photoanodes; J x V curves of c) α-Fe_2O_3/Co^{II}-NC-Fe^{II} and d) α-Fe_2O_3/Co^{II}-NC-Fe^{III} and before and after long-term stability test. **87**

Figure 3.8: *J x V* curves before and after long-term stability of a) α-Fe_2O_3/Co^{II}-NC-Fe^{II} and its (b-c) chopped-light chronoamperometry measurements at different applied potentials (0.1 - 1.2 $V_{Ag/AgCl}$); the same measurements carried out for (d-f) α-Fe_2O_3/Co^{II}-NC-Fe^{III} photoanode. Figures c and f represent the magnification of figures b and e, respectively, and show the spikes associated with charge carriers recombination at pH 7. .....**88**

Figure 3.9: Dynamics of photogenerated holes (probed at 650 nm) in a) α-Fe_2O_3, b) α-Fe_2O_3/Co^{II}-NC-Fe^{II} and c) α-Fe_2O_3/Co^{II}-NC-Fe^{III} photoanodes; d) transient absorption decay of the materials at 0.62 $V_{Ag/AgCl}$ (1.23 V_{RHE}). The measurements were carried out in the absence or under 0.62 $V_{Ag/AgCl}$ of applied bias in 0.1 M KPi (pH 7). **89**

Figure 3.10: Cyclic voltammetry (CV) curves of c) Co^{II}-NC-Fe^{II}, Co^{II}-NC-Fe^{III}, e) α-Fe_2O_3/Co^{II}-NC-Fe^{II} and f) α-Fe_2O_3/Co^{II}-NC-Fe^{III} photoanodes in 0.1 M KPi. All CV curves depict the first (1^{st}) and tenth (10^{th}) cycles. **91**

Figure 3.11: *In-situ* FTIR spectra of a) Co^{II}-NC-Fe^{II}, b) α-Fe_2O_3/Co^{II}-NC-Fe^{II}, c) Co^{II}-NC-Fe^{III} and d) α-Fe_2O_3/Co^{II}-NC-Fe^{III} in the dark. The spectra were recorded in the range of -0.1 to 1.0 V vs Ag/AgCl (1 mV s^{-1}) in 0.1 M KPi (pH 7).The circles depict

the appearance of the Co^{III}/Fe^{II} (rose), Co^{II}/Fe^{III} (green) and Co^{III}/Fe^{III} (yellow) oxidized species as a function of applied bias. 92

Figure 3.12: *In-situ* FTIR spectra of a) α-Fe_2O_3/Co^{II}-NC-Fe^{II} and b) α-Fe_2O_3/Co^{II}-NC-Fe^{III} under light illumination. The measurements were carried out for materials deposited onto gold substrates. 94

Figure 3.13: Schematic illustration of charge carrier transport in α-Fe_2O_3/Co^{II}-NC-Fe^{III} photoanode and an energy diagram depicting the three proposed reactions during PEC characterization, one of which is the photoinduced electron transfer from the CB of α-Fe_2O_3 to $[Fe(CN)_6]^{3-}$ in Co-NC-Fe. The band edge positions are shown at pH = 0 relative to NHE. 96

Figure 4.1: Bands structure of tetragonal zircon-type $BiVO_4$ and monoclinic scheelite $BiVO_4$. 101

Figure 4.2: a) J-V curves of an photoanode before and after surface passivation, b) surface defect states in the band strutcutre, facilitating charge recombination, c) deposition of an OER catalyst layer, promoting facile hole transfer and d) deposition of a very thin npncatalytic surface layer to passivate surface states, supressing charge carrier recombination at the surface for improving water oxidation. 103

Figure 4.3: HRTEM images of a) the bare α-Fe_2O_3 and b) FeOOH/α-Fe_2O_3 thin films. The thickness of the amorphous FeOOH layer is about 2 nm; c) current density-potential curves recorded at pH 13.6 under 1 sun simulates solar light irradiation. 104

Figure 4.4: Illustration of the monoclinic BiVO4 crystal before and after SnO_2 conformal layer deposition. {010} and {110} depict the dual-facet $BiVO_4$. The powder materials were used for OER and for SPS and TAS measurements as photoanodes on cleaned FTO. 106

Figure 4.5: TEM images of (a-b) unmodified $BiVO_4$ and (c-d) $BiVO_4$@SnO_2 3% samples. The inset in c) shows the zoomed-in image; e) FEG-SEM image and f) EDX spectrum of $BiVO_4$@SnO_2 3% sample. 109

Figure 4.6: a) XRD diffraction peaks and b) Kubelka-Munk converted UV/Vis diffuse reflectance plots of unmodified $BiVO_4$ and $BiVO_4$@SnO_2 samples on FTO substrate 111

Figure 4.7: Time courses of oxygen evolution from O_2 evolution over 70 mg of $BiVO_4$ and $BiVO_4$@SnO_2 0.5, 1.0, and 3.0% samples suspended in 100 mL of 0.05 M $AgNO_3$ solution under stirring. The suspension was irradiated with a 300 W Xe arc lamp in the presence of a 0.22 M $NaNO_2$ UV filter (λ > 400 nm). 112

Figure 4.8: Chopped linear sweep photocurrent density vs potential of a) unmodified $BiVO_4$,b) $BiVO_4$@SnO_2 0.5%, c) $BiVO_4$@SnO_2 1% and d) $BiVO_4$@SnO_2 3% photoanodes. The measurements were carried out in 0.1 M KPi electrolyte (pH 7), Scan rate: 10 mVs^{-1}. The values illustrated in the spectra indicate the photocurrent density obtained at 0.62 V (vs Ag/AgCl) corresponded to 1.23 V (vs RHE). **113**

Figure 4.9: a) SPS spectra of unmodified $BiVO_4$, $BiVO_4$@SnO_2 1% and $BiVO_4$@SnO_2 3% under vaccum conditions. The films were prepared by drop-casting an aqueous suspension containing the particles onto FTO substrate. Transient absorption spectra of b) unmodified $BiVO_4$ and $BiVO_4$@SnO_2 1% and 3% in the absence of an applied bias, c) at 1.23 V_{RHE} for $BiVO_4$ and $BiVO_4$@SnO_2 1% and d) for $BiVO_4$@SnO_2 1% without applied bias and at 1.23 V_{RHE}. **114**

Figure A1: Top-view FEG-SEM images of a) the vertically oriented α-Fe_2O_3 and b) α-Fe_2O_3/graphene films; c) UV-Vis spectra of α-Fe_2O_3 and α-Fe_2O_3/graphene films. **140**

Figure B1: EDX spectra of α-Fe_2O_3/Co^{II}-NC-Fe^{II} at different regions of the cross-sectional profile. **141**

Figure B2: EDX spectra of α-Fe_2O_3/Co^{II}-NC-Fe^{III} at different regions of the cross-sectional profile. **142**

Figure B3: XPS spectra of α-Fe_2O_3/Co^{II}-NC-Fe^{II}: a) C 1s and b) N 1s and α-Fe_2O_3/Co^{II}-NC-Fe^{III}: c) C 1s and d) N 1s. **143**

Figure B4: IPCE plots of α-Fe_2O_3, α-Fe_2O_3/Co-NC-Fe^{II}, α-Fe_2O_3/Co-NC-Fe^{III} photoanodes recorded at 0.62 V vs Ag/AgCl in 0.1 M KPi aqueous solution. **..... 144**

Figure B5: Cyclic voltammograms in the dark of a) Co^{II}-NC-Fe^{II} and Co^{II}-NC-Fe^{III} All measurents were carried out on gold substrates; *In-situ* FTIR spectra of c) Co^{II}-NC-Fe^{II} and d) Co^{II}-NC-Fe^{III}. The spectra were recorded in the dark from -0.1 to 1.0 V vs Ag/AgCl (1 mV s^{-1}). CV and in-situ FTIR measurements were carried out in 0.1 M KPi. **145**

Figure B6: *In-situ* FTIR spectra of a) Co^{II}-NC-Fe^{II}, b) α-Fe_2O_3/Co^{II}-NC-Fe^{II}, c) Co^{II}-NC-Fe^{III} and d) α-Fe_2O_3/Co^{II}-NC-Fe^{III} in 0.1 M KPi. All the spectra were recorded in the range of 2200-2000 cm^{-1}. The negative signals correpond to formed oxidized species whereas positive signals correspond to consumed species as function of applied bias. **146**

Figure B7: FTIR spectra of the a) $K_3Fe(CN)_6$ and $K_4Fe(CN)_6.3H_2O$ precursors salts depicting the formation of Co^{III}/Fe^{II} at lower potentials b) Co^{II}-NC-Fe^{II} and c) Co^{II}-NC-Fe^{III} in the dark and under light illumination in the absence of applied bias. **147**

Figure B8: In-situ FTIR spectra of a) α-Fe_2O_3/Co^{II}-NC-Fe^{II} depicting the formation of Co^{III}/Fe^{II} at lower potentials and of b) α-Fe_2O_3/Co^{II}-NC-Fe^{III} at 1.0 V with 5 subsequent spectra at the same potential. **148**

Figure C1: a) FEG-SEM image of the as-prepared $BiVO_4$ and b) schematic illustration of the truncated bipyramid and platelike geometries of $BiVO_4$ with their {010} exposed facet. **149**

Figure C2: (a-f) TEM images of unmodified $BiVO_4$ depiciting its smooth surface. **150**

Figure C3: (a-f) TEM images of $BiVO_4$@SnO_2 3% depiciting the thin SnO_2 conformal layer over $BiVO_4$ surface. **151**

Figure C4: FEG-SEM image combined with EDX for element mapping on $BiVO_4$@SnO_2 3% photocatyst. **152**

Figure C5: Related element mapping images for Bi, O, V and Sn atoms of $BiVO_4$@SnO_2 3% photocatalyst. **153**

List of Tables

Table 1: Precursors amount in the synthesis of α-Fe_2O_3 nanorod films varying their thickness. **55**

Table 2: ν$C{\equiv}N$ stretching mode frequencies[a] of each material. The measurements were carried out in dark conditions. **93**

List of Abbreviations

AM	Air mass
CB	Conduction band
CE	Counter electrode
CPD	Contact potential difference
CV	Cyclic voltammetry
CVD	Chemical vapour deposition
EDX	Energy-dispersive X-ray spectroscopy
EIS	Electrochemical impedance spectroscopy
ET	Electron injection
FEG-SEM	Field emission gun scanning electron microscope
FTIR	Fourier-transform infrared spectroscopy
FTO	Fluorine doped Tin oxide
HER	Hydrogen evolution reaction
HT	Hole injection
IPCE	Incident to photon-to-current efficiency
J-V	Current x voltage
LMCT	Ligand-to-metal charge transfer
MLCT	Metal-to-ligand charge transfer
NHE	Normal hydrogen electrode
OD	Optical difference

OER	Oxygen evolution reaction
PB	Prussian blue
PEC	Photoelectrochemicall cell
POL	Polarization of electron-hole pairs
PU	Polyurethane
RE	Reference electrode
rGO	Reduced graphene oxide
RHE	Reversible hydrogen electrode
SLG	Single layer graphene
SPS	Surface photovoltage spectroscopy
STH	Solay-to-hydrogen efficiency
TAS	Transient absorption spectroscopy
TEM	Transmission electron microscopy
VB	Valence Band
WE	Working electrode
WOC	Water oxidation catalyst
XPS	X-ray photoelectron spectroscopy
XRD	X-ray diffraction

List of Symbols

E_{Fn}	quasi Fermi energy level for electrons
E_{Fp}	quasi Fermi energy level for holes
E_{G}	band gap energy
j_{max}	maximum photocurrent
N_{D}	donor density
η_{tr}	fraction of photogenerated charge carriers
V_{fb}	flatband potential
V_{onset}	onset potential
W	depletion layer width

Contents

Introduction **23**

Chapter 1 ..... **26**

1.1 General aspects of water splitting: materials and advanced techniques for characterization 27

1.1.1 Water splitting 27

1.1.2 Semiconductor/Electrolyte interface 32

1.1.3 Charge carrier separation and transport 33

1.1.4 Surface states and Fermi level pinning 33

1.1.5 Hematite (α-Fe_2O_3) 35

1.1.6 Important considerations into photoelectrochemical water splitting on α-Fe_2O_3, drawbacks and challenges 38

1.1.7 pH-dependent performance of α-Fe_2O_3 photoanodes 42

1.1.8 Charge recombination in α-Fe_2O_3 photoanodes 43

1.2 Advances techniques for charge carrier characterization 46

1.2.1 Transient absorption spectroscopy (TAS) for evaluationg charge carrier dynamics 46

1.2.1 Surface photovoltage spectroscopy (SPS) 47

Chapter 2 Unraveling the role of single layer graphene as overlayer on hematite photoanodes **49**

2.1 Introduction **50**

2.1. Graphene 47

2.2. Experimental 55

2.2.1 α-Fe_2O_3 nanorod films preparation 56

2.2.2 Synthesis of single layer graphene (SLG) 56

2.2.3 SLG deposition onto α-Fe_2O_3 nanorods films 56

2.2.4 Structural characterization 56

2.2.5 Photoelectrochemical (PEC) characterization 57

2.2.6 Transient absorption spectroscopy (TAS) measurements 58

2.2.7 Surface photovoltage spesctroscopy (SPS) measurements 59
2.3. Results and discussion 59
2.4 Partial conclusion 72
Chapter 3 Surface modification of α-Fe_2O_3 photoanodes with cobalt hexacyanoferrate (Co-NC-Fe): The role of the mixed oxidized states on the enhancement of PEC performance 73
3.1.1 Prussian Blue (PB) 74
3.1.2 Cobalt Hexacyanoferrate (Co-NC-Fe) 74
3.1.3 α-Fe_2O_3/Co-NC-Fe compound for PEC water splitting 76
3.2 Experimental 79
3.2.1 Synthesis of α-Fe_2O_3 nanorods and α-Fe_2O_3/Co-NC-Fe films 79
3.2.2 Characterization of the materials 80
3.2.3 PEC characterization 80
3.2.4 TAS measurements 80
3.2.5 *In-situ* characterization: UV-Vis and FTIR spectroscopy measurements 80
3.3 Results and discussion 81
3.4 Partial conclusion 97
Chapter 4 SnO_2 as thin conformal layer over BiVO4 surface for enhanced charge carrier separation towards O_2 evolution 99
4.1 Introduction 100
4.1.1 Bismuth vanadate ($BiVO_4$) 100
4.1.2 Charge carrier dynamics on $BiVO_4$ 102
4.1.3 Conformal layer coatings 102
4.2 Experimental 106
4.2.1 Synthesis of $BiVO_4$ and $BiVO_4$@SnO_2 particles 106
4.2.2 Materials characterization 107
4.2.3 O_2 evolution reactions 107
4.2.4 Photoelectrochemical measurements 107
4.2.5 Surface photovoltage spesctroscopy (SPS) measurements 108
4.2.6 Transient absorption spectroscopy (TAS) measurements 108

4.3 Results and Discussion 109
4.4 Partial conclusion 116
5 Final remarks 117
6 References 118
7 Appendix 140

Introduction

It is a common sense that the rise in population growth increases the demand for energy, which is mainly met by fossil resources, like coal, natural gas or oil.[1] The consumption of fossil fuels and the emission of CO_2 and other greenhouse gases have increased since the pre-industrial era, presenting one of the world´s most pressing challenges. The combustion of fossil fuels leads to an increase in air pollution, often producing smog highly injurious to human health. Furthermore, a drastic impact to the Earth´s atmosphere is caused by the largely amount of CO_2 emission, which is expected to double by 2050.[2] Such gases block the release of heat back into the space, causing warming of the Earth´s atmosphere.[3] Impacts like rising global temperature (more than 2 °C by 2050), heat waves, heavy rain falls, and increased melting rate of ice in the Artics are the most outcomes by the increased amount of CO_2 release.

Figure 1a shows the temperature report of the global distribution of temperature changes in 2019, relative to the period 1951-1980, data taken from the *Berkeley Earth*,[4] a non-profit source of scientific data focused on land temperature data analysis for climate science. The map shows the combined temperature change across both land and the sea surface, in which at areas near the Poles, temperature changes upward of 3 °C, much more extreme than the rest of the world.

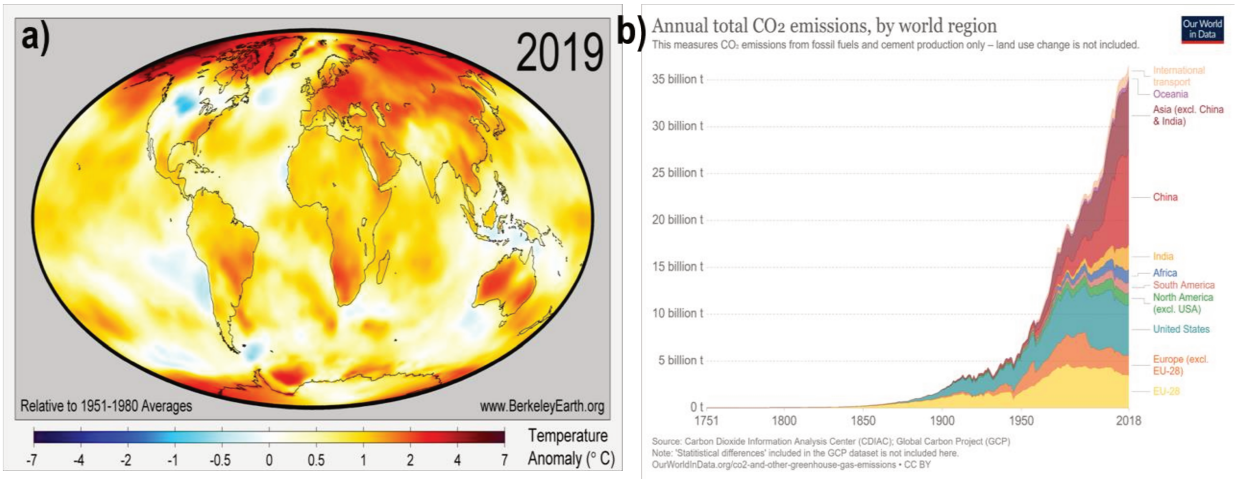


Figure 1: a) Local temperatures in 2019 relative to the average temperature to the period 1951-1980[4] and b) annual total CO_2 emissions by world region.[5]

Figure 1b shows the breakdown of global CO_2 emissions measured in tonnes per year by region, data extracted from *Our World in Data*,[5] a non-profit and scientific online publication that focuses on large global problems. The graphic shows, based on several sources, a significant rise in CO_2 emissions from fossil fuel in the second half of the 20th century across Asia and most notably, China. During the 21st century, plenty

of computer models predict that Earth´s average temperature will raise between 1.8º and 4.0º Celsius if we continue to emit as many as greenhouse gases. This means that we are commited to significant impacts of warming such as ocean warming and sea ice melt.[6] Figure 2 shows the global CO_2 emission, broken down by sector and major countries including Brazil, which varies significantly across countries.[7]

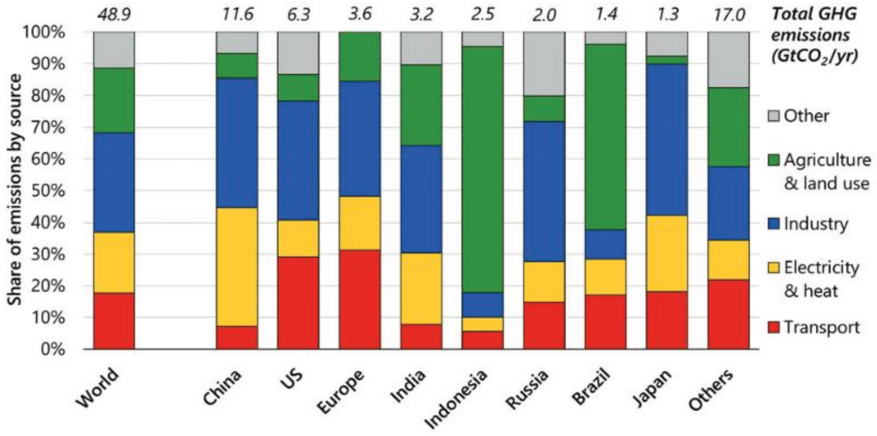


Figure 2: Global greenhouse gas emissions in 2014, segmented by sector and by leading countries. Data provided by CAIT (Climate Data Explorer).[8]

Since the mitigation of CO_2 concentrations is an urgent task and of uttermost importance, there has been an enormous tendency to replace the current energy consumption especially those from non-renewable sources,[9] boosting the interest of the scientific community to increase efforts to seek alternative clean energy solutions. As global warming is becoming an overwhelming problem, hydrogen (H_2) as an alternative clean fuel has gained increasing attention.[10] The recent improvements of technologies for H_2 production have shown great contribution as an attractive option for the deep decarbonisation of global energy systems, considering cost-effective, performance and economic viability.[7] Despite much progress, considerable improvements are still necessary for H_2 to become truly competitive.

Hydrogen fuel is a zero-emission fuel burned with oxygen. It is considered a suitable energy vector to support the transition to a decarbonized energy system in order to meet the emission reduction goals of the Paris Agreement. In a recent report (2019) by the International Energy Agency (IEA), it is estimated that less than 0.7 percent of current hydrogen production comes from renewable sources, resulting in 830 million tonnes of CO_2 per year.[11] At present, roughly 95% of worldwide hydrogen production is done by non-renewable sources such natural gas (48%), oil (30%) steam reforming and coal gasification with water-gas shift (WGS) reaction (18%) and only 4% is obtained by means of water electrolysis.[12]

Hydrogen as a fuel has a strategic importance in the pursuit of low-emission and more sustainable energy system. With high energy yield of 122 kJ/g, which is 2.75 times higher than hydrocarbon fuels, hydrogen is currently being explored for use in combustion engines and fuel-cell electric vehicles.[13] Hydrogen vehicles are available commercially in several countries and of only five years ago, 225 000 fuell cell for home heating systems have been sold. Besides these examples, hydrogen can be used in many segments of industry[14] and electricity sectors,[15] demonstrating its enormous versatility in a wide range of commercial applications.

Solar energy[16] could be a clean and renewable free source of energy that is sustainable and totally inexhaustible to satisfy the goals for hydrogen production. The solar energy that irradiates Earth´s surface (1.3×10^5 TW) greatly exceeds current global human energy consumption (1.6×10^1 TW, 2010).[17] In this concept, solar water splitting process for hydrogen production is potentially attractive when a semiconductor is photo-excited by photons creating electron/hole pairs capable to split water and generate molecular hydrogen (H_2) and oxygen (O_2).[18]

As an ideal alternative, photoelectrochemical (PEC) and photocatalytic (PC) solar energy conversion systems can offer high ability to convert or store electromagnetic energy from the sun in chemical bonds, by splitting water into H_2 and O_2. In an overall water splitting based on PC technology, a photocatalyst is suspended in a reactor with water and the H_2 and O_2 products are produced throughout the entire suspension. On the other hand, in a PEC system,[19] a photoelectrode is manufactured containing the semiconductor material responsible for light absorption to drive water oxidation (photoanode) or proton reduction (photocathode). In this specific case, H_2 and O_2 can be spatially separated at different compartments.

Although, the biggest challenge is to find a proper semiconductor that satisfies all the requirements in order to make it suitable for practical and commercial applications. Among many semiconductors used as photoelectrodes for water oxidation, one can mention α-Fe_2O_3,[17] TiO_2,[20] $BiVO_4$,[21] WO_3[22] and so on. Despite much progress achieved, there is still a need of accurate and deeper information about intrinsic properties of these semiconductors. In this thesis, a comprehensive understanding of the reason for enhanced PEC performance of α-Fe_2O_3 as well as $BiVO_4$ photoelecrodes after surface modification was the main aim of the work.

Chapter 1

In this first chapter, it will be discussed a general introduction of the fundamental aspects of PEC water splitting, summarizing the advantages, drawbacks and goals. The discussions and insights provided here reflect the direction for general photoelectrode developments towards addressing limitations to improve the performances of α-Fe_2O_3-based materials and of other photoelectrode systems. A deeper focus on charge carrier dynamics to better understand the mechanisms that are involved in the performance of such devices is the aim of this work.

Theoretical Background

1.1 General aspects of water splitting: materials and advanced techniques for characterization

1.1.1 Water Splitting

Water splitting is thermodynamically an uphill reaction (Figure 1.1a) accompanied by a large positive change in Gibbs free energy (238 kJ/mol).[23] This means that photosynthetic processes (which include water splitting and CO_2 reduction) are unfavorable and require photochemical energy input to occur, whereas downhill (Figure 1.1b) processes (e.g. oxidation of phenol) are merely accelerated by the catalyst.[24] Considering the feasibility of the global equation of water splitting, the water oxidation reaction is particularly, not only from thermodynamic point of view but also kinetically, arduous to be succesfully achieved since it requires the transfer of four electrons and four protons, turning the seek for a good candidate as a photonode more challenging. The whole process generates two electron/hole pairs for each H_2 molecule (1.23 eV x 2 = 2.36 eV) or four electron/hole pairs for each O_2 molecule (1.23 eV x 4 = 4.92 eV).[23]

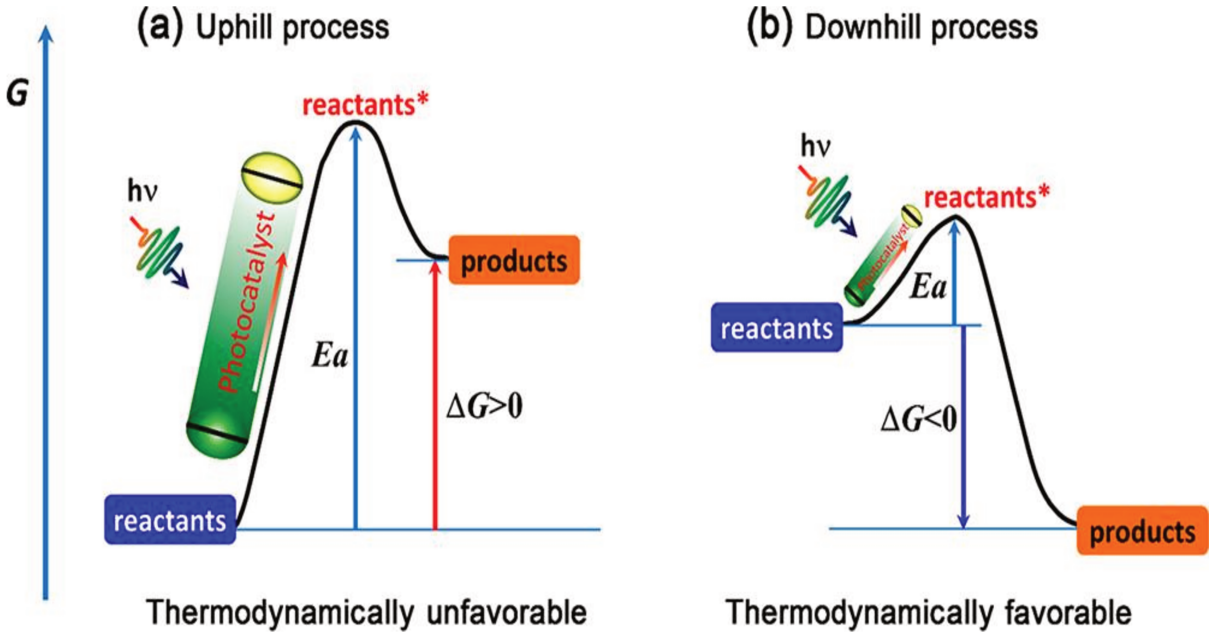


Figure 1.1: Thermodynamics of a) uphill and b) downhill processes in photocatalysis.[24]

When a semiconductor is photoexcited with energy equal or greater than its band gap, electron and hole pairs are created. The electrons (e^-) from the valence band (VB) are excited to the conduction band (CB), leaving holes (h^+) in the VB. The photogenerated electrons and holes cause reduction and oxidation reactions, respectively. To accomplish the overall water splitting, the backward reaction, that is, the water formation from H_2 and O_2, must be strictly inhibited, and meanwhile, the photocatalysts must be stable in the reaction.[25]

There are two pathways to accomplish split of water using a semiconductor, photochemical (PC) and photoelectrochemical (PEC) water splitting. In the former case, particulate suspensions (Figure 1.2a) is the most popular in evaluating the photocatalytic performance, owing to easier instrumentation required. For a typical particle-based system, both reduction and oxidation reactions take place on the surface of the same particle, in close vicinity.[26] Under illumination, if they overcome recombination, the photogenerated electrons and holes migrate to the surface, being spatially separated to drive reduction and oxidation of water (Figure 1.2b)

In the later, a simplistic PEC cell should consist of at least three components, the photoelectrode, the electrolyte and an external electric circuit. PEC water splitting dates back to the early 1970s, when Fujishima and Honda,[27] pioneering researchers on catalysis, developed the first PEC cell for overall water splitting consisting of a singe crystalline TiO_2 (rutile) as photoanode under applied external bias. Typically, in a PEC cell configuration, the photoelectrode (in this case an n-type photoanode) is irradiated by photons whose energy is greater than the band gap, resulting in electrons population in the CB, leaving holes in the VB. The photogenerated electrons migrate to the counter electrode to drive proton reduction, while holes in the VB emerge to the interface to generate oxygen,[26] as depicted in Figure 1.2c.

In this scenario, photoelectrochemical (PEC) water splitting represents an environmentally friendly and sustainable procedure to generate hydrogen fuel and can be described as a more ellegant manner to store solar photons into chemical energy. The advantages of PEC systems include better spatial charge separation, easy control of the reaction pathways and the possibility to generate the products in separate compartments,[26] minimizing products crossover. Additionally, by applying an external bias, semiconductors materials that are not able to perform overall water splitting (e.g. α-Fe_2O_3 and $BiVO_4$) The basic principles of PEC water splitting (Figure 1.2c) include the redox reactions each electrode, represented in the following equations:

$$\text{Photoanode: } 2\ H_2O + 4h^+ \rightarrow\ O_2 + 4H^+, \quad \Delta E^\circ = 0.82\ \text{V vs NHE} \tag{1.1}$$

$$\text{Cathode: } 2\ H^+ + 2e^- \rightarrow H_2, \quad \Delta E^\circ = -0.41\ \text{V vs NHE} \tag{1.2}$$

$$\text{Global Reaction: } H_2O \rightarrow H_2 + \tfrac{1}{2}\ O_2,\ \Delta E^\circ = 1.23\ \text{V vs NHE} \tag{1.3}$$

Equations 1.1-1.3 show that the overall water splitting reaction requires at least 1.23 V to take place.

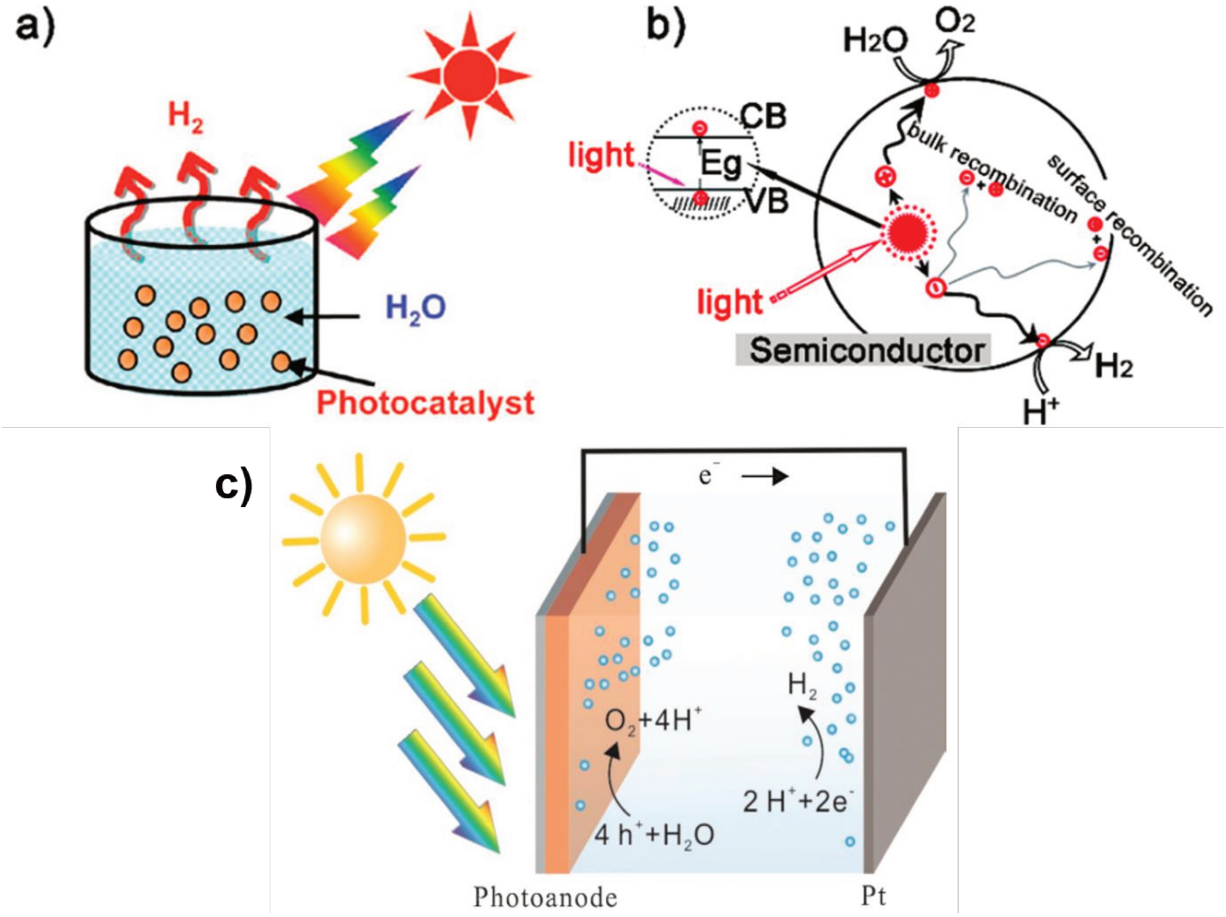


Figure 1.2: Schematic illustration of a) a particulate semiconductor water splitting, b) oxidation and reduction of water taking place at single particle[26] and c) PEC water splitting cell depiciting the photoanode (left) and the Pt wire as counter electrode (right).[28]

To be considered a good candidate for efficient photocatalytic water splitting, a given semiconductor must fulfil some requirements. For overall water splitting, one of the key principles is that i) its conduction and valence bands (BC and BV, respectively) should straddle the oxidation (O_2/H_2O) and reduction (H^+/H_2) potentials of water, which are 0 and +1.23 V *vs.* the normal hydrogen electrode (NHE) at pH 0, respectively. It means that the energy required to drive the overall water-splitting reaction by the electron/hole pairs needs to be at least 1.23 eV.[29] To accomplish this, an efficient semiconductor must have a small band gap with high

absorption coefficient over the entire range of the solar spectrum. Moreover, the semiconductor must have a ii) suitable electronic conductivity and iii) a good electrochemical stability against photocorrosion.[29,30] Figure 1.3 shows the band gap position of different semiconductors compared to HER (hydrogen evolution reaction) and OER (oxygen evolution reaction) redox potentials.

Among many semiconductors, TiO_2 is one of the main used and possess adequate stability, however, due to its large band gap (E_G = 3.2 for anatase TiO_2) it is just able to absorb the UV region, which is only 4% of the solar spectrum. Therefore, a given semiconductor should harvest visible light for effective water splitting.[29] It has been suggested that the semiconductor should have an optimal band gap of 2.03 eV, which lead to solar-to-hydrogen efficiency of 16.8%.

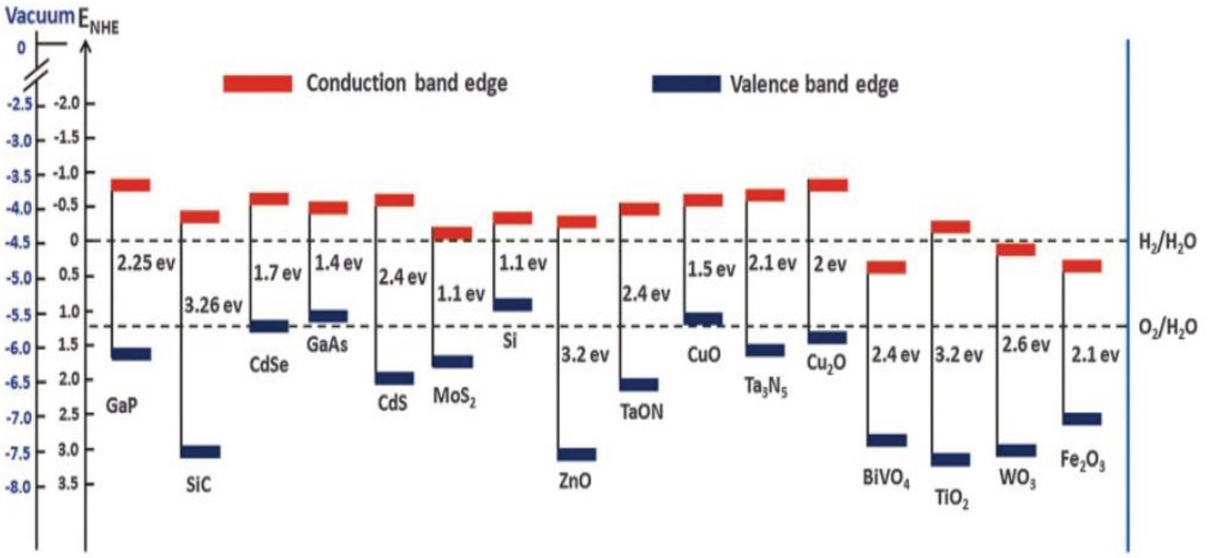


Figure 1.3: Band energy positions diagram of most semiconductors in contact with aqueous electrolyte at pH = 0 relative to NHE. The redox potentials of HER and OER are compared to the VB and BC position of the semiconductors.[17]

In addition to the aforementioned criteria, there are other points to be considered. As depicted in Figure 1.3, the difference between the redox potentials of water oxidation and reduction is of 1.23 V. Hence, the band gap energy of the semiconductor must be, at least 1.76 eV,[31] since only 70% of the band gap energy can contribute to photopotential needed to split water and convert this energy into hydrogen and oxygen.[32]

Prior to evolving O_2 and H_2 during water splitting, there are some crucial chemical and physical steps that occur inside and on the surface of the photoelectrode: i) light absorption, ii) exciton separation, iii) carrier diffusion, iv) charge transport, v) bulk and surface recombination and finally vi) water oxidation and reduction

reactions.[33] The first three steps are strongly dependent on the the structural and electronic parameters of the semiconductor materials. High crystallinity presents a positive effect on the semiconductor activity, since the recombination sites of the charge carriers, resulted from the density of defects, are decreased. In addition, by reducing the particle size of the material, higher photocatalytic activity can be obtained, since the electron/hole pairs migration can be optimized against their short diffusion length.

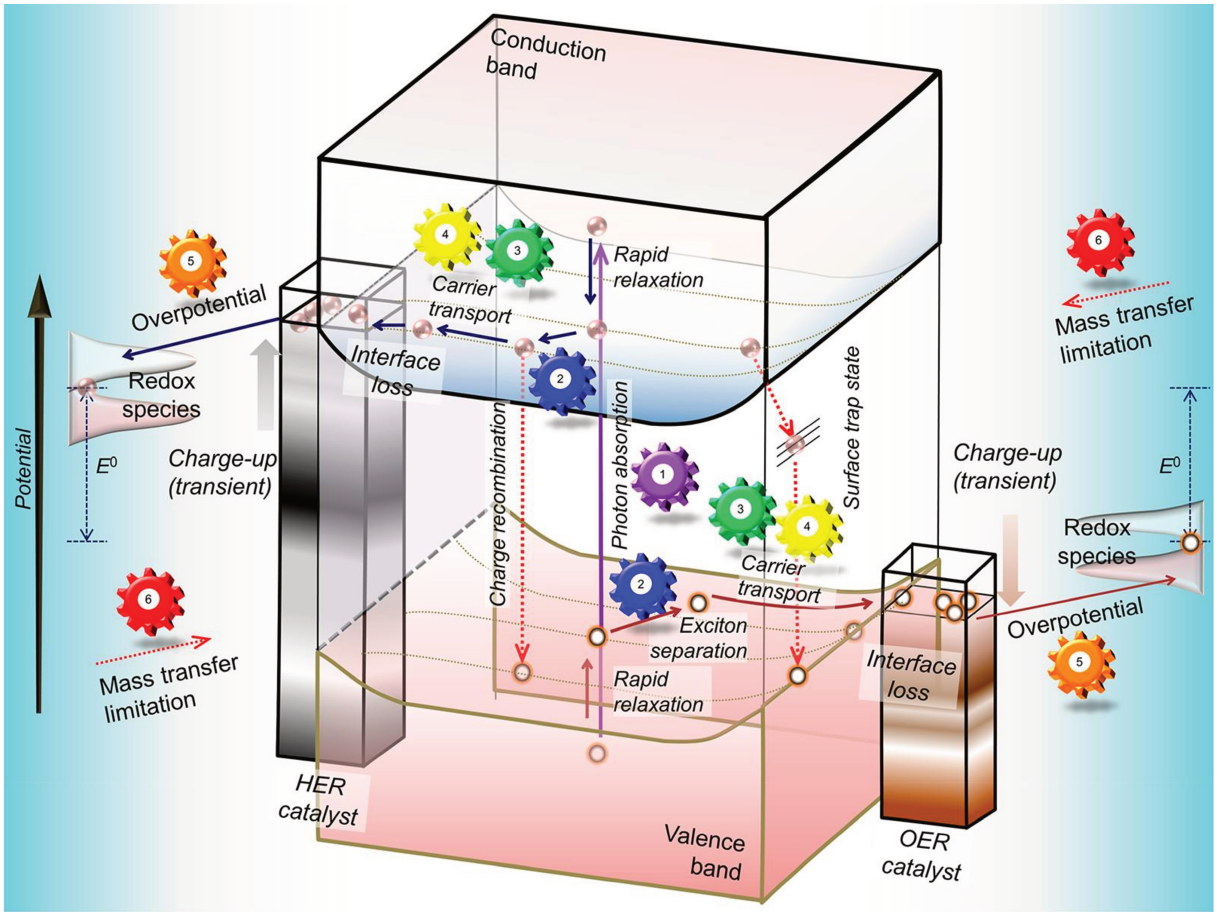


Figure 1.4: Overall outlook of the photocatalytic water splitting process. The numbers indicate the preferential order for succesfull overall water splitting.[33]

Figure 1.4 shows the sequential photocatalytic water splitting process using a single semiconductor, which can be extended to PEC configuration**.** In an ideal perspective, the bottleneck for obtaining efficient charge collection for OER/HER, is that after light absorption, excitons (electron/hole pairs) should be effectively separated into free carriers without experimenting recombination. The paramount importance of enhancing the efficiency of a semiconductor considering these parameters is the key factor for turning promising candidates effective and affordable for practical and commercial applications.

1.1.2 Semiconductor/Electrolyte interface

When a semiconductor is immersed into an electrolyte that contains a redox couple (e.g. H_2O/O_2), an electronic equilibrium of the relative positions of the Fermi levels in the semiconductor and in the redox electrolyte is reached. The Fermi level position with respect to the solution redox potential will depend on the work function and excess of positive or negative charge in the semiconductor electrode. Considering an n-type semiconductor, as α-Fe_2O_3, its Fermi level lies above the Fermi level of the electrolyte and thus, electrons will be transferred to the oxidized species in the solution through the semiconductor/liquid junction (SCLJ) to reach the equilibrium state.[34] Due to removal of electrons from the semiconductor, a depletion layer is formed because the layer is depleted of the majority carriers, region so-called space charge region (SCR) in the semiconductor. The resulted band bending is equal to the original difference between the Fermi levels of the redox electrolyte and the semiconductor. At this point, the Fermi levels in both phases are equal and the equilibrium is reached.

Figure 1.5 shows the band offsets of α-Fe_2O_3 before and after illumination in contact with electrolyte. In Figure 1.5a, since no contact between the two phases exists, the redox potentials are unchanged. After illumination (Figure 1.5b), electron/hole pairs are photogenerated in the semiconductor through light absorption. If the process is operated under open circuit conditions, the Fermi leves of the semiconductor will increase due to the internal photovoltage (V_{ph}). A quasi-Fermi energy level is now necessary to describe the electrochemical potential of the photogenerated electrons and holes.

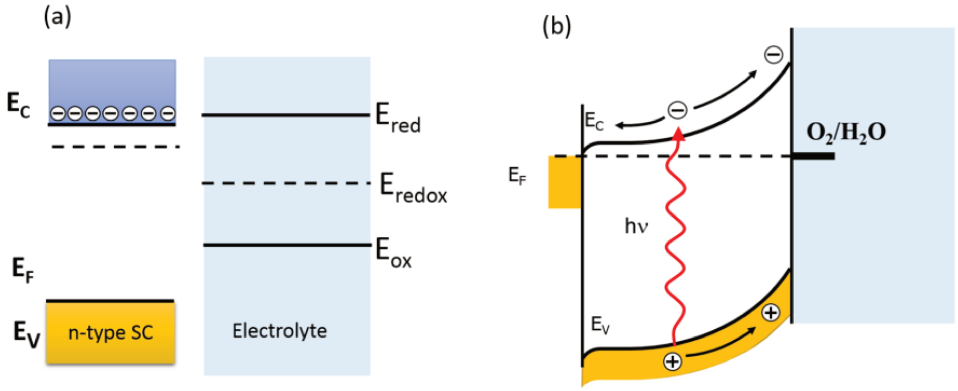


Figure 1.5: Energy diagram of α-Fe_2O_3 and the electrolyte under a) isolated and b) equilibrated conditions. After reaching equilibrium, space charge layer is created.[35]

In a PEC configuration, band bending can also be induced by applying an external potential between the working and the reference electrodes. As the positive bias is increased, the resulted upward band bending turns more pronounced, whereas

by applying a negative bias, the degree of the band bending starts to decrease. After reaching equilibration, the electrode surface will be positively charged, while the solution will have an excess of negative charges at the region so-called Helmholtz layer.[36] This gradient will create a built-in electric field generated in the SLCJ responsible for separating electron-hole pairs and thus generating a photovoltage (V_{ph}) and photocurrent. In the case of an n-type semiconductor as a photoanode, holes (minority carriers) are transferred to the electrolyte in drift mechanism to perform water oxidation, meanwhile electrons participate to proton reduction at the external circuit.

1.1.3 Charge carrier separation and transport

For many semiconductors in which the generated photopotential is not enough, an external bias is necessary to maintain the separation of the charge carriers and complete the reaction. The major problem arises when charge carriers are generated in the bulk and the distance to the back contact is much larger than the diffusion length, leading to facilitated charge carrier recombination. However, the remained charge carriers that did not recombine must overcome thermodynamics and kinetics barrier for an efficient charge transfer. Light-induced electron/hole pairs must be separated to circumvent eventual charge recombination that hamper the extraction of any current from the photogenerated charges.[37] These properties are strongly affected by crystallinity, crystal structure and particle size. Inevitably, an external potential should be applied in order to separate the photogenerated charge carriers and hence, creating a photovoltage and a photocurrent.

1.1.4 Surface States and Fermi Level Pinning

Despite much advantages of many semiconductors, very few of them behave ideally. A challeging problem which arises in this domain is to overcome the surface states effects on the field of semiconductor photoelectrochemistry, which has been under heavy debate.[38] The surface states arise when the periodic crystal symmetry is broken, leaving under-coordinated atoms with dangling bonds,[39] and thus, generating electronic states within the band gap, so-called surface states/mid-gap states.[40] Surface states play a vital role in the kinetics of interfacial reactions at the electrodes during illumination. It turns out that these electronic energy levels resulted from the surface states are susceptible to exchange electrons with the bulk semiconductor and with redox species in electrolyte, affecting the potential distribution across the junction.

In an energy diagram, the surface state is defined by a particular energy (E_{ss}) with surface concentration (N_{ss}).[41] For an n-type semiconductor, as the electrode potential is increased, the Fermi level moves downwards until it matches with E_{ss}. Figure 1.6 shows the energy diagram of α-Fe_2O_3 photoanodes at different applied potentials. At low potential, holes can easily recombine at surface states (r-SS) since they lie just below Fermi level. By increasing potential, r-SS becomes fully depleted and holes can accumulate at the surface to drive water oxidation. By further positive biasing, the surface states alters the electron ocupation of surface states, leading to so-called Fermi level pinning,[34] phenomenon by which the potential drop at the band bending varies much slowly with the applied voltage, becoming stuck in the surface state and giving rise to a fixed barrier height.

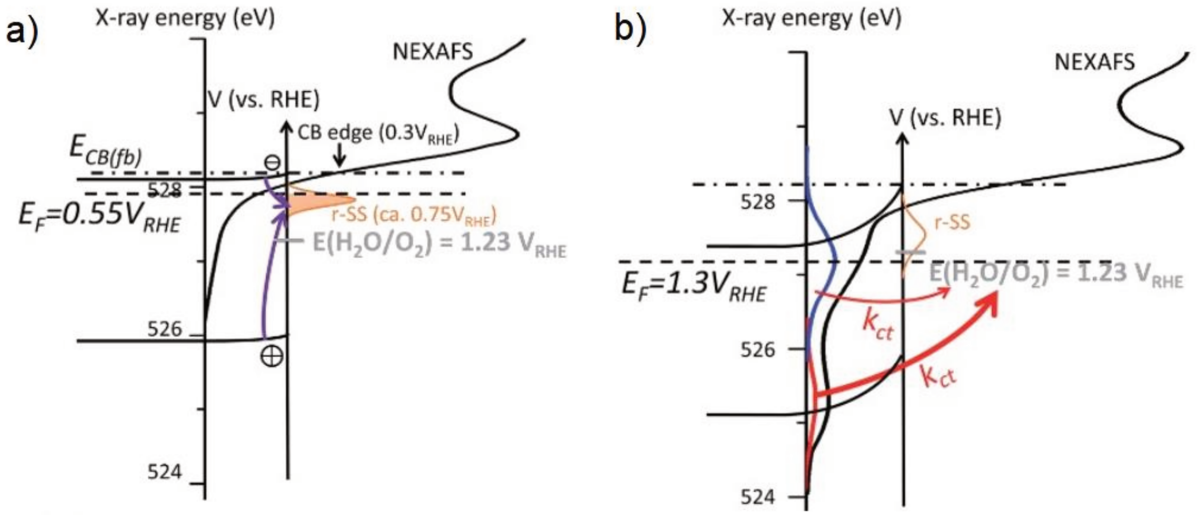


Figure 1.6: Schematic illustration of energy diagrams of α-Fe_2O_3 photoanodes at a) 0.55 V_{RHE} and b) 1.3 V_{RHE}. Purple arrow indicate charge carrier recombination; r-SS indicates recombination surface states.[42]

In order to decrease the surface states effects on the photoactivity of α-Fe_2O_3, the control of the sintering parameters, including temperature and atmosphere make a major contribution to reduce crystal defects, modifying the surface states of the photoelectrodes. By annealing α-Fe_2O_3 photoanodes at high-temperature sintering (~800 °C), Sn dopant diffusion from the FTO substrate into the hematite lattice was found to improved the donor density, increasing photocurrent response.[43] Recently, plenty of researches have been devoted their efforts to the development of efficient photoelectrodes by supressing surface states effects.[44] The impact of surface states on the water oxidation photocatalysis, specially for α-Fe_2O_3, still remains controversial. The improved knowledge of the intrinsic optoelectronic of photoelectrode materials will be important for their technological development.

1.1.5 Hematite (α-Fe_2O_3)

Hematite (α-Fe_2O_3), which is iso-structural with corundum (α-Al_2O_3) is the most thermodynamically stable and common form of iron oxide.[17] In addition, it is the most common form of crystalline iron oxide.[45] Despite being the most used n-type semiconductor as a photoanode for water oxidation, the synthetic α-Fe_2O_3 can be either n-type or p-type, depending on the impurity content and oxygen deficiency in its lattice. For iron oxide in its highest oxidation state, each iron atom has oxidation state of 3+. Hematite is arranged in a corundum structure, where each iron atom has six oxygen neighbors and each oxygen atom has four iron neighbors. The unit cell of α-Fe_2O_3 structure is illustrated in Figure 1.7,[46] in which the structure can be understood as an arranged hexagonal closed-packed lattice along the [001] direction. The electrostatic repulsion of the Fe3+ results in different Fe-O bond lengths.[46]

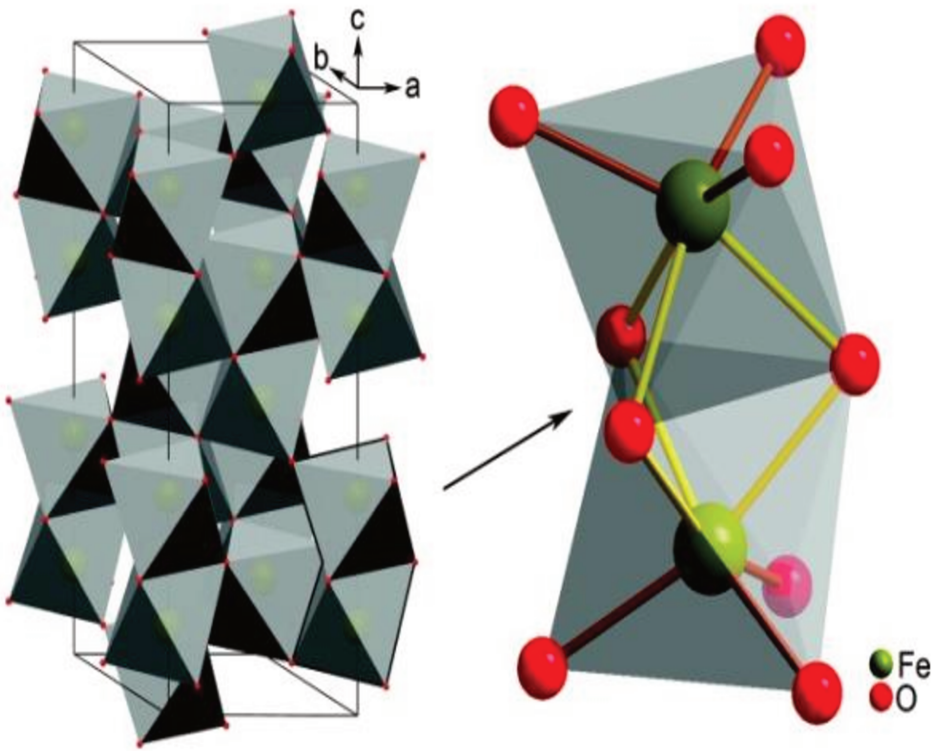


Figure 1.7: The uni cell (left) of αFe_2O_3 illustrates the octahedral face-sharing Fe_2O_9 dimers forming a long chain in the c direction. The electrostatic repulsion of the Fe^{3+} cations is detailed in the right.[47]

Among the myriad of metal oxide semiconductors studied for photoelectrochemical (PEC) water splitting, α-Fe_2O_3, which is an *n*-type material with an optical bandgap energy between 1.9 and 2.2 eV (corresponding to wavelengths of 650 and 560 respectively) depending on the sample preparation technique,[48] has been

emerged as a promising candidate as photoanode. This is due to its advantageous properties such as abundance, visible light absorption, stability in alkaline media and non-toxicity.[17,49–52] Therefore, α-Fe_2O_3 is able to achieve high solar-to-hydrogen (STH) efficiency (theoretical value of 15.5%) and deliver a total photocurrent of 12.6 mA cm^{-2} under AM 1.5G solar irradiation.[53] However, a given semiconductor materials must be $3/\alpha$ thick in order to absorb 95% of the light at this wavelength range, where α is the absorption coefficient. In case of Fe_2O_3, $\alpha = 8 \times 10^4$ cm^{-1} at 550 nm, and thus, the thickness of the photoelectrode must be at least 0.4 µm to convert significant amount of incident energy.

Besides the aforementioned properties and despite the many advantages, α-Fe_2O_3 presents several drawbacks that need to be fully addressed before promoting it for commercialization. As well as for many candidates semiconductors, α-Fe_2O_3 suffers from highly reduced charge transport as the minority carrier diffusion lengths are considerably shorten than the absorption depth of light (micrometer scale). The short hole diffusion length (usually estimated between 1.5 and 5 nm) results in high loss of charge carrier separation efficiency. Additional disadvantages such as incompatible CB for proton reduction, sluggish water oxidation kinetics, low minority carrier mobility (10^{-2} cm^2 V^{-1} s^{-1}) and very short excited-state lifetime (3-10 ps) which lead to a fast charge carrier recombination, are the main factors that limit high photo-activity of α-Fe_2O_3 for water splitting.[54–57] In order to overcome these shortcomings, many efforts have been devoted to improve the PEC performance of α-Fe_2O_3 photoelectrodes such as nanostructuring,[58,59] doping,[60,61] heterojunctions[62,63] and incorporation of carbon materials.[64,65] These strategies have proved their ability to enhance the charge carriers separation and transport in α-Fe_2O_3 photoanodes, increasing photocurrent densities.

In terms of electronic properties, α-Fe_2O_3 has its charge transport *via* polaron hopping,[66] by which the size effect difference between Fe^{2+} and Fe^{3+} ions as well as associated lattice distortion have an important role. Additionally, femtosecond laser spectroscopy studies reveal ultra-fast dynamics of the charge carriers, where electrons recombine within 3 ps.[67] The critical drawback associated with fast charge recombination in α-Fe_2O_3 has been recognized as the main fate of the photogenerated charge carriers in hematite, as the short-lived charge carriers are unlikely to have sufficient time to drive the challenging chemistry of water oxidation.

Morphological control plays a vital role in the pholoelectrochemical performance of many semiconductors.[59] Due to short hole diffusion length in α-Fe_2O_3, only holes within a few nanometers of the electrode/electrolyte interface can be

practical for water oxidation. Considering the difference in the photoelectrochemical behavior between the polycrystalline nanosized α-Fe_2O_3 and α-Fe_2O_3 nanorods vertically oriented onto de FTO substrate (Figure 1.8), not only morphology but even orientation have a significant impact in the photocurrent efficiency. While an inefficient photogenerated charge collection through the polycrystalline nanosized α-Fe_2O_3 at the grain boundaries, one-dimensional (1D) nanorod structure with a preferred crystallographic orientation in [110] direction as well as the absence of significant grain boundaires provide higher conductivity.

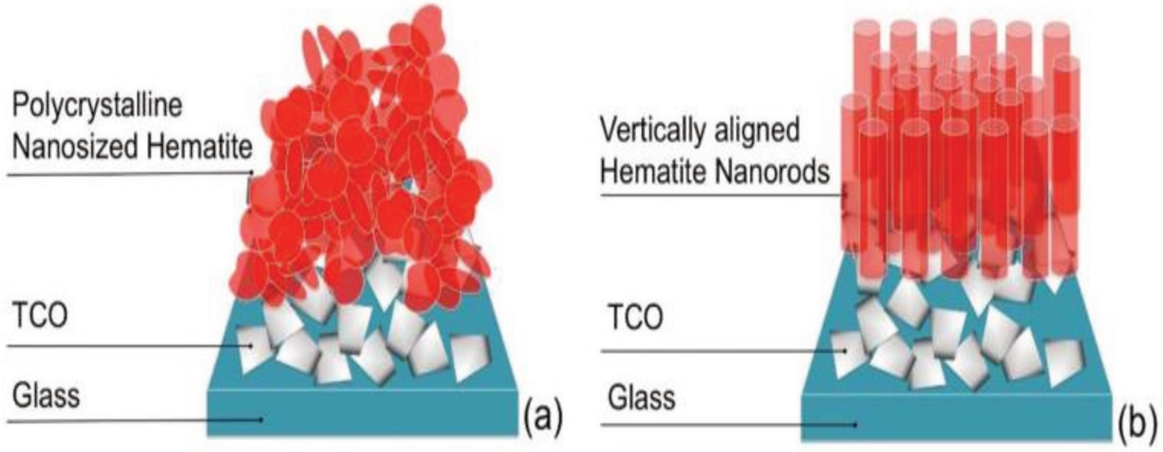


Figure 1.8: a) Polycrystalline nanosized α-Fe_2O_3 and b) α-Fe_2O_3 nanorods vertically oriented onto de FTO substrate.[68]

Despite much progress has been achieved for enhanced PEC activity of α-Fe_2O_3 photoelectrodes, the aforementioned drawbacks still hamper its use as an effetive semiconductor for application as a non-modified material. Therefore, the simple control of morphological characteristics is not sufficient to guarantee charge separation and further modifications are needed, for instance, the addition of a co-catalyst[33] of a second material with adequate properties to help the collection of the photogenerated charge carriers.

1.1.6 Important considerations into photoelectrochemical water splitting on α-Fe_2O_3, drawbacks and challenges

The electron transfer from α-Fe_2O_3 to the electrolyte after reaching equilibrium, causes an upward band bending of the CB and VB in the semiconductor. The extent of the band bending can be increased, decreased of even reversed to be downwards by applying an external bias. Figure 1.9 shows what happens to energy diagram of α-Fe_2O_3 or other n-type semiconductor when submitted to application of different external bias. For definition, flat band potential (V_{fb}) is the electrochemical potential applied to the semiconductor that reduces the band bending to zero, and there is no current. At this point, the semiconductor/electrolyte interface is not polarized. In α-Fe_2O_3,[69] commonly found values of V_{fb} range between 0.4 and 0.8 vs RHE.

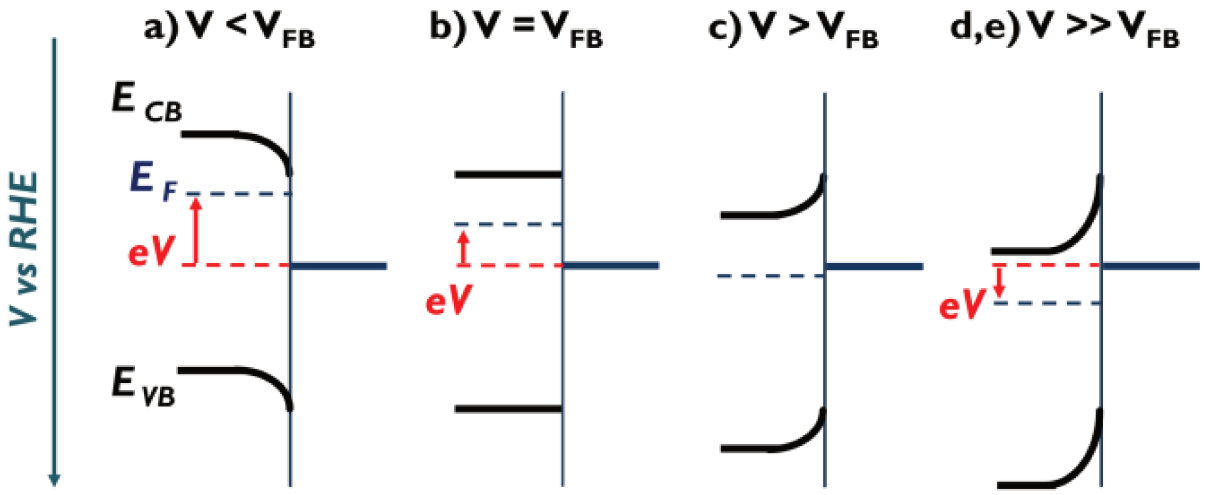


Figure 1.9: Electronic bands of an n-type semiconductor as a photoelectrode at different applied bias related to V_{fb}; a) V< V_{fb}, b) V= V_{fb}, c) V> V_{fb} and d) V>> V_{fb}.

i) For V < V_{fb}: When a more negative potential is applied compared to V_{fb} the Fermi level is forced to be downwards, causing the inversion of the band bending. After illumination, holes at the VB of α-Fe_2O_3 are transferred away from the surface and meanwhile, electrons move to the surface, leading to a negative current;

ii) For V = V_{fb}: At the moment in which the applid potential compensates the electrostatic potential of the electrolyte, band bending reduces to zero;

iii) For V> V_{fb}: For any potential higher than V_{fb}, the upwards of band bending

is enough to drive photogenerated holes towards semiconductor/electrolyte interface. At this point, the applied potential is able to overcome kinetic barrier of electron/hole recombination, generating positive current after starting water oxidation. For potentials much higher than the V_{fb}, a plateau of the photocurrent is reached, since recombination is no longer rate liming and mass diffusion becomes the key limiting factor.

As already mentioned, not only the aforementioned topics affect the photocurrent profile in α-Fe_2O_3 photoanodes. Despiste surface states has been ascribed as an important issue in α-Fe_2O_3 photoresponse profile, it has been also reported that the surface states in α-Fe_2O_3 can display ambivalent nature. Studies with combination of first-principle calculations and PEC experiments on α-Fe_2O_3 demonstrate that for potentials more negative than the onset potential (V_{onset} - potential at which current starts to rise after a reaction taking place), surface states act as recombination centers, while at more positive potentials these states are those where OER (oxygen evolution reaction) take place irrespective of pH.[70] In most cases, the chemical identity and the role of the states are not fully understood, which is currently the subject of intense investigation. Nonetheless, extensive work on solving misleading interpretation has been devoted towards obtaining accurate information.[71]

Figure 1.10 shows the schematic energy diagram of PEC water splitting based on α-Fe_2O_3 photoelectrode. The quase-Fermi energy levels of holes and electrons are indicated as $E_{F,p}$ and $E_{F,n}$, respectively and η_{tr} is the fraction of the photogenerated charge carriers reaching the semiconductor/electrolyte interface, normally dependent on a high anodic potential due to slow OER kinetics. After photoexcited by photons with energy equal of higher than the band gap (E_G) of α-Fe_2O_3, holes are transferred to the electrolyte with efficiency of η_{ct} to drive OER, as shown in Figure 1.10a. The quasi-Fermi level arises when a semiconductor is irradiated, where the materials is no longer in thermodynamic equilibrium, reaching quasi-equilibrium state.[72]

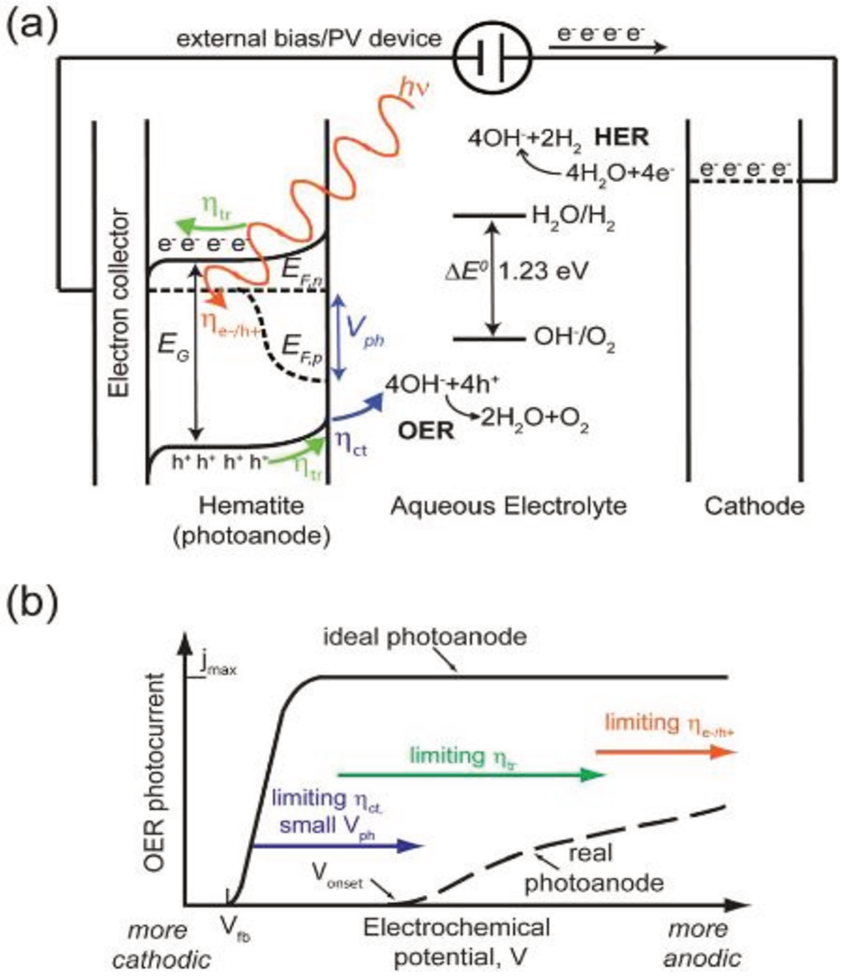


Figure 1.10: a) Schematic PEC system with energy diagram of device based on α-Fe_2O_3 photoanode. The illustration depicts photoexcitation of α-Fe_2O_3 and subsequent processes prior to OER and HER taking place, b) schematic illustration of the difference between an ideal PEC performance of α-Fe_2O_3 and a real photoanode where main factors dominate the J x V profile.[48]

In general, an ideal photoanode should display a photocurrent profile depicted in Figure 1.10b, where a V_{onset} and high photocurrent values are indispensable for enhancing the efficiency of a semiconductor for water splitting. Far from an ideal behavior where V_{ph} values in α-Fe_2O_3 should be equal to its optical band gap, the values are typically smaller than 0.4 eV and accompained by limiting η_{ct}. The real PEC performance of α-Fe_2O_3 is shown by the dashed line where V_{onset} is located at much more positive thant V_{fb}, reaching low maximum photocurrent j_{max}. For an ideal photoresponse of α-Fe_2O_3 photoelectrode, $V_{onset} = V_{fb}$ (typically 0.5 V vs RHE – reversible hydrogen electrode) and j_{max} reaches 12 mA cm^{-2} within 0.1 V. The plateau photocurrent for the ideal photoanode assumes the optical limit where all photons with energy higher than E_G are absorbed, with all holes being consumed to drive OER. The

result of V_{onset} - V_{fb} is often ascribed as the overpotential for the OER. To attain practical significance, the lowering of V_{onset} is a core issue to consider. For most α-Fe_2O_3-based electrodes reported, V_{onset} and V_{fb} values are ~1.0 V and 0.4-0.6 V vs RHE, respectively.[46] The remaining overpotential is a major drawback for the implementation for instance of α-Fe_2O_3-based tandem cells.[73]

Possible assignment of the electronic transitions in α-Fe_2O_3 has been in discussion in the literature, remained a subject of continue debate. In general, three types of electronic transitions in α-Fe_2O_3 are usually assigned to i) single ligand field (LF) or d-d transitions ascribed to Fe^{3+} ions; ii) O 2p → Fe 3d ligand to metal charge transfer (LMCT) and iii) metal to metal charge transfer (MMCT). The band gap photoexcitation in α-Fe_2O_3 is mostly attributed to charge transfer processes of the following types:

$$Fe^{3+} + Fe^{3+} \xrightarrow{h\nu} Fe^{4+}\ (h^+) + Fe^{2+}\ (e^-) \quad (1.4)$$

$$O^{2-} + Fe^{3+} \xrightarrow{h\nu} O^-\ (h^+) + Fe^{2+}\ (e^-) \quad (1.5)$$

It has been recognized that LMCT transition is the only source of photocurrent in Fe_2O_3.[38] Theoretical calculations have predicted that the highest occupied orbital has a strong O 2p character while the lowest unoccupied orbitals are mostly Fe 3d. The excited electrons are located at Fe 3d orbital while holes are at an O 2p, active for water oxidation. It has been considered that the electronic transitions resposible for the absorption of visible light in α-Fe_2O_3 are indirect/forbidden (Fe^{3+} d-d) whereas direct transitions between O 2p and Fe 3d orbitals occur only at energies higher than 3.2 eV. Surface holes on α-Fe_2O_3 have been recently assigned to Fe^{IV}=O species, and the localized accumulation of these species is more recently ascribed as the rate-determining step for water oxidation.[74,75]

More recent works have been devoted enormous effort to characterize the surface hole density of α-Fe_2O_3 during water oxidation. In particular, it has been described that the rate of water oxidation increases with third power of the surface hole density, suggesting three surface holes in the rate determining step of the reaction.[76] Basically, focusing on (110) surface of α-Fe_2O_3, which is the most active facet, hydroxyl-terminated α-Fe_2O_3 (110) with two neighbouring Fe(III)-OH groups form Fe(OH)-O-Fe(OH) dimer in aqueoues solutions. Successive oxidations processes of Fe(III)-OH lead to formation of low densities of Fe^{IV}=O species under low illumination and then to Fe^{V}=O. Finally, after three successive oxidations, the Fe dimer

obtains enough oxidation power to allow the nucleophilic attack of a water molecule to generate O_2.[75] In summary, it is assumed that the water oxidation reaction is primarily determined by the density of accumulated surface Fe^{IV}=O species, rather than changes in their energetics or even changes in potential across the depletion/Helmholtz layer.[74]

1.1.7 pH-dependent performance of α-Fe_2O_3 photoanodes

The electrolyte pH also plays a key role on the PEC performance not only for α-Fe_2O_3 but all semiconductors. It has been reported that the electronic properties of the SCLJ are highly linked to the electrolyte pH.[77] The pH not only affects the modulating ion transport but also the interfacial characteristics of the photoelectrode. For instance, there are reports on the changes of local pH that show an modification of the relative aligment between the semiconductor energy bands and the water redox energy levels.[78] These lead to the a modification of reaction mechanism[79,80] and also a change of the surface chemistry.[70]

Importantly, theoretical calculations combined with PEC impedance spectroscopy (PEIS) studies have shown that at higher pH values, Fermi level pinning is noticeably mitigated, decreasing the accumulated surface charges at surface traps, assisting the proceeding of water oxidation reaction.[70] On the other hand, the pH decrease invokes a gradual increase of the density of surface trap states, leading to deteriorate the performance of the photoelectrode.

In a recent work by Liu and co-workers,[81] the α-Fe_2O_3 photoanode response was dramatically affected by the increase in pH, exhibiting much higher photocurrent density as well as a cathodic shift in the onset potential by increasing pH from 7.0 to 13.6. Figure 1.11 displays the dynamic potential-pH diagram, which is an extended version of the Pourbaix diagram. As shown, the increase in the electrolyte pH from 7.0 to 13.6 lead to the enhancement of photocurrent values from 0.15 to 1.13 mA cm^{-2}.

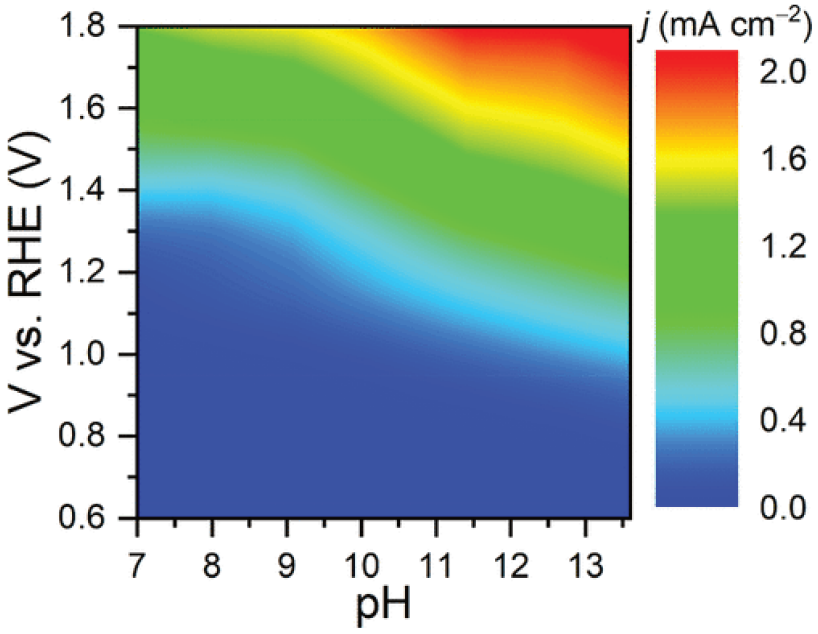


Figure 1.11: Photocurrent density-pH diagram of α-Fe_2O_3 photoanode under AM 1.5G illumination.[81]

Their work identified that the pH-dependent kinetics of water oxidation are a key step governing the PEC performance, significantly alleviating Fermi level pinning and defining the efficiency of charge transfer across the interface. Such parameters has a crucial impact on the photocurrent magnitude as well as the onset potential. Despite recent studies have shown strong evidence that charge accumulation links directly to the kinetic balance between charge recombination and charge transfer at the surface,[82,83] the identity of the surface reactive sites dependent on pH is still under long-running debate with considerable controversial conclusions.

1.1.8 Charge recombination in α-Fe_2O_3 photoanodes

The kinetic mismatch between water oxidation and charge carrier recombination is dramatically severe in α-Fe_2O_3.[74] The elucidation of the kinetic competition between electron/hole recombination and water oxidation is crucial for the development of efficient photoelectrodes for water splitting. In PEC water splitting approach, charge separation across the depletion of space charge layer with holes lifetime on the order of 0.1-10 s is required for efficient water oxidation. In some studies, intraband gap states, resulted from both oxygen vacancies[84] and crystalline disorder,[85] are assumed to represent either as recombination centers and charge transfer states mediating water oxidation,[77,86] whereas other studies attribute such states only for promoting surface recombination.[87,88]

It has been demonstrated the high dependence of the PEC performance of α-Fe_2O_3 photoanodes on the applied bias. Recombination processes on the 10 ms to 1 s time scale has already been demonstrated, and are assigned to recombination of bulk α-Fe_2O_3 electrons with relatively long-lived holes (milliseconds) accumulated at the semiconductor/eletrolyte interface. At modest anodic bias above V_{fb}, the space charge layer are able enough to spatially separate photogenerated electron/hole pairs.[83] However, at these potentials, the energetic barrier resulted by the space charge layer field is still not sufficient to inhibit subsequent back electron-hole recombination in the semiconductor bulk on a time scale faster than water oxidation and thus, stronger anodic bias is required to either obtain cathodic shift of onset potential and boost photocurrent density. At higher potentials, there is a high possibility of holes to accumulate at the semicondutor/electrolyte interface and their lifetime is potentially long enough (>1s) to promote water oxidation.[82]

Figure 1.12 shows the photocatalytic water splitting processes sequentially taking place at different time scales.[33] One can see that exciton separation and charge carrier lifetime have faster time scale compared to the hydrogen and/or oxygen evolution reaction.

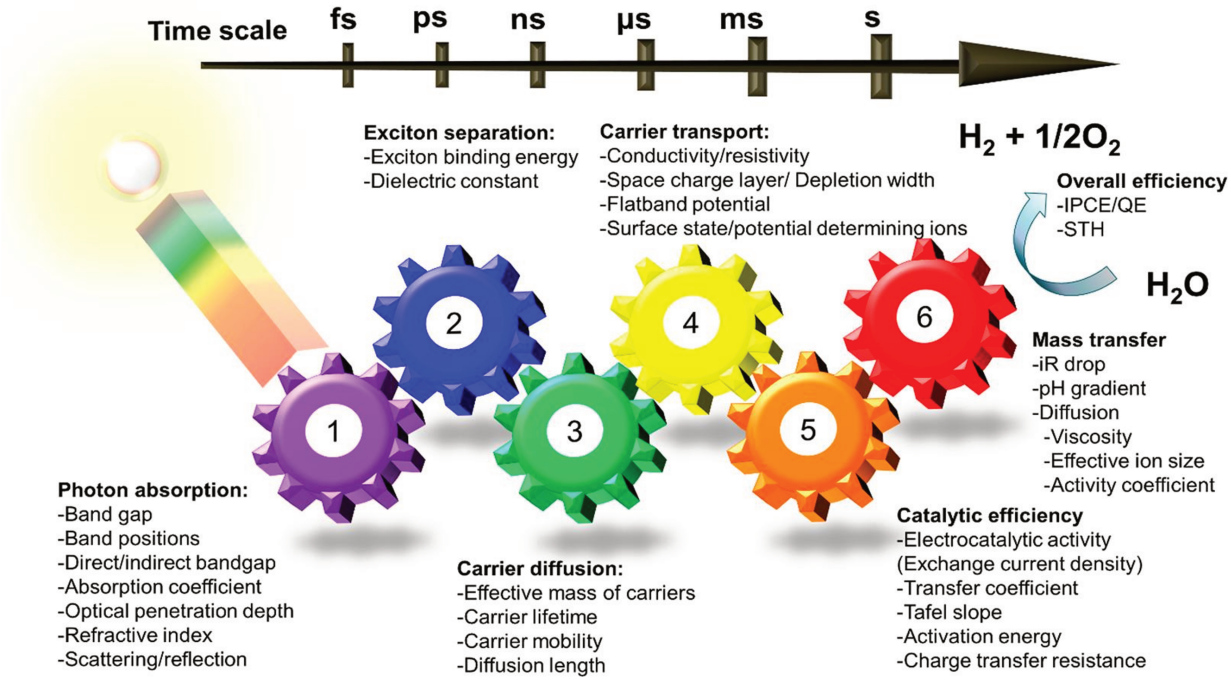


Figure 1.12: Sequential water splitting processes occuring at different time scales. All steps are connected and should be effectively integrated for successful overal water splitting.[33]

Figure 1.13 presents ultrafast (fs-ns) electron/hole recombination and the processes that occur under pulsed laser excitation and at different applied pontentials.

This model includes in addition to VB and CB positions, the intraband states located at few 100 mV below CB, which can act either as electron or hole traps. Under illumination and at potentials close to or cathodic of V_{fb}, a significant fraction of photogenerated electrons within the space charge layer are rapidly trapped into intraband states (represented by the full orange circles in scheme i). At potentials more anodic than V_{fb}, space charge layer is extended and less electrons fill the intraband states (resulting in empty orange circles in scheme ii). The population of the remained trapped electrons subsequently decays on the microsecond time scale due to recombination with holes in the VB. At even more anodic potentials ($V >> V_{fb}$), a substantial increase in the trapped electrons collected by the external circuit is achieved, decreasing charge recombination rate with holes in the VB and finally, photogenerated holes accumulate at the photoelectrode surface to perform water oxidation, as shown in Figure 1.13 (scheme iii).[82]

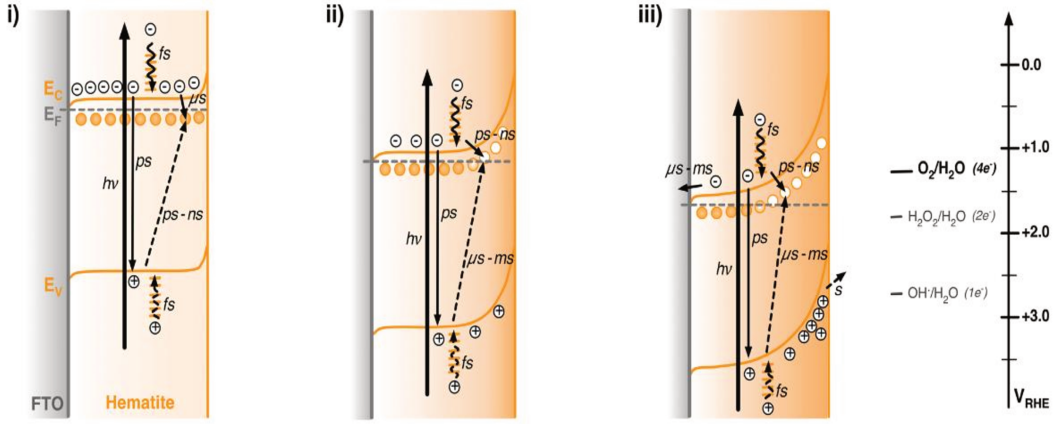


Figure 1.13: Schematic illustration of the energy diagrams and processes associated with photogenerated charge carriers in α-Fe_2O_3 photoanodes under illumination and at different applied potentials of i) 0.5 V vs RHE, ii) 1.1 V vs RHE and iii 1.6 V vs RHE.[82]

Based on the diagram illustration, one can see that charge recombination processes occur on time scale much faster than water oxidation. This means that prior to evolving O_2, the photoanode must overcome all those electron/hole recombination, even at high potential values. Consequently, the kinetic mismatch between the lifetimes of the photogenerated charges, limited by fast recombination processes on picosecond to millisecond time scales followed by slow kinetics of OER catalysis are one of the primary limitations to high efficiencies in α-Fe_2O_3.[74] Therefore, there has already been an enormous effort into the development of suitable techniques to deep understand complex mechanisms of charge recombination to proceed the manufacturing of effective photoelectrodes for water splitting.

1.2 Advanced techniques for charge carrier characterization

1.2.1 Transient Absorption Spectroscopy (TAS) for evaluating charge carrier dynamics

Transient Absorption Spectrocopy (TAS), also known as Laser Flash Photolysis has been used to investigate photogenerated charge carrier recombination for a wide range of semiconductors for electro and photoelectrocatalytic applications. TAS is a pump-probe technique able to characterize photo-induced charge carriers dynamics and associated lifetimes of molecules, materials and devices. The technique was first announced in 1950 by George Porter and Ronald G. W. Norrish, granting them the Nobel Prize in Chemistry in 1967 for their studies of fast chemical reactions by means of very short pulses of energy. Since the technique was able to measure reaction kinetics in the microsecond range, their pioneering work opened up new possibilities to study faster photochemical reactions, reaching the femtosecond scale in the 1990s.[89]

In a typical experiment, the excitation source is an intense short laser pulse (pump pulse) while the sample gets electronically excited. Such excited species are short-lived transient species and can be subsequently probed with a monochromatic light, known as a probe pulse in the visible to near infrared region, generating a spectrum of the absorption as a function of wavelength and/or time. The measured absorption is generally expressed as the difference in optical density (ΔOD) after (excited state) and before (ground state) pulse of excitation, as shown in Figures 1.14a and b. This variation can also be determined by monitoring the probe pulse at a specific wavelength.

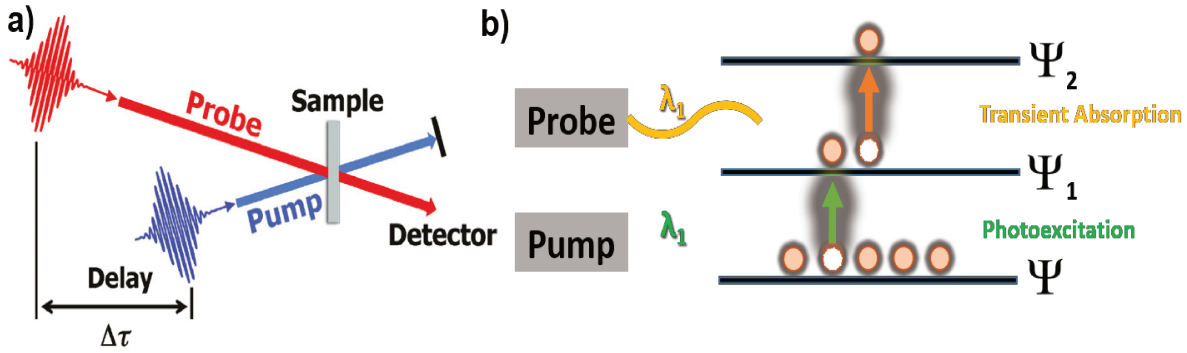


Figure 1.14: Schematic illustration of a) pump-probe transient absorption spectroscopy and b) the generation of transient species after short pulse excitation.

The transient absorption spectrum ΔOD measures the difference between ΔOD_2 and ΔOD_1, represented by the following Equation 1.6 and means the change in absorption resulted after passing the pump laser pulse.

$$\Delta OD = \underbrace{A_{fast}t^{-\alpha}}_{\substack{bulk \\ recombination}} + \underbrace{A_{slow}e^{-\frac{t}{\tau}}}_{\substack{surface \\ recombination}} \quad (1.6)$$

where A_{fast}, A_{slow}, α and τ are the amplitude and time constants, obtained after signal fitting. The first term of the equation is related to bulk electron/hole recombination on shorter time scale after excitation (μs-ms). The second term is ascribed to both surface recombination and water oxidation, which compete with each other.

This technique has been utilized by many research groups with the aim of understanding the charge transfer dynamics in several photocatalytic processes, such O_2 reduction,[90] NO oxidation[91] and water oxidation.[92] Depending on the time resolution of the experiment, different processes can be monitored. In water splitting, the kinetic competition between water oxidation and electron/hole recombination is a paramount consideration for the development of photoelectrodes for solar-driven water splitting. Some studies have also focused on ultrafast timescales (<75-150 ps) of recombination dynamics of photoinduced electrons and holes.[67,93] Such fast recombination process are typically associated to fast bimolecular (non-geminate) recombination of high photoinduced charge carrier densities, but their impact on PEC performance are still unclear.

1.2.2 Surface Photovoltage Spectroscopy (SPS)

Surface photovoltage spectroscopy (SPS) is another powerful and reliable technique able to investigate and assess the mechanisms and photochemical charge carrier dynamics within the photocatalysts,[94,95] where the photovoltage is obtained as a function of external illumination using a Kelvin probe.[96,97] The use of SPS technique contributes to the construction of surface and interface band diagrams, including the measurement of energy levels of semiconductors.[95] Additionally, SPS can be used to resolve the kinetic and thermodynamic contributions that cannot be obtained by only PEC studies.[98] SPS has been applied in many photocatalysts including $SrTiO_3$,[96] ZnO,[99] CdSe,[97] $K_2Ti_4O_9$[100] and $BiVO_4$.[101]

In SPS, the contact potential difference (CPD) of a film is measured during illumination by monochromatic light. The magnitude of the signal is directly proportional to the charge separation properties and it can be used to determine the

effective band gap of the material and also to understand the photochemical charge transfer properties.[97] Measurements using SPS are contactless and non-destructive that probes contact potential difference changes (△CPD) in the surface of thin films upon illumination. The changes in the surface voltage are monitored as a function of incident photon at different wavelengths.[95,102] A photovoltage arises from the movement of photogenerated charge carriers through the film or across the interface between the film and the substrate,[94] as illustrated in Figure 1.15.[98]

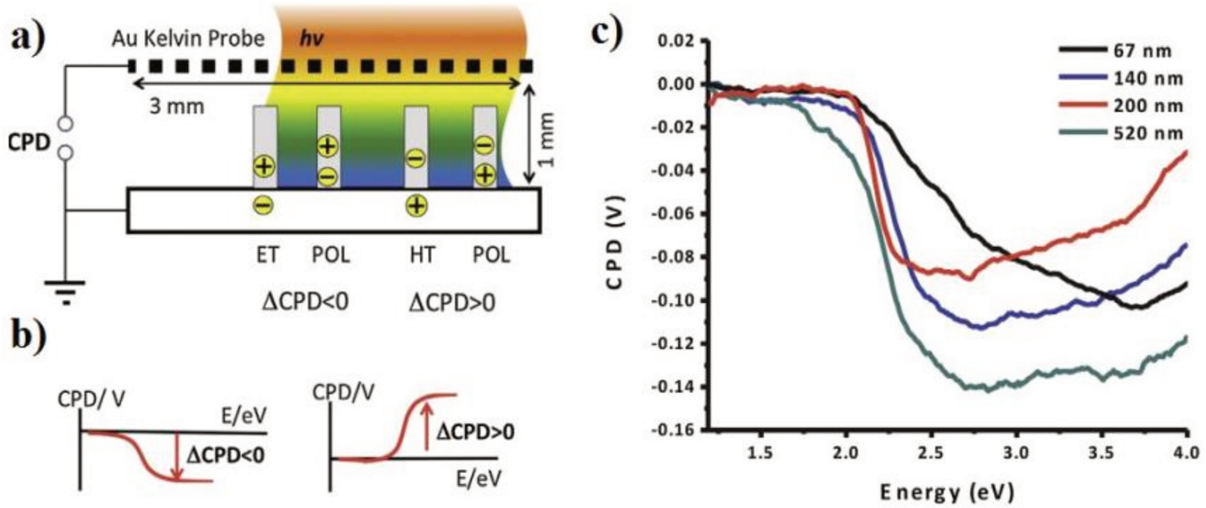


Figure 1.15: a) Measurement configuration of SPS plot with b) negative and positive signals and c) a typical spectra (photovoltage signal (△CPD) versus the photon energy (eV)) of α-Fe_2O_3 films with different thickness.[98]

With a sensitivity much higher than that of PEC measurements, SPS signals are obtained due to the polarization of electron-hole pairs (POL) or due to electron or hole injection (ET or HT), as shown in Fig. 1.15a. When △CPD signal is negative (Fig. 1.15b), electrons move away from the Kelvin probe, and when it is positive, the signal means that electrons move toward the Kelvin probe.[98] Therefore, the SPS is positive in p-type semiconductors and negative in n-type semiconductors.[95]

In the case of α-Fe_2O_3 (n-type), its absorption coefficient is 8 x 10^6 cm^{-1} at 2.75 eV, which requires a thickness film of at least 575 nm.[57] Because of this requirement, thickness film around this range of length shows more negative photovoltage, as shown in Fig. 1.15c. This study confirmed that the photochemical charge separation at α-Fe_2O_3 nanostructures is mostly determined by the kinetics and thermodynamics at its surface and also, shows the importance of surface states in α-Fe_2O_3 for hole trapping and water oxidation.[98]

Chapter 2

Unraveling the role of single layer graphene as overlayer on hematite photoanodes

In this first part of the thesis, it will be discussed a general introduction of the graphene-based materials and their optoelectronics properties. Single-layer graphene (SLG) will be used as a surface modifier onto α-Fe_2O_3 photoanode surface. The properties of the as-synthesized materials will be evaluated for better understanding the charge carrier dynamics responsible for enhanced PEC perfomance towards water oxidation.

Introduction

It has been shown that single-layer graphene (SLG) added over a wide range of photocatalytic materials surface can be an advantageous strategy to improve their performance towards practical applications.[103] Nevertheless, the beneficial effect and the role of SLG deposition on the materials surface have not been fully elucidated and it opens a wide avenue for investigation.

Combination of complimentary techniques is a powerful way to characterize the charge carrier dynamics, giving novel insights into how the SLG positively affects the materials surface. Studies employing transient absorption spectroscopy (TAS), a pump-probe technique, have been devoted to investigate and monitor the charge carrier lifetime on microsecond to second time scales and to study the effect of bias potential on the electron-hole recombination rate in α-Fe_2O_3 photoanodes.[82,104] Pendlebury *et al.*[105] correlated the application of a positive bias with the long-lived photoholes in Fe_2O_3 photoanodes using TAS.

Herein, by combining TAS, SPS and electrochemical impedance spectroscopy (EIS) techniques, it is revealed that the SLG increases the lifetime of photogenerated charge carriers leading to a more efficient photochemical charge separation. The unclear relation between better PEC performance of α-Fe_2O_3 photoanodes with the addition of SLG was the subject of scrutiny in this study. In fact, the SLG seems to act reducing the surface traps at the α-Fe_2O_3 photoanode-electrolyte interface and consequently improving the efficiency of hole diffusion and promoting an enhancement of the overall photoresponse.

Theoretical Background

2.1 Graphene

Although graphene has been studied for the past 40 years, it was only in 2004 that graphene was first isolated by Konstantin Novoselov and Andre Geim from the University of Manchester by micromechanical cleavage, technique well-known as scotch-tape method.[106] Such discovey garanteed their prize in Nobel of Physics in 2010. Recently, the graphene industry is moving forward to a wide range of applications, including nanoelectronics,[107] gas sensors,[108] biological sensors,[109] fuel cells,[110] photovoltaic devices[110] and photocatalytic hydrogen generation.[111] In photocatalysis, graphene can contribute to electron transport, decreasing the charge carriers recombination rate.

Additionally, graphene offers great flexibility for device application since it can be cut and used as many frames of any shape by using lithographic techniques.[112,113]

By definition, graphene is a monolayer of sp^2 carbon atoms tightly packed into a two-dimensional plane (2D) honeycomb lattice, which has been gained enormous attention since its first isolation due to its excellent mechanical, thermal, optical and electrical properties.[114] Besides being one of allotropes of carbon, including diamond, carbon nanotube and fullerene, graphene is the basic building block for graphitic-based materials of other dimensionalities including 0D fullerenes,[115] 1D nanotubes[116] and 3D graphite.[117] Graphene presents high thermal conductivity (~ 3000 - 5000 W m^{-1} K^{-1}), excellent intrinsic carrier mobility (2,000,000 $cm^2V^{-1}s^{-1}$), high surface area (~ 2600 m^2g^{-1}) and excellent optical transparency to a wide range of light wavelength, gaining the possibility to be utilized as transparent electrodes in optoelectronic devices.[118] Figure 2.1 shows the bidimensional structure of graphene monolayer and the bands structure of pure, n-type and p-type graphene.

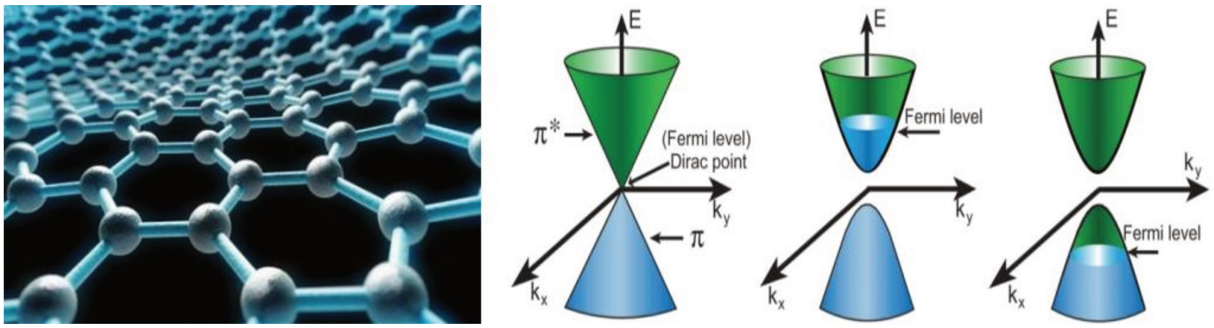


Figure 2.1: Bidimensional structure of graphene monolayer, arranged in an atomic-scale hexagonal lattice made of carbon and b) bands structure of pure, n-type and p-type graphene.[119]

The VB π and CB π* energy bands of graphene form the Dirac cone, where the two bands are intercepted. The zero-gap characteristic of graphene is due to the location of the VB and CB that intercept at the zone corners (the K point in the Brillouin zone).[120] By modifying the optical properties of graphene when introducing heteroatoms or functional groups, it is possible to extend its practical applications, specially in photocatalytic systems. The adsorption of oxygen atoms removes double bonds of carbon atoms, forming C-O covalent bonds, modifying the position of the atoms, and thus, introducing a band gap in graphene. The functional groups introduced in graphene lead to a facilitated formation of different composites with semiconductors due to chemical bonds between oxygen and metal atoms. Subsequently, the material can be submitted to a reduction process to remove the functional groups, partially

restoring the C=C conjugated bonds and consequently the aromaticity of graphene layers. Figure 2.2 shows the graphene oxidation process to produce graphene oxide (GO) and subsequent reduction do reduced graphene oxide (rGO) with partly restoration of the structure and properties of single layer graphene (SLG).

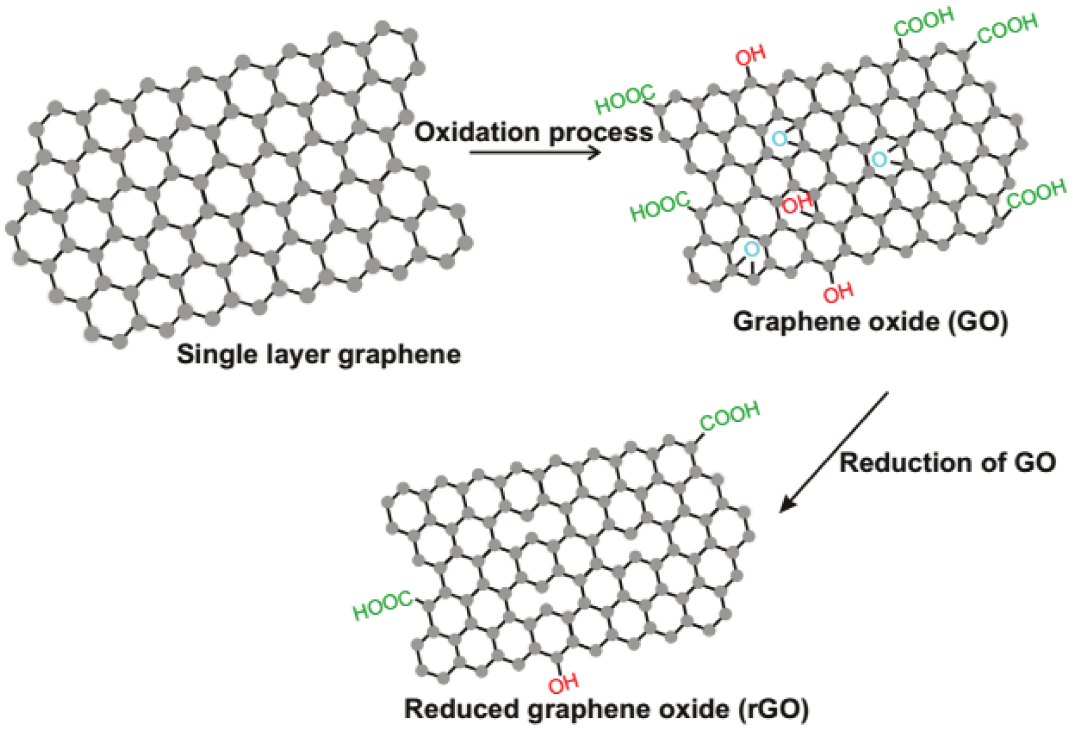


Figure 2.2: Synthesis of rGO from graphite, after GO reduction process.[121]

Many methods of graphene preparation have been described in the literature since its discovery and a wide range of properties can be obtained by specific procedures, leading to produce either bulk material or graphene films on solid supports. By a theoretically predictability, graphene is a zero-gap semiconductor, offering limited applicability for practical industry.[122] The first method reported was the mechanical exfoliation of few-layer graphene involving the use of scoth tape.[123] Additional methods include reduction of graphene oxide,[124] electrochemical and chemical exfoliation of graphite.[125] However, these methods usually result in the formation of bulk materials with a relatively poor usability, which in many cases are influenced by many defects in the graphene structure.

The most used procedure for the synthesis of graphene-based materials is the Hummers´ method,[126] which is a chemical process to oxidize graphite in the presence of strong oxidants in acid media, resulting the final product as graphite oxide. Since graphite oxide contains spacing between the graphene sheets due to many functional groups in their structure, their exfoliation is facilitated to produce GO. Then, GO can

be further reduced to rGO by different strategies as hydrothermal,[127] solvothermal[128] and photocatalytic reduction.[129]

Recently, the use of reduced graphene oxide (rGO) as an overlayer coating α-Fe_2O_3 photoanode surface showed to be a promising alternative to enhance the photocurrent density. In a previous work of our group,[130] the incorporation of rGO in α-Fe_2O_3 films showed the enhancement in photocurrent generation of 46%, which was attributed to a better charge separation and electron transport, inhibiting charge carrier recombination. Although some improvements have been achieved with rGO, SLG is even more compelling because it has much less defects, less functional groups on surface and edges and its synthesis is more reproducible, giving rise to a material with very well-known composition and more accurate properties as conductivity and transparency. SLG coating over Ti:α-Fe_2O_3 surface has been already demonstrated to be more effective to boost the performance in PEC cells.[131] The use of rGO in photoelectrodes has been resulted in enhanced optical, conductive and chemical properties of different materials, whereas the use of SLG can optimize their electrical, stability and redox properties. The use of single layer graphene (SLG) has been shown a substantial enhancement of the photoelectrochemical performance of many semiconductors.[131,132] Compared to other types of graphene-based materials as graphene oxide, reduced graphene oxide, which present a considerable amount of defects and functional groups, SLG is a promising alternative for replacing rGO-based materials.

Based on many defects derived from the synthesis of different types of graphene and to take full advantage of the outstanding properties of the material, the standardization of the growth process is an important issue to accomplish. Therefore, the growth technique should ensure the high yield, followed by high quality of the SLG sheets. In this concept, one can mention bottom-up synthesis methods as chemical vapour deposition (CVD),[133] which is the most practical and play an accurate control of the continuous growth of graphene films. In the CVD growth method, a continuous flow of carbon gas precursor/Ar/mixture, in which methane (CH_4) is the most used as carbon source, results in the graphene growth. This results in large-area, high-quality graphene with relatively low cost. Since carbon presents low solubility into copper (Cu),[134] copper foils are used as the preferred substrate, allowing the production of large-scale of SLG sheets.

Objectives

The aims in this chapter are twofold: First, obtaining SLG of high quality with subsequent successful deposition onto α-Fe_2O_3 nanorods photonodes and hereafter, unravel the main reason for enhanced photocurrent density after its deposition over α-Fe_2O_3 photoelectrode surface. Despite better performance, the knowledge about charge carrier dynamics is important for better understanding the properties of α-Fe_2O_3/graphene-based photoelectrodes. To accomplish this, the combination of transient absorption and surface photovoltage spectroscopies will be carried out.

2.2 Experimental

2.2.1 α-Fe_2O_3 nanorod films preparation

α-Fe_2O_3 nanorod films were prepared by aqueous solution precursor method under hydrothermal conditions.[135–138] For this, 2.5 mmol of $FeCl_3.H_2O$ was dissolved in 25 mL of distilled water and added into 25 mL of 3.75 mmol of urea aqueous solution, and the system was let stirring for 10 min. Afterwards, FTO (fluorine-doped tin oxide) substrates were vertically placed into the solution and the non-conductive side of the substrate was masked using Teflon tape to avoid the deposition of α-Fe_2O_3 particles. The reaction was performed in a 100 mL Teflon-lined stainless steel autoclave at 100 °C for 10 h. Then, the films were annealed at 750 °C for 30 min to convert the FeOOH phase into α-Fe_2O_3 and to activate their surface, as shown in Figure 2.3. Films with different thicknesses were prepared by varying the amount of $FeCl_3.6H_2O$ and urea precursors, as shown in Table 1.

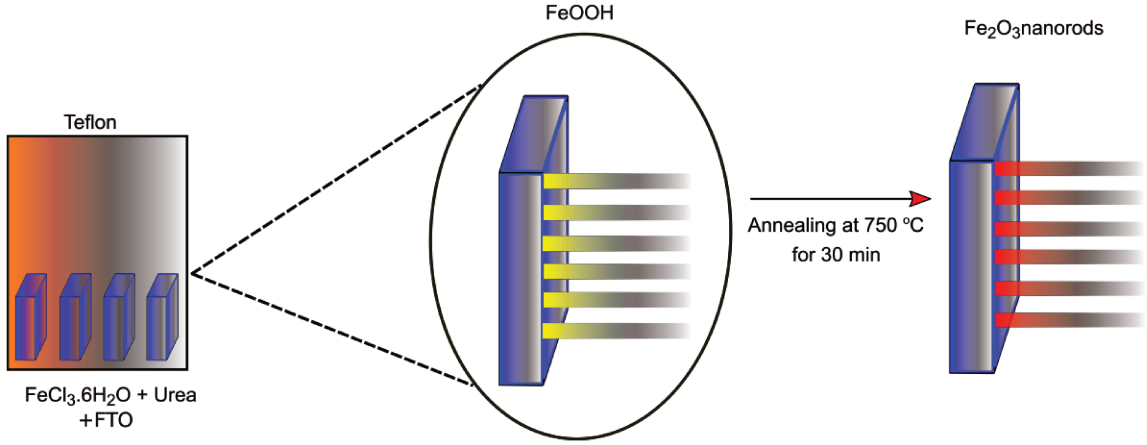


Figure 2.3: Schematic illustration of hydrothermal synthesis of α-Fe_2O_3 nanorod films onto FTO substrate.

Table 1: Precursors amount in the synthesis of α-Fe_2O_3 nanorod films varying their thickness.

Sample	$FeCl_3.6H_2O$ (mol)	Urea (mol)
S1	1.25 mmol	1.88 mmol
S2	2.50 mmol	3.75 mmol
S3	5.00 mmol	7.50 mmol
S4	10.0 mmol	15.0 mmol

2.2.2 Synthesis of single layer graphene (SLG)

SLG was synthesized via chemical vapour deposition technique (CVD).[139] Copper foils (Alpha Aesar, 99.8% purity) were cut into squares of 2 cm^2 and immersed in an ultrasound bath with acetone for 5 min and then in isopropyl alcohol for another 5 min. Each sample was dried using high-purity nitrogen gas. The pure Cu foil was loaded into a quartz tube furnace and then heated up to 1000 °C under 20 sccm H_2 atmosphere and annealed for 1 h. Methane (CH_4) gas was then used as carbon precursor with constant flow of 2 sccm for 20 min, maintaining a growth pressure of 330 mtorr. The system was cooled down at a rate of 300 °C/min under H_2 and CH_4 flux to ambient temperature.

2.2.3 SLG deposition onto α-Fe_2O_3 nanorods films

Firstly, a polyurethane (PU) solution (1 wt% in tetrahydrofuran, THF) was spin-coated on SLG/copper foils at 3000 rpm for 30 s and dried at 80 °C on a hot plate for 10 min.[140] The SLG was etched by floating the copper foil in a $FeCl_3$ (10 wt%) aqueous solution (Trancene CE100) until the complete dissolution of the copper. The SLG/PU films were immersed several times in distilled water to remove the excess of copper species. Afterwards, SLG was deposited onto the α-Fe_2O_3 films by immersing the substrate below the graphene sheet that is floating at the surface of the solution. Subsequently, the α-Fe_2O_3/graphene-PU film was immersed in a THF solution for 24 h to dissolve the PU polymer and dried at 200 °C for 2h.

2.2.4 Structural characterization

The materials were characterized by X-ray diffraction (XRD) using an X-ray diffractometer XRD-7000 of Shimadzu MAXIMUM with a voltage/current of 40 kV/30 mA and a scanning angle of 2θ from 20 to 70°. The Raman spectra were measured using a confocal Raman model T64000-Jobin Yvon with exposure time of 30 s and accumulation of 100 spectra in the range of 400-3250 cm^{-1}. The morphology of the as-prepared α-Fe_2O_3 and of the α-Fe_2O_3/SLG photoanodes was obtained by field emission-scanning electron microscopy (Quanta 250 FEG-SEM). In order to analyze the chemical composition of the materials, XPS analysis (X-ray photoelectron spectroscopy/ScientaOmicron ESCA + spectrometer) was performed. An excitation source of Al Kα ($h\nu$ = 1486.6 eV) radiation and high-performance hemispheric analyzer

(EAC2000) was used with an ultra-high vacuum chamber (UHV) maintaining the pressure of 10^{-9} Pa during the measurements. The XPS high-resolution spectra were recorded at a constant pass energy of 20 eV with a 0.05 eV per step.

2.2.5. Photoelectrochemical (PEC) characterization

PEC measurements were carried out using a potentiostat/galvanostat (μAutolab III). The photocurrent-potential (I-V) curves were obtained under irradiation with a polychromatic light under intensity of 100mW cm^{-2} (450 W Xenon lamp, AM 1.5G). The measurements were performed in a three-electrode cell with α-Fe_2O_3 and Fe_2O_3/SLG photoanodes (1 cm^2) as the working electrode, Ag/AgCl in saturated KCl (3 mol L^{-1}) as the reference electrode and Pt wire as the counter electrode. The electrolyte was 1 M NaOH (pH 13.6, 25°C, 50 mL) solution. Linear sweep voltammetry (LSV) was carried out at a scan rate of 10 mV s^{-1} in the range of 0.2 to 1.8 V vs. RHE (reversible hydrogen electrode). The Ag/AgCl electrode potential was converted to RHE by Nernst formula (Equation 2.1).

$$E_{RHE} = E_{Ag/AgCl} + 0.059 * pH + E^{0}_{\frac{Ag}{AgCl}} \quad (2.1)$$

where E_{RHE} is the potential *vs.* RHE, $E^{o}_{Ag/AgCl}$ = 0.1976 V at 25°C and $E_{Ag/AgCl}$ is the potential *vs.* Ag/AgCl and the pH is 13.6 (1 M NaOH aqueous solution).

EIS measurements were performed using the same three-electrode cell in 0.1 M NaOH in dark conditions with coupled Faraday cage potentiostat/galvanostat (Autolab PGSTAT129N), to avoid external influence. EIS provides an electronic analysis for Mott-Schottky plots (C^{-2} *vs* E), following Equation 2.2:

$$\frac{1}{C^2} = \frac{1}{e\varepsilon\varepsilon_0 N_D A^2}\left[\left(V - V_{fb}\right) - {}^{KT}/_{e}\right] \quad (2.2)$$

where C is the capacitance, e the elementary charge, $\mathcal{E}_0$ the vacuum permittivity, $\mathcal{E}$ the dielectric constant, A the area, K the Boltzmann constant, V the applied potential and T the temperature. The parameters N_D (donor density) and V_{fb} (flat band potential) were calculated by linear adjustment from Mott-Schottky plot. Additionally, the charge transport in the material was analyzed by the semi-circle in the Nyquist plot.

The IPCE (incident photon-to-current conversion efficiency) values were obtained according to the following formula (Equation 2.3),

$$IPCE\ (\lambda) = \left(J * 1240/P_{light} * \lambda\right) \tag{2.3}$$

where J is the measured photocurrent density (mA cm^{-2}), 1240 is the value obtained by multiplying h (Planck´s constant) by c (speed of light), P_{light} is the monochromatic illumination power (mW cm^{-2}) and λ is the wavelength (nm) of the incident light.

2.2.6 Transient absorption spectroscopy (TAS) measurements

TAS measurements at µs-s time scale were carried out using a pump-probe transient absorption spectrometer (Optical Building Blocks Corporation - OBB), illustrated in Figure 2.4. A nitrogen laser was used as UV excitation source (337 nm, pulse width = 6 ns, typically 1 Hz repetition, 150 μJ. cm^{-2}. $pulse^{-1}$). The probe pulse was obtained using a light source (tungsten lamp) and the wavelength at 650 nm was selected using an OBB monochromator. The measurements were conducted on α-Fe_2O_3 and α-Fe_2O_3/graphene films under 1.2 V_{RHE} of applied bias using the same cell described in the PEC characterization section, in which the mΔOD is the transient absorption change. The signal was measured using a digital oscilloscope (Tektronic, TDS 2022C).

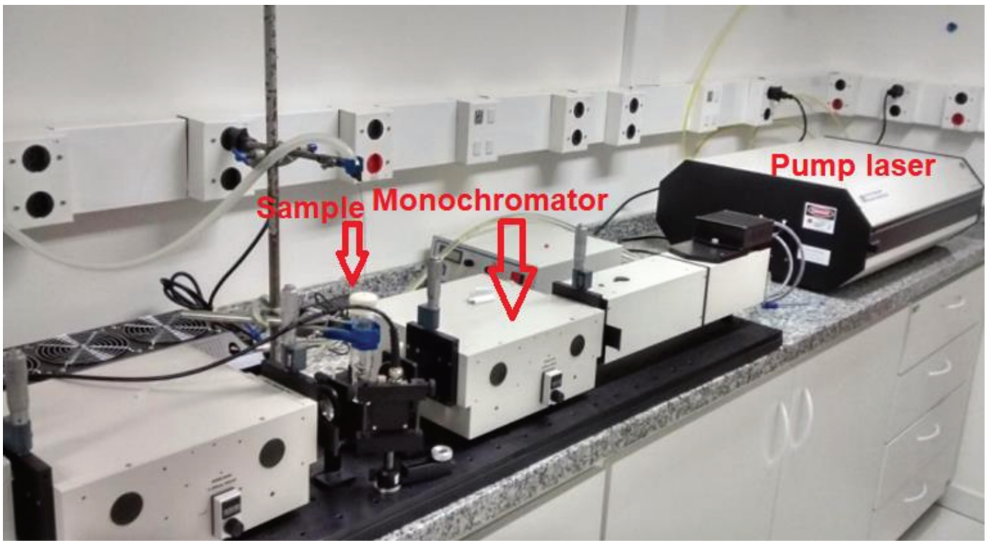


Figure 2.4: Transient absorption spectrometer used for charge carrier dynamics experiments.

2.2.7 Surface photovoltage spectroscopy (SPS) measurements

SPS measurements were carried out using a gold mesh Kelvin probe (Delta PHI Besocke, sensitivity of 1 mV) as the reference electrode inside a home-built vacuum chamber (~10^{-5} mbar). The samples were placed in the chamber and illuminated with a 150 W Xe lamp filtered through an Oriel Cornerstone 130 monochromator. The CPD data were plotted *vs.* energy (eV). The measurements were conducted on α-Fe_2O_3 and α-Fe_2O_3/SLG films.

2.3 Results and discussion

Prior to SLG deposition, the α-Fe_2O_3 nanorods films thickness was optimized based on the photocurrent values in which the best samples were chosen for further characterizations. Four samples were prepared by varying their thicknesses through a control over the amount of precursors and then further characterized. The XRD patterns of the α-Fe_2O_3 films (S1, S2, S3 and S4) were obtained after an annealing treatment at 750 °C for 30 min and assigned as alpha phase of hematite (JCPDS 33-0664), see Figure 2.5a.

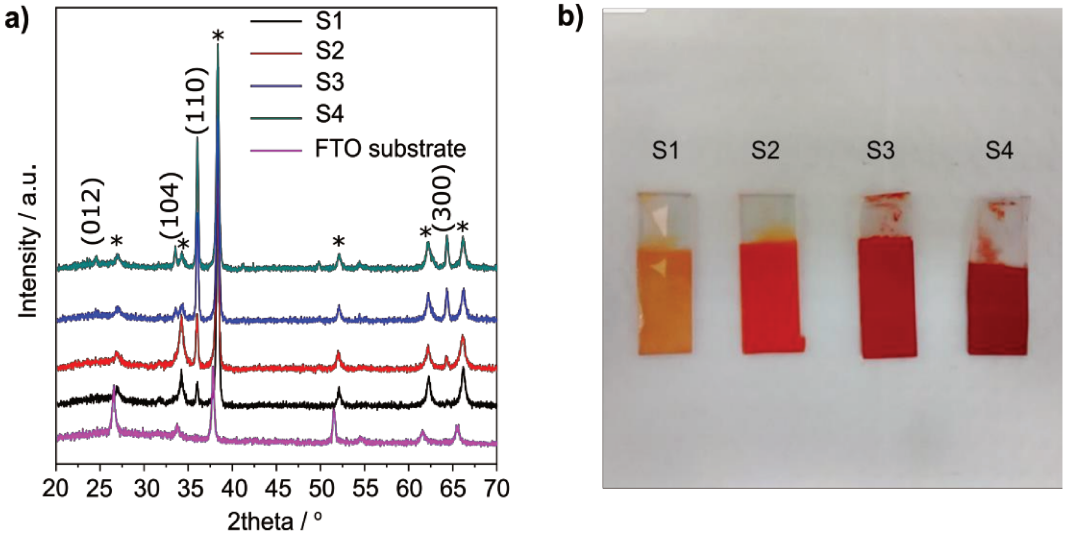


Figure 2.5: a) X-ray diffraction patterns of S1, S2 S3 and S4 samples and of the FTO substrate (* denotes the FTO substrate peaks) and b) photographs of S1, S2, S3 and S4 films.

The most intense diffraction peak is (110) at 35.5°, indicating the preferential growth of α-Fe_2O_3 in the [110] axis vertical to the substrate. This crystallographic peak provides higher conductivity in pristine α-Fe_2O_3 nanostructure[141]

and consequently facilitates the charge transport through one-dimensional nanorod structure.[142,143] The intensity of this peak increases from S1 to S4, from thinner to thicker films. The shift in the peaks position of the films compared to that of FTO may be resulted by the high temperature during thermal annealing, since the FTO substrate was not thermally treated. The colour of the α-Fe_2O_3 films changes from orange to dark red as the thickness increases, due to light scattering as depicted in Figure 2.5b.

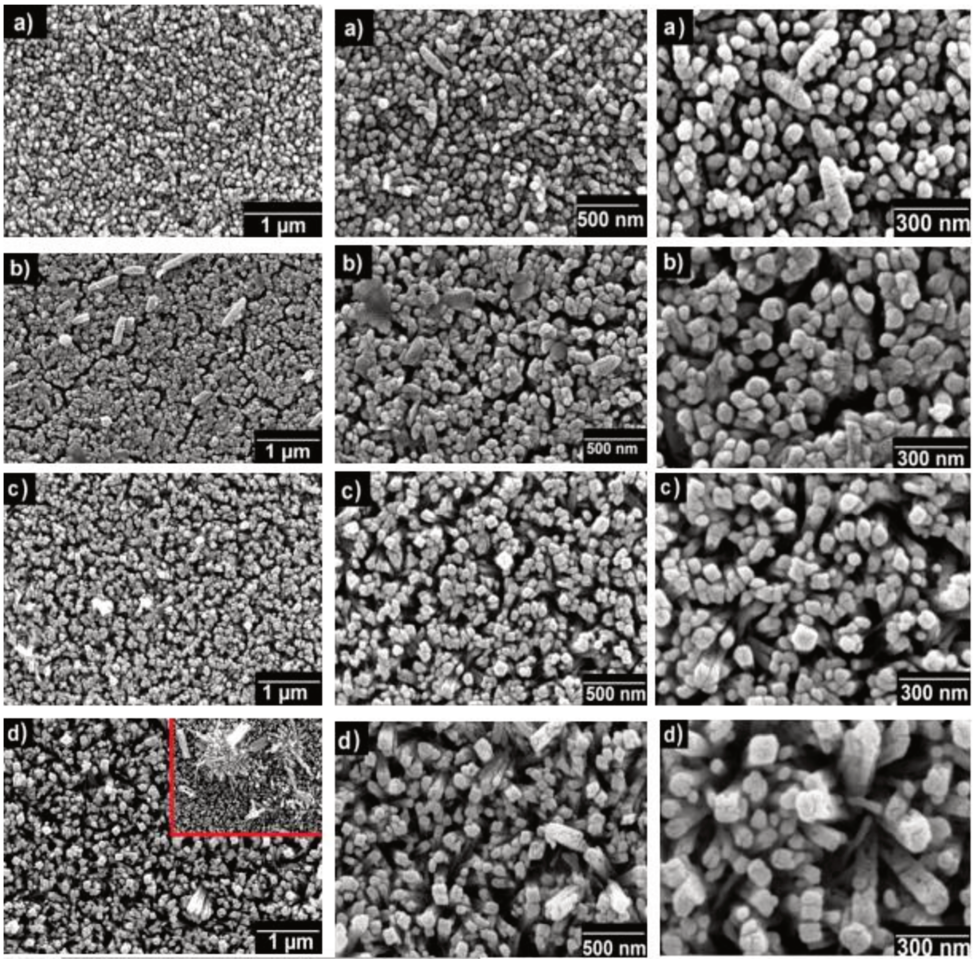


Figure 2.6: Top-view FEG-SEM images of a) S1, b) S2, c) S3 and d) S4 α-Fe_2O_3 samples.

The morphology of the α-Fe_2O_3 films was investigated through FEG-SEM. The top-view FEG-SEM images of the α-Fe_2O_3 photoanodes with nanorod shapes are shown in Figures 2.6a-d. The effect of the amount of precursors on the thickness of α-Fe_2O_3 films was investigated by cross-sectional FEG-SEM images (Figures 2.7a-d). It can be seen that the thickness of the films is highly affected by Fe^{3+} precursor concentration in the solution, in which higher concentrations lead to longer and larger Fe_2O_3 nanorods and consequently an increase in film thickness. The S1, S2, S3, and S4 samples present thicknesses of 297, 380, 1167 and 1700 nm, respectively. Additionally,

for thicker films, it is observed that an excess of α-Fe_2O_3 nanorods is deposited over the vertically oriented nanorods that are directly in contact with the FTO substrate (inset in Figure 2.6d), as previously observed by Carvalho and co-workers.[143] This may affect the charge carrier transport across the α-Fe_2O_3 nanorods and consequently the photocurrent density. To confirm this hypothesis and evaluate the influence of film thickness, PEC measurements were carried out using front and back side illumination.

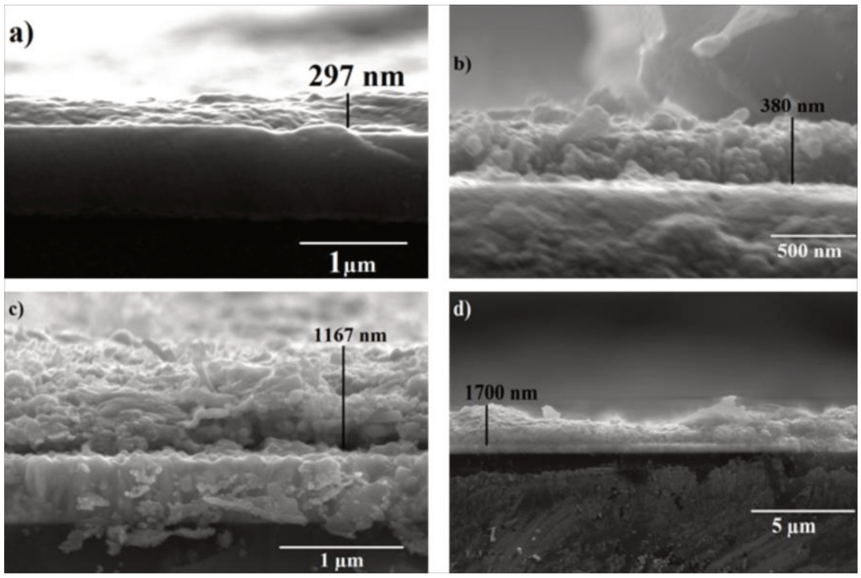


Figure 2.7: Cross-section images of a) S1, b) S2, c) S3 and d) S4 samples depicting their thicknesses.

As expected, the photocurrent density values (Figure 2.8a-d) are strongly influenced by film thickness. Thinner films (S1 and S2) generate higher photocurrent when the front side is illuminated. On the other hand, thicker films (S3 and S4) show higher photocurrent densities from back side illumination. Since the diffusion length of holes in α-Fe_2O_3 is of only 2-4 nm, thinner films with shorter α-Fe_2O_3 nanorods length result in a more effective suppression of electron/hole recombination.[49,82] This dependence of the photocurrent density with the thickness and side of illumination can be related to the photon penetration depth at visible wavelengths in α-Fe_2O_3 ($\alpha = 8 \times 10^4$ cm^{-1} at $\lambda = 550$ nm). In theory, α-Fe_2O_3 requires a thickness in the range of 400-800 nm to absorb the maximum of the sunlight spectrum.[144,145] Herein, the S1 and S2 photoanodes, which have thicknesses less than 400 nm, show higher photocurrent values from front side illumination. Although the S1 and S2 photoanodes absorb less light than the thicker films, the electrons generated at the top of the film can easily travel through the nanorods and be injected into the substrate to reach the external circuit.

In contrast, for S3 and S4 films, front side illumination leads to a decrease in the photocurrent density, since the pathway for electron transport is too long to prevent the charge recombination, even with higher absorption. Thicker films induce a built-in resistance increasing the energy barrier to the charge transport due to several point defects that act as a favorable recombination site. For further investigations and SLG surface modification, the S2 photoanode was selected due to its highest photocurrent response.

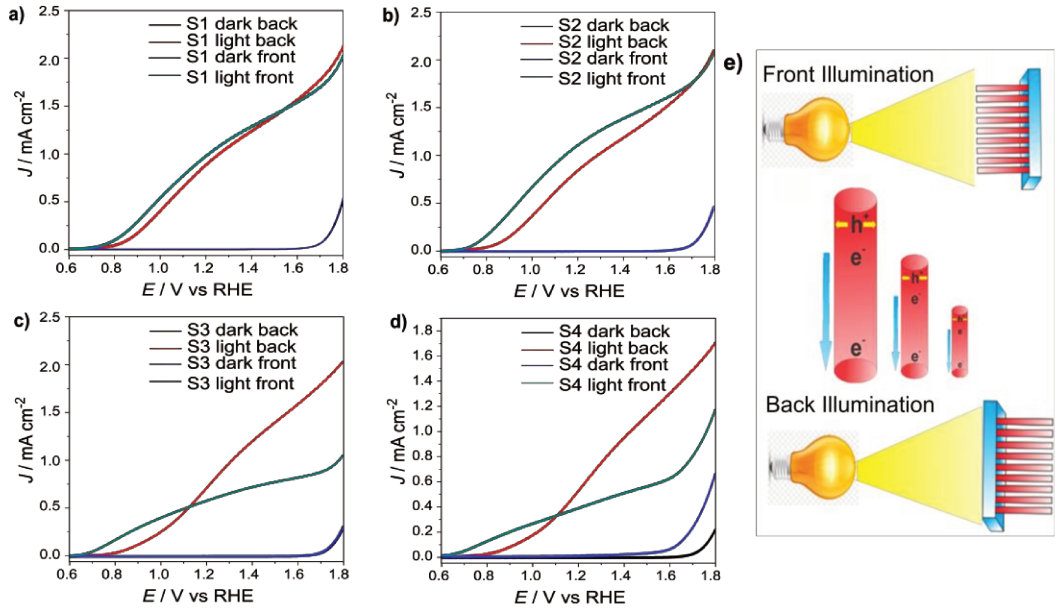


Figure 2.8: Photocurrent density (mA cm^{-2}) vs V_{RHE} (I-V curves) applied potential of a) S1, b) S2, c) S3 and d) S4 α-Fe_2O_3 photoanodes and e) schematic illustration of front and back illumination on nanorod-based films.

It is well known that α-Fe_2O_3 photoanodes require an annealing treatment at high temperature for a short period of time to improve their activity towards water oxidation.[137] Qiu *et al.*[145] reported that the enhanced PEC performance of α-Fe_2O_3 photoanodes annealed at high temperatures is due to the fine-tuning of the crystallite size and it is also related to the diffusion and incorporation of Sn atoms from the conducting layer during the annealing process. Both effects act by suppressing the charge carrier recombination through reduction in the charge transport resistance. Despite the improvement promoted by the high annealing temperature in the overall α-Fe_2O_3 performance, it is worth mentioning that the beneficial contribution of Sn^{+4} diffusion from the conductive substrate and its incorporation into α-Fe_2O_3 structure remains controversial for thicker films.[146]

Considering the parameters affected by high-temperature annealing on α-Fe_2O_3 structure and the low-thermal stability of graphene-based materials, the

transfer of SLG over the α-Fe_2O_3 photoanodes was conducted after annealing at 750°C for 30 min. The SLG was synthesized via CVD on copper foil and subsequently transferred onto the α-Fe_2O_3 film. The CVD technique is a prominent way to allow the growing of uniform monolayer graphene with high quality in large scale using methane (CH_4) as precursor.[147] The chemical composition of graphene film grown by CVD on copper foil was evaluated by X-ray photoelectron spectroscopy (XPS), shown in Figure 2.9. The XPS overview spectrum confirms the presence of carbon, oxygen and copper without any additional elements. C 1s XPS spectrum can be deconvoluted into a strong peak at 284.5 eV, attributed to C-C bonds and the C-O peak at 286 eV[148] due to the presence of carbonic gas adsorbed at the surface of the sample. The analysis reveals 91.2% of carbon atoms in the structure with oxygen impurities. As described in the experimental section, the SLG was added over the α-Fe_2O_3 nanorods after the chemical etching of the copper foil to avoid any trace of residual copper atoms and the contribution of this metal in the photoelectrochemical measurements. Although the transfer of graphene (SLG) from Cu foil to a specific substrate is hard to accomplish, the final quality of graphene is not altered in most of the cases due to graphene's robustness.[149]

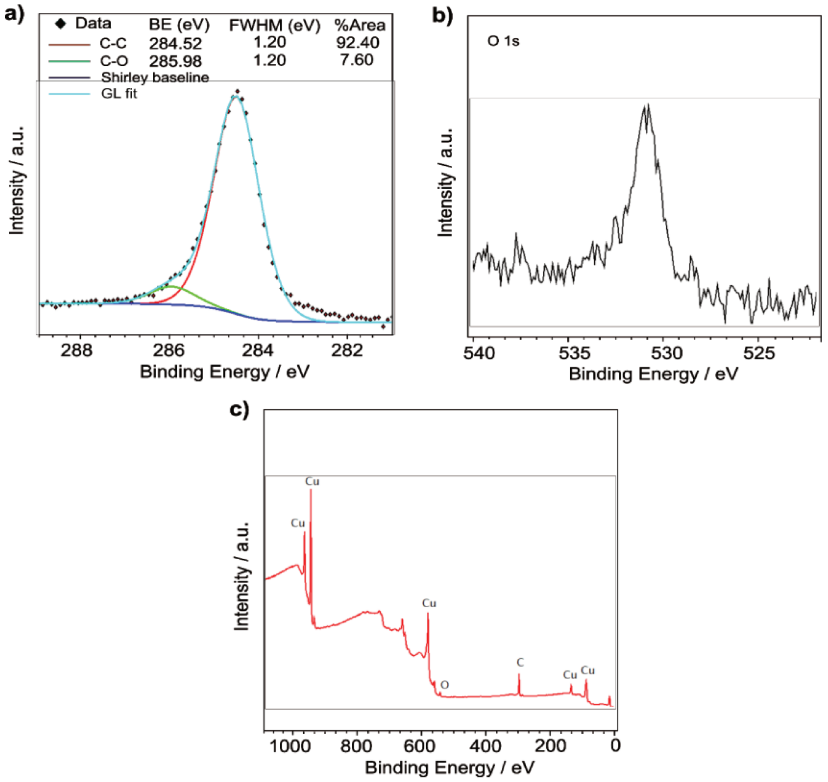


Figure 2.9: a) C 1s deconvolution show C-C bonds with the expected energy of 284.52 eV and 285.98 eV (C-O bonds are due to adsorbed carbonic gas and other carbon oxide residues), b) O 1s does not show any more complex oxidation states and c) XPS full spectrum (survey) of graphene (CVD) film on copper foil.

FEG-SEM images exhibit the morphology of the α-Fe_2O_3/SLG (Figure 2.10a) and bare α-Fe_2O_3 films(Figure 2.10b and c). It can be observed that the α-Fe_2O_3 nanorods are entirely covered by an ultrathin and transparent layer of graphene after its transfer from the copper foil film. The optical properties were evaluated in terms of absorbance and the results show that the SLG layer compared with the bare α-Fe_2O_3 nanorods slightly affects the absorption owing to its high transparency (Appendix A - Figure A1) and should not interfere the UV light excitation of α-Fe_2O_3. Cross section profiles FEG-SEM images of bare α-Fe_2O_3 photoanode are shown in Figures 2.10b and c and depict the Fe_2O_3 nanorods deposited onto FTO substrate. After SLG deposition, the cross section of two different regions of α-Fe_2O_3/SLG photoanode was analysed by FEG-SEM, as shown in Figure 2.10d (spectra 1 and 2) and Figure 2.10g (spectra 3 e 4) with their respective EDX mapping. EDX spectra (Figures 2.10e and f) clearly demonstrate the higher contribution of carbon content at SLG region (spectrum 2 in Figure 2.10d) compared with α-Fe_2O_3 region (spectrum 1 in Figure 2.10d). The same observation can be seen in spectra 3 (Figure 2.10h) and 4 (Figure 2.10i) where higher content of carbon is obtained at the top of the film, indicating the presence of SLG over the α-Fe_2O_3 nanorods.

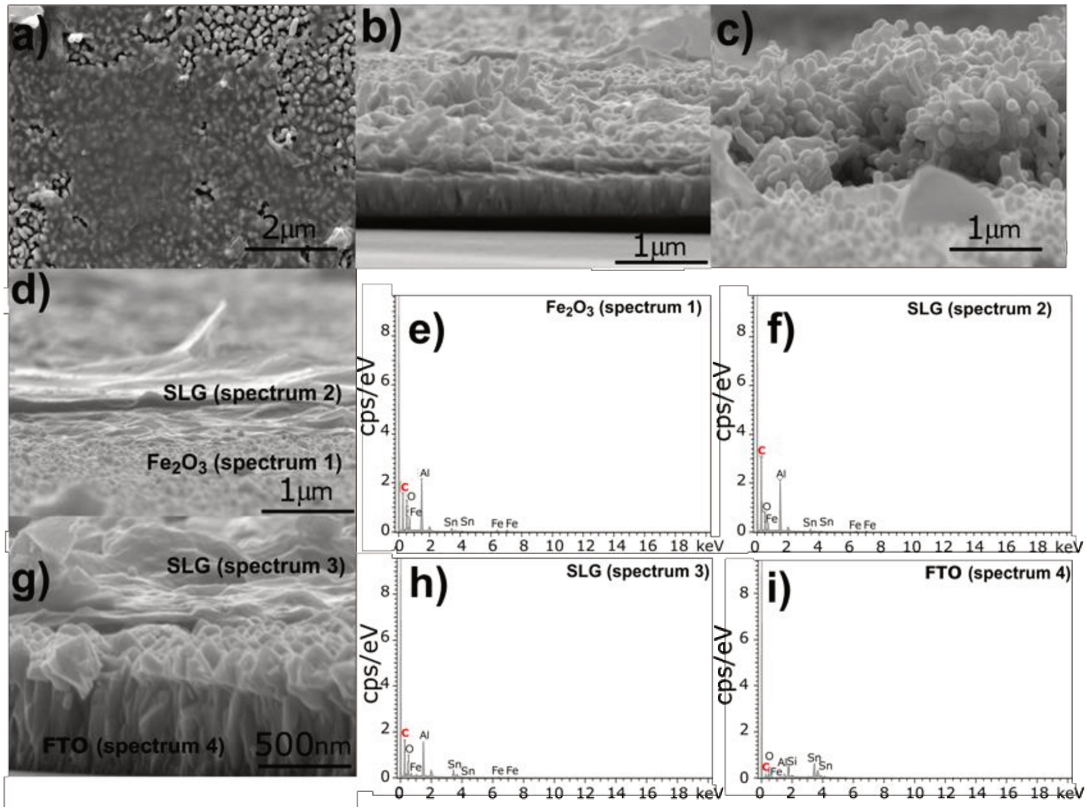


Figure 2.10: a) FEG-SEM top-view image of α-Fe_2O_3/SLG photoanode; b-c) cross sectional profile FEG-SEM image of the vertically oriented α-Fe_2O_3; d) cross sectional profile FEG-SEM image of the α-Fe_2O_3/SLG photoanode with e-f) EDX mapping spectra (spectrum 1 and 2); g)

cross sectional profile FEG-SEM image of the α-Fe_2O_3/SLG photoanode with h-i) EDX mapping spectra (spectrum 3 and 4).

Further confirmation of the successful deposition of high-quality graphene can be revealed by Raman spectroscopy. Figure 2.11a shows the Raman spectra of graphene on FTO, α-Fe_2O_3 and α-Fe_2O_3/graphene films. The α-Fe_2O_3 sample shows peaks at 407 (E_g), 495 (A_{1g}), 596 (E_g) and 1272 cm^{-1} (two-magnon scattering) exhibiting the spectral signatures for hematite.[54] Graphene shows the fingerprint of G (1572 cm^{-1}) and 2D (2690 cm^{-1}) bands, from the doubly generated zone center E_{2g} and second-order-zone boundary phonons, respectively.[147] The D band, which is commonly present in many graphene-based materials and related to defects, is not observed or its intensity is too small to be detected. This is strong evidence that the SLG synthesized via CVD has a negligible amount of defects in its framework, which is highly desirable for photocatalytic applications. Moreover, the very sharp and intense 2D-band and low G-band with the 2D/G ratio in Figure 4a suggest the existence of single layer graphene on the copper foil.[150] G and 2D bands on α-Fe_2O_3/graphene film are slightly shifted to lower energies (1572 to 1537 cm^{-1} and 2690 to 2614 cm^{-1}, respectively) due to a possible strain in graphene emerged after its transference[151,152] indicating a possible interaction between the oxygen atoms from the Fe_2O_3 nanorods and the carbon atoms in the SLG; such interaction is expected to decrease C-C bond energies.

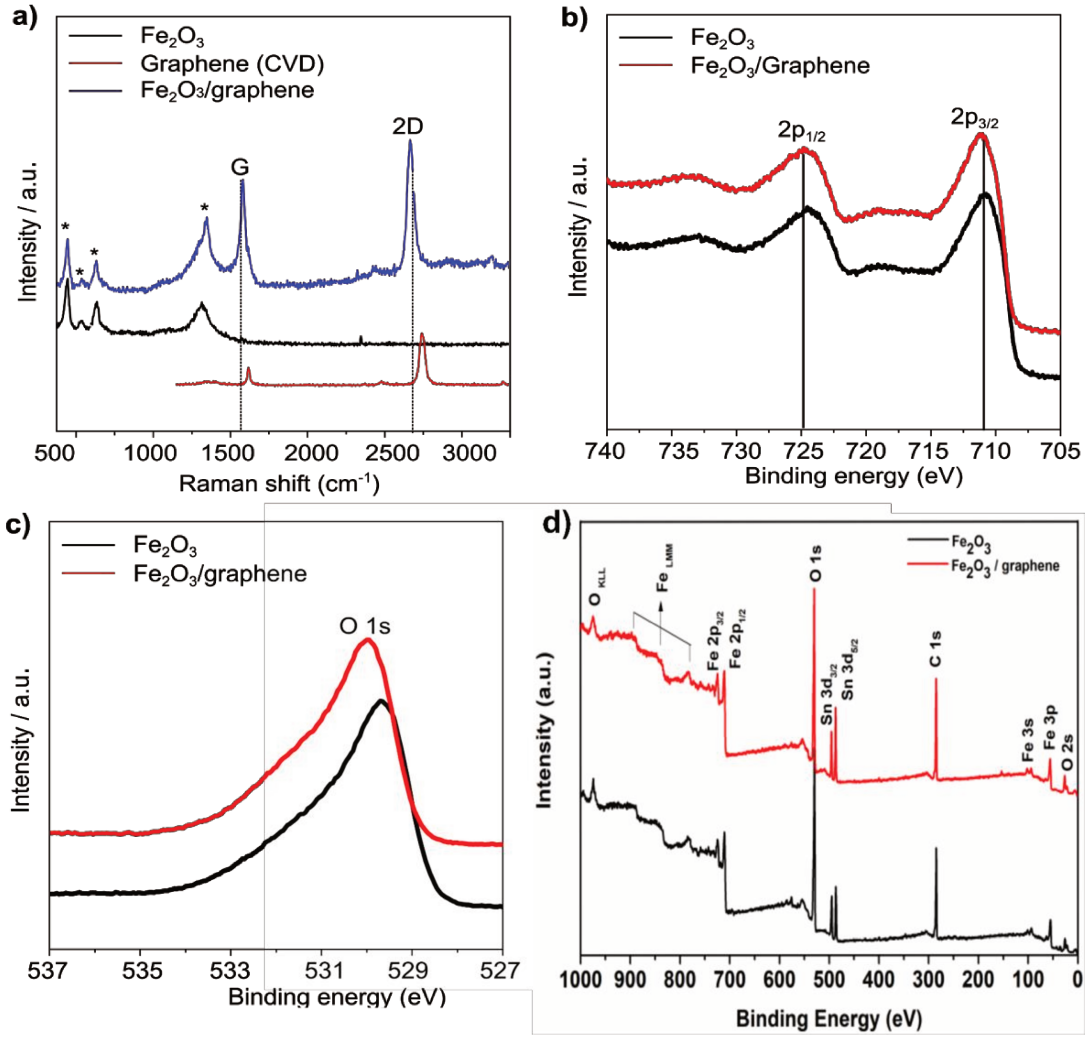


Figure 2.11: a) Raman spectra of α-Fe_2O_3 (black), graphene (red) and α-Fe_2O_3/graphene (blue) films; XPS scans of α-Fe_2O_3 (black) and Fe_2O_3/SLG films (red) of b) Fe 2p core level with pronounced peaks for orbital split of Fe $2p_{1/2}$ and $2p_{3/2}$, c) O 1s and d) survey spectra.

XPS analysis of the as-prepared α-Fe_2O_3 and α-Fe_2O_3/graphene films was carried out to evaluate their chemical composition. For the α-Fe_2O_3 film, the XPS of the Fe 2p core level is evaluated, as shown in Figure 2.11b. It is observed an orbital split of Fe $2p_{1/2}$ and Fe $2p_{3/2}$ peaks at 710.75 eV and 724.50 eV, respectively, as expected for iron oxide. For α-Fe_2O_3/SLG sample, it is noticed a slight shift to higher binding energy for the Fe $2p_{3/2}$ peak position (711 eV), but this could not be related to the presence of SLG overlayer. For all samples, the satellite peak around 719 eV suggests the presence of Fe^{3+} species and the absence of Fe^{2+} ions. O 1s spectra (Figure 2.11c) show a shift of 1 eV to higher binding energy comparing the pristine and SLG-modified material. This shift has been already reported as an effective tight contact formed between Fe and C carbon atoms connected by oxygen atoms bridges (Fe-O-C) at the

surface.[153] Another work described van der Waals chemical interaction between graphene and other metal oxides (e.g. TiO_2), which is a further evidence of a strong interaction between oxygen from the Fe_2O_3 surface and graphene layer.[153,154] To ensure that the total Cu foil was removed from the SLG layer the full XPS survey is presented in Figure 2.11d. As clearly shown, no trace of this metal (Cu foil) used to support the synthesized SLG has been detected.

To elucidate the impact of SLG on the α-Fe_2O_3 PEC performance, linear sweep voltammetry (LSV) under simulated illumination (front side) was carried out. To ensure that the response corresponds only to α-Fe_2O_3 photoanodes, the photocurrent density of the SLG deposited onto bare FTO substrate was measured (Figure 2.12a). Therefore, as no trace of metal has been detected (XPS survey in Figure 2.11d) and a slight change in absorption is observed with the SLG deposition, no significant. activity under simulated sunlight is expected. Indeed, only a small photocurrent density in the range of μA was measured during the PEC experiment, which is negligible in comparison to those obtained for α-Fe_2O_3 (1.25 mA cm^{-2}) and α-Fe_2O_3/graphene (1.64 mA cm^{-2}) photoanodes. Figure 2.12b shows the photoactivity of α-Fe_2O_3 and α-Fe_2O_3/SLG photoanodes under applied bias (0.2 - 1.8 V_{RHE}).

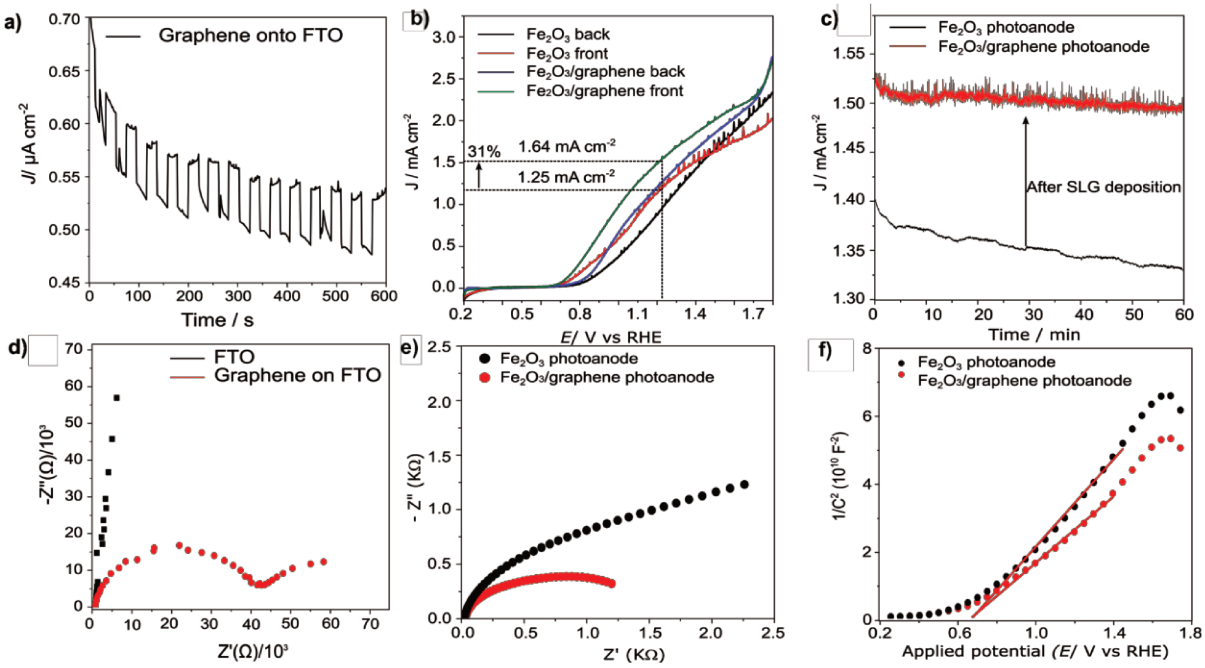


Figure 2.12: a) Photocurrent density vs time measurement at 1.23 V_{RHE} under chopped illumination of graphene onto FTO substrate; b) photocurrent density (mA cm^{-2}) vs. potential curves and c) long-term photocurrent stability over time of α-Fe_2O_3 and α-Fe_2O_3/graphene photoanodes under illumination. All measurements were performed in 1 M NaOH solution (pH = 13.6); d) Nyquist plots in the dark of FTO

and SLG deposited on FTO; e) Nyquist and f) Mott-Schottky plots obtained by EIS of α-Fe_2O_3 and α-Fe_2O_3/SLG photoanodes The Mott-Schottky measurements were performed at 1-100 kHz frequency in the dark.

The incorporation of SLG onto α-Fe_2O_3 film surface leads to an enhancement of 31% in the photocurrent values at the water oxidation potential (1.23 V_{RHE}), from 1.25 to 1.64 mA cm^{-2}. Furthermore, it is noticed a cathodic shift of ~100 mV comparing the pristine and SLG-modified photoanodes, indicating a passivated surface by the carbon-based material. This behaviour is probably due to the higher conductivity of the α-Fe_2O_3/SLG material, when compared with that of the pristine α-Fe_2O_3 photoelectrode. In addition, the photostability is confirmed when 1.23 V_{RHE} is applied under 1 h of simulated sunlight irradiation (Figure 2.12c), indicating that the SLG was not removed from the α-Fe_2O_3 surface, even under long period of applied bias. Besides, the α-Fe_2O_3/SLG photoanode is demonstrated to be even more stable than the pristine material.

The positive effect of graphene incorporation on the photoactivity of many semiconductors has been extensively reported.[155–157] The understanding of the role played by the graphene is crucial for the development of new graphene-based devices which is still an open question. Cardona *et. al* [131] reported electrical impedance spectroscopy (EIS) studies for the first time on Ti-doped hematite photoanodes after the incorporation of the SLG. The authors claimed that the improvement of the photocurrent density is related to a decrease in the surface recombination rate.

To shed some light on the role of SLG incorporation onto α-Fe_2O_3 nanorods surface, EIS under dark conditions was carried out to evaluate the electronic properties of the photoelectrodes. Firstly, EIS experiment was carried out on bare FTO and SLG/FTO, as shown in Figure 2.12d. The bare FTO exhibits a resistive behaviour in comparison with the SLG/FTO that shows a well-formed semicircle. In fact, the FTO does not contribute to the overall photoactivity as expected, while the EIS results for FTO-SLG confirmed the high quality of the graphene sheet that is used here. Afterwards, the EIS data for α-Fe_2O_3 and α-Fe_2O_3/SLG photoanodes were analysed in terms of Nyquist and Mott-Schottky plots (Figure 2.12e,f).

Nyquist plots (Figure 2.12e) show that the SLG has a positive impact on the α-Fe_2O_3 surface by reducing the charge transfer resistance at solid-liquid interface compared with that of the pristine α-Fe_2O_3 photoanode. Mott-Schottky plot (Figure 2.12f) provides information about flat band potential (V_{fb}), donor density (N_D)

and it enables the calculation of the depletion layer width (W) and the onset (n_{ox}) potential. The calculated parameters for α-Fe_2O_3 and α-Fe_2O_3/SLG photoanodes are: N_D varies from 3.94 10^{19} to 4.52 10^{19} cm^{-3}; V_{fb} = 0.60 to 0.64 V_{RHE}; W = 20 to 18 nm and n_{ox} = 0.13 to 0.14. As already reported, the addition of SLG over α-Fe_2O_3 surface does not cause significant changes in the electronic parameters, besides the reduction of the resistance to charge transfer, suggesting a surface passivation effect,[158] which means that the single EIS data are not sufficient to elucidate the complete effect of the SLG overlayer.

The charge separation processes that take place in photocatalysts are mostly studied by electrical and optical changes, limiting the information about the yield and decay dynamics of the photogenerated charge carriers.[98] To get knowledge on how the charge carrier dynamics is influenced by the SLG coating onto the hematite surface, IPCE, TAS and SPS measurements were carried out (Figure 2.13). These powerful techniques are able to provide additional information about charge carrier lifetime[92,159] and photochemical charge separation and transport.[102]

IPCE data as a function of wavelength (λ) plots for the α-Fe_2O_3 and α-Fe_2O_3/SLG photoanodes were obtained by collecting the photocurrent values recorded under monochromatic light irradiation. This measurement is carried out in order to investigate the change in the photoresponse of a photoanode as a function of the irradiation wavelength. In Figure 2.13a, it is observed a pronounced enhancement of the IPCE values (at 1.23 V_{RHE}) for α-Fe_2O_3/SLG photoanode when compared with pristine α-Fe_2O_3 photoanode. At short wavelengths, the IPCE values for α-Fe_2O_3/graphene are two times higher than those for the α-Fe_2O_3 photoanode, reaching the maximum of 32% at λ = 300 nm. The improvement on the IPCE values for α-Fe_2O_3/graphene photoanode indicates that more photons were converted to photocurrent when SLG is coating the α-Fe_2O_3 surface.

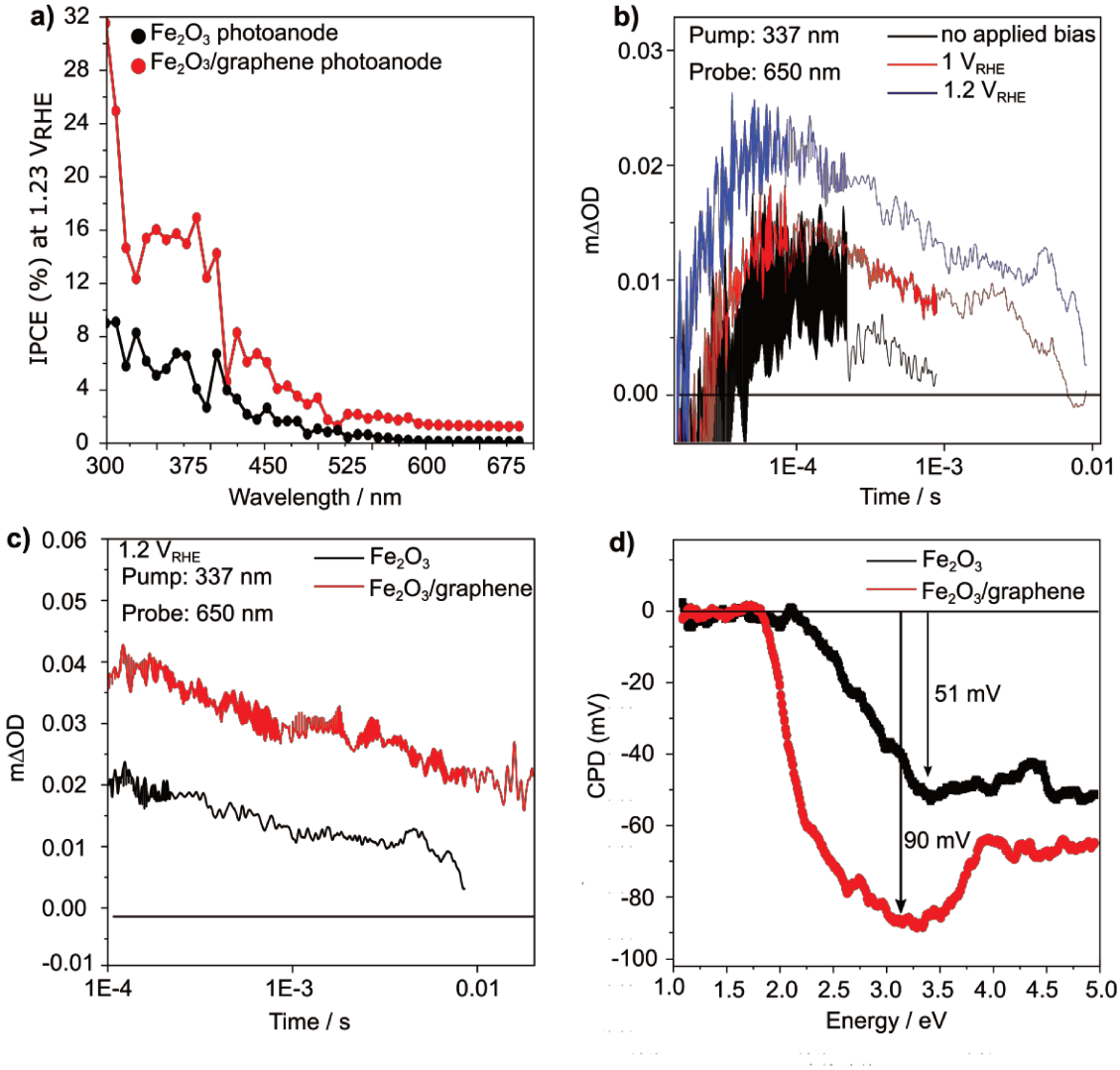


Figure 2.13: a) IPCE plots of α-Fe_2O_3 and α-Fe_2O_3/SLG photoanodes at 1.23 V_{RHE} in 1 M NaOH aqueous solution; transient absorption kinetic decays of b) α-Fe_2O_3 photoanode as a function of applied bias, c) α-Fe_2O_3 and α-Fe_2O_3/SLG photoanodes under 1.2 V_{RHE} of applied bias and d) SPS spectra of α-Fe_2O_3 and α-Fe_2O_3/SLG photoanodes under vacuum conditions.

The dynamics of the photogenerated holes in α-Fe_2O_3 photoanodes can be estimated (Figure 2.13b) with the help of pulsed lasers as excitation source, leading to the formation of electron-hole pairs followed by probing the transient species.[82] The μs-s transient absorption signals for α-Fe_2O_3 and α-Fe_2O_3 /SLG photoanodes were recorded in NaOH aqueous solution in the absence of sacrificial agents.

Firstly, α-Fe_2O_3 excited state decay was recorded in the absence and presence of external bias. The unbiased α-Fe_2O_3 photoanode exhibits ultrafast charge recombination and smaller amplitude of the transient signal. A longer decay phase and an increase in the amplitude of the signal are observed under applied bias of 1 and 1.2

V (*vs.* RHE), indicating that more positive potentials lead to more photogenerated holes, thereby increasing their lifetime.[105]

Minimizing or even supressing the ultrafast electron/hole recombination in α-Fe_2O_3 photoanodes is desirable in order to improve the water oxidation reaction (OER). TAS measurements were also carried out for α-Fe_2O_3/SLG photoanode at 1.2 V_{RHE} (Figure 2.13c). At this potential, much longer hole lifetime accompanied by a gain in the transient signal is obtained, indicating the positive effect of the SLG in assisting the generation of more long-lived holes. The slower decay signal of the photogenerated holes exhibited by α-Fe_2O_3/SLG photoanode strong indicates an accumulation of these charges at the photoanode surface, supressing charge carrier recombination and giving sufficient holes lifetime to drive water oxidation.

SPS measurements conducted on α-Fe_2O_3/SLG photoanodes are shown in Figure 2.13d. The light-induced change of the contact potential difference (CPD) of the samples was obtained using a contactless semi-transparent Kelvin probe. The negative signal confirms the *n*-type character of α-Fe_2O_3, which means that electrons from the CB of the α-Fe_2O_3 move towards the FTO substrate and away from the tip.[98] The spectra onset provides the effective band gap value of the material, which was 2.12 eV for α-Fe_2O_3 and 1.94 eV for α-Fe_2O_3/SLG photoanodes. The band gap value of 2.12 eV for α-Fe_2O_3 is in agreement with that reported in the literature.[17] The intensity of the CPD increases from - 50 to - 90 mV upon SLG incorporation. The more negative SPV signal of Fe_2O_3/SLG photoanode indicates that more electrons are injected into FTO substrate whereas holes are accumulated at the surface of the photoanode,[100] enhancing the charge carrier separation and enabling the photogenerated holes to be available to oxidize water at the surface, corroborating with the TAS measurements.

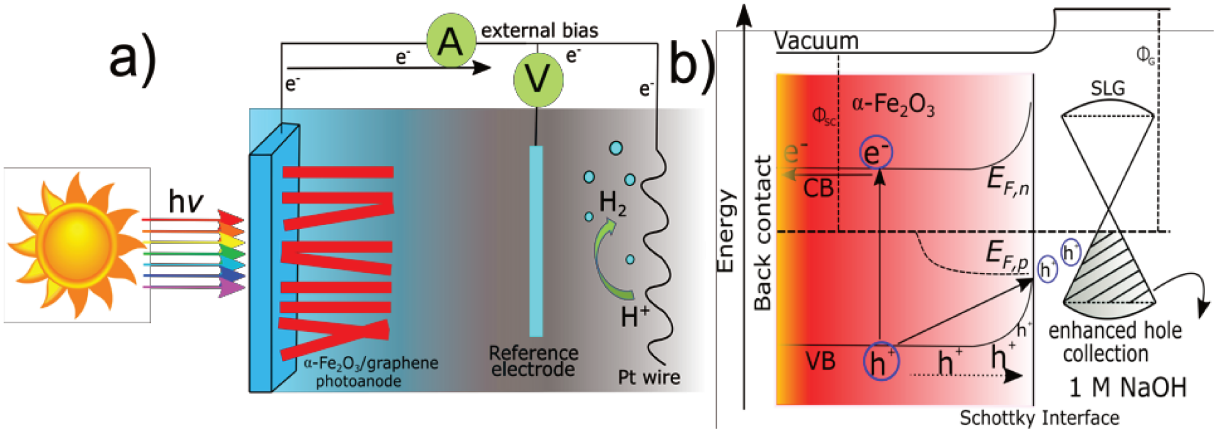


Figure 2.14: a) Schematic illustration of the PEC cell and b) the charge carrier separation that takes place at the α-Fe_2O_3/SLG photoanode surface.

In summary, EIS, IPCE, TAS, and SPS enable us to relate the enhancement in the photoelectrochemical response with the suppression of surface traps[160–162] promoted by the presence of the SLG over the α-Fe_2O_3 nanorods. The SLG passivation effect may reduce the defects on the α-Fe_2O_3 nanorods surface, removing the pinning of Fermi level[163–166] and hole traps and consequently, the water oxidation reaction efficiency is increased (Figure 2.14). In fact, the water oxidation kinetics become faster and more efficient provided by the SLG addition. The results prove the synergistic effect of α-Fe_2O_3 and SLG materials towards water oxidation reaction (OER).

2.4 Partial conclusion

In this work, the role of the single layer graphene as overlayer on hematite photoanodes surface was investigated for water oxidation reaction via photoelectrochemical process. The photocurrent density of α-Fe_2O_3/graphene photoanode was increased from 1.25 to 1.64 mA cm^{-2} at 1.23 V_{RHE} in comparison to bare α-Fe_2O_3 photoanode. This photocurrent value was observed to be higher than those reported in the literature using also SLG as overlayer on α-Fe_2O_3 photoanodes.

The use of different techniques to characterize the α-Fe_2O_3/graphene materials provided novel insights about the role of SLG added over the α-Fe_2O_3 nanorods photoanodes for driving the water oxidation reaction induced by simulated sunlight. The techniques applied in this first part of the thesis were of great value to evaluate the charge carrier dynamics and show that the SLG can act suppressing the surface traps, increasing the lifetime of the photogenerated holes and electrons and consequently enhancing the material performance. The SPV and TAS techniques revealed that in the presence of SLG sheets, more electrons moved from the α-Fe_2O_3 conduction band towards the FTO substrate, whereas the photogenerated holes are captured by the ultra-thin graphene overlayer moving to the photoanode-electrolyte interface. Therefore, the present results confirm the suppression of electron-hole recombination and the faster water oxidation kinetics upon the incorporation of SLG and consequently the increase in the photocurrent density of Fe_2O_3/graphene photoanode. Further experiments are necessary to optimize the interface between Fe_2O_3 and graphene sheets in order to increase the photocurrent density.

Chapter 3

Surface modification of α-Fe_2O_3 photoanodes with cobalt hexacyanoferrate (Co-NC-Fe): The role of the mixed oxidized states on the enhancement of PEC performance

In this chapter, it will be discussed a general introduction of the fundamental aspects of Prussian-blue analogues and their use as effective electrocatalysts for enhanced PEC performance after modification of α-Fe_2O_3 photoanode surface. *In-situ* techniques will be employed for better characterize the photochemical changes during PEC water oxidation.

3.1 Theoretical Background

3.1.1 Prussian Blue (PB)

Prussian blue (PB), also known as Berlin blue or Paris blue, was the first purely synthetic pigment and is a dark pigment synthesized by oxidation of ferrous ferrocyanide salts, leading to the chemical formula $Fe_4^{III}[Fe^{II}(CN)_6]_3$. It is an inorganic material of mixed valence in a tridimensional framework composed by Fe^{II} bound to Fe^{III} through a cyanide (CN^-) bridge to construct a face-centered cubic unit cell.[167] Prussian blue analogues (PBAs) are representative cyanide-based coordination polymer materials and due to the adjustable metal active sites, PBAs have been found auspicious application in electrocatalytic water splitting, exhibiting great performance for OER.[168]

PBAs have been described as good candidates for solving the modern challenges for energy storage.[169] For instance, a wide range of analogues generally show high capacity for thousands of cycles and fast reversible kinetics for potassium and sodium ion aqueous batteries.[170] In case of water splitting, PB-type materials have emerged as promising candidates as electrocatalysts towards water oxidation, and can be expressed as $A_xFe[Fe(CN)_6]_y.mH_2O$, where A is an alkaline metal; $0 < x < 2$, $y < 1$.[171]

3.1.2 Cobalt Hexacyanoferrate (Co-NC-Fe)

Cobalt hexacyanoferrate (Co-NC-Fe), which has an analogous structure to PB, is a robust, effective and inexpensive electrocatalyst and has shown good electrocatalytic activity owing to its both fundamental and practical perspectives.[172,173] This material is very competitive with state-of-the-art metal oxides and exhibits long-term stability at neutral pH and ambient conditions,[168] making it promising WOC (water oxidation catalyst) candidate in solar fuels manufacturing. Due to its high porosity and susceptibility for incorporation interstitial solvent molecules and alkali metals, Co-NC-Fe becomes a versatile type of electrocatalyst-based materials in very different fields.[174,175] Compared to others cobalt-based electrocatalysts such as CoPi, Co-NC-Fe exhibits much faster water oxidation kinetics ($1.4\ s^{-1}$ for Co-NC-Fe vs $2 \times 10^{-3}\ s^{-1}$ for CoPi) for each active site.[176,177] Such peculiar

properties as electrochromism and sensing are based on electron transfer between Fe^{III} and Co^{II} ions in its structure.[178–181] Its application in oxygen evolution reaction (OER) has been already studied in both basic[182] and neutral[168] media and more recently the material has shown improved performance also in acidic conditions.[183] The outstanding performance of these catalysts is attributed to their structural and electronic properties. The coordination networks are robust owing to the strength of cyanide (CN^-) bridging with high covalent character.[184] Owing to their porosity, open framework and structural stability, these catalysts present benefits to ion diffusion.[185]

Figure 3.1a shows the schematic illustration of the regular crystal structure of cobalt-iron analogue of PB, considered active for water oxidation in PEC systems. It contains cobalt atoms where water oxidation takes place. It has been reported that the colour of the oxidized state of Co-NC-Fe will depend on its chemical composition.[186] Basically, Co-NC-Fe presents two oxidized states with different spin configurations:

$$A_yCo^{3+}[Fe^{2+}(CN)_6]_{1-x} \rightarrow Co^{III}/Fe^{II} \text{ (blue)}$$
$$A_yCo^{2+}[Fe_{3+}(CN)_6]_{1-x} \rightarrow Co^{II}/Fe^{III} \text{ (red)}$$

where the spin state depends on their vacancy ratio, and in the case where there is a mixed oxidized state, the colour exhibits brown aspect (Figure 3.1b). The CN^- groups bridge the two metal ions, where Fe atoms are linked to the carbon side of CN^- and Co species are linked to the nitrogen side.

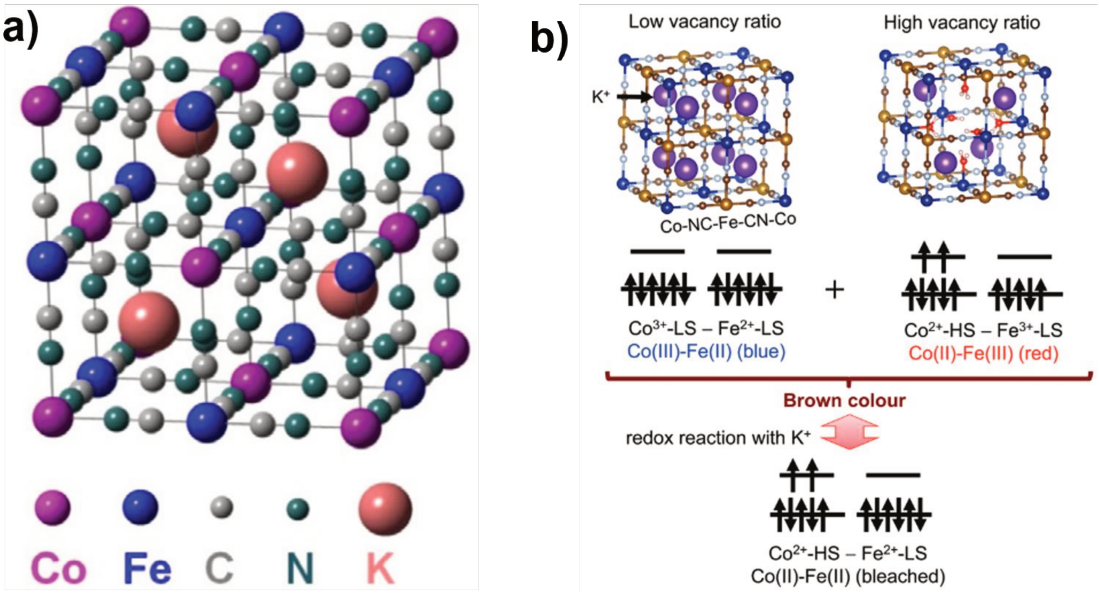


Figure 3.1: A) Representation of the face-centered cubic unit cell of the Co-NC-Fe ($KCo[Fe(CN)_6]$)[184] and b) schematic view of the crystal structure of low and high vacancy ratio with valence/spin-states.[186]

Co-NC-Fe is of particular interest from fundamental and practical perspectives due to its versatility and good electrocatalytic activity. Both cobalt and iron atoms exist in two common oxidation states (II and III) within the structure, leading to myriad of compound stoichiometries and redox configurations.[187] When both cobalt and iron undergo reduction (from III to II oxidation state), cations must move into the Co-NC-Fe structure to maintain its electroneutrality. Co-cations are usually alkali metals, which in case of Co-NC-Fe is K^+ (Figure 3.1b), and they occupy tetrahedral sites in the lattice.

Optically switchable materials have been extensively studied owing to their potential application in light-based devices, including optical and sensors. More recently, their light-induced properties have been widely evaluated, in order to better understand the elementary mechanisms that take place under dark and light conditions.[188] For instance, in CsCoFe, where Cs^+ is the alkali cation, there are two electronic configuration for Co-Fe pairs, diamagnetic ls-ls $Fe^{II}(S=0)$-$Co^{III}(S=0)$ and the paramagnetic hs-ls $Fe^{III}(S=1/2)$-$Co^{II}(S=3/2)$, in which light-induced effects allow switching between the two states. It has been reported that under illumination, electron transfer from Fe^{II} to Co^{III} takes place with concomitant spin change to the higher entropy $Fe^{III}(S=1/2)$-$Co^{II}(S=3/2)$ configuration, leading to a expansion of Co-N bonds by about 0.2 Å and lattice expansion.[188]

It has been already reported that Co-NC-Fe produces substantial improvements in both onset potential and a remarkable 6-fold enhancement of the photocurrent after its deposition onto $BiVO_4$ photoanodes.[184] Such improvements has been assigned to the adequate alignment of the VB levels of $BiVO_4$ and Co-NC-Fe, favouring more efficient interfacial hole transfer, presumably via Co t_{2g} in Co-NC-Fe. More recently, studies focused on understanding the charge carrier dynamics of Co-NC-Fe-based photoelectrodes for enhanced PEC performance have been described. Moss and co-workers[176] shows the evidence of fast hole transfer (< ms) from $BiVO_4$ to Co-NC-Fe even at low positive bias, leading to cathodic shift of onset potential (up to 0.8 V).

3.1.3 α-Fe_2O_3/Co-NC-Fe compound for PEC water splitting

The formation of α-Fe_2O_3 nanorods perpendicularly oriented to the FTO substrate improves electron transfer along [110] direction, as shown in a previous work.[81] However, its performance as bare photoanode is still far from its theoretical

predictability, and the addition of Co-NC-Fe on α-Fe_2O_3 photoanodes to enhance water oxidation kinetics with respect to surface recombination presents a promising alternative as an excellent water-oxidation catalyst (WOC). Hegner and co-workers[189] determined by DFT calculations that there is no allowed hole transfer in α-Fe_2O_3/Co-NC-Fe, due to the misalignment of their energy levels, turning charge transfer not favorable. However, after its incorporation on α-Fe_2O_3 photoanode, its photocurrent density is improved, which was assigned to be a consequence of hole-scavenging character of the interface and the suggestion of different hole-transfer pathways, including tunneling or hopping processes.

In the present study, in order to improve even further the solar-driven water oxidation, the modification of its surface with Co-NC-Fe was carried out by dip-coating method. To gain deeper understanding into the water oxidation mechanisms, the combination of different techniques, especially *in situ* and/or *operando* is of great value for advancing the development of novel electrocatalysts for PEC water splitting.[190,191] Such techniques provide conditions to analyze charge dynamics, reaction intermediates, electrode surfaces and interfaces.[192–194] One example is the use of *in-situ* FTIR spectroscopy which makes possible to investigate the fundamental aspects of interfacial processes allowing to advance planning the synthesis of prospective photocatalysts for water splitting.[195–197]

In the following, fundamental studies of the chemical processes that occur during water oxidation on α-Fe_2O_3/Co-NC-Fe photoanodes are discussed. Despite better PEC performance of α-Fe_2O_3 photoanodes upon Co-NC-Fe incorporation has been already shown[183,189] the major cause of this improvement is still unknown. In addition, the effect of different oxidation states of Fe and Co species in Co-NC-Fe analogues structure on their PEC properties was investigated. As mentioned, both cobalt and iron exist in II and III oxidation states within the as-prepared Co-NC-Fe structure, leading to different and complex redox processes under applied bias in the absence and presence of light illumination.[188] It was found that the Co-NC-Fe containing Fe^{III} is more active for PEC performance, in which the presence of Fe^{III} seems to be essential to boost the photocurrent density. *In situ* techniques suggest that the reversibility of Fe^{II}/Fe^{III} redox processes in crucial for enhanced PEC performance of α-Fe_2O_3/Co-NC-Fe photoanode.

Objectives

The goal of this second part of the thesis is to better understand the mechanisms that take place on α-Fe_2O_3 photoanode after Co-NC-Fe deposition. Despite success, the knowledge about the chemical processes in hexacyanoferrate compound in α-Fe_2O_3-based photoelectrodes are still unclear. To accomplish this, *in-situ* UV-Vis and FTIR measurements will be carried out to deeply evalute the chemical changes during PEC water oxidation.

3.2 Experimental Section

3.2.1 Synthesis of α-Fe_2O_3 Nanorods and α-Fe_2O_3/Co-NC-Fe Films

The synthesis of α-Fe_2O_3 nanorods films was carried out by the same methodology described in section 2.2.1, as well as detailed elsewhere.[198] The synthesis of Co-NC-Fe materials began with precursors salts containing Fe atoms in the oxidation states of +2 ($K_4Fe(CN)_6.3H_2O$) and +3 ($K_3Fe(CN)_6$) to form Co^{II}-NC-Fe^{II} and Co^{II}-NC-Fe^{III} respectively, and subsequently added on α-Fe_2O_3 photoanodes resulting in α-Fe_2O_3/Co^{II}-NC-Fe^{II} and α-Fe_2O_3/Co^{II}-NC-Fe^{III} photoanodes. The deposition of Co-NC-Fe on α-Fe_2O_3 films was carried out by dip-coating method, by immersing α-Fe_2O_3 films first in 0.2 M potassium ferricyanide ($K_3Fe(CN)_6$ corresponding to Fe(III) and $K_4Fe(CN)_6.3H_2O$ corresponding to Fe(II)) and subsequently in 0.04 M $CoCl_2.6H_2O$ for 15 minutes eacH, as shown in Figure 3.2. The dip-coating sequential method was carried out 5 times with subsequent drying process at 100 °C between each deposition. After the final coating step, the films were washed and then dried at 80 °C for 2h. For comparison purposes, Co-NC-Fe powders without their addition on α-Fe_2O_3 films were synthesized by mixing their precursors salts and further centrifuged and dried.

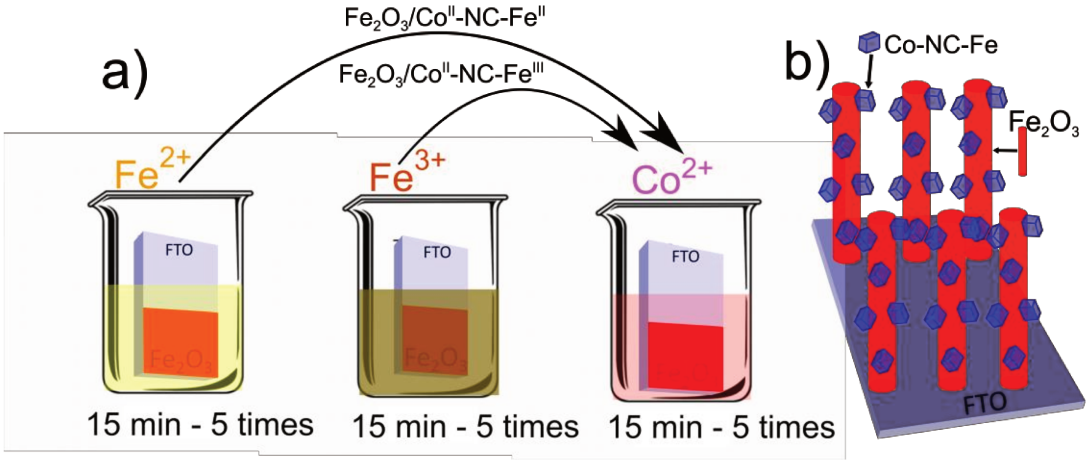


Figure 3.2: Layer-by-layer method to synthesize α-Fe_2O_3/Co-NC-Fe photoanodes with Fe atoms in their II and III oxidation states; b) illustration of the α-Fe_2O_3 nanorods modified with Co-NC-Fe nanocubes covering their surface.

3.2.2 Characterization of the materials

The as-prepared α-Fe_2O_3 and the α-Fe_2O_3/Co-NC-Fe photoanodes were characterized by FEG-SEM and XPS analyses, described in section 2.2.4.

3.2.3 PEC characterization

All PEC experiments were carried out using the same setup in section 2.2.5, where α-Fe_2O_3, α-Fe_2O_3/Co^{II}-NC-Fe^{II} and α-Fe_2O_3/Co^{II}-NC-Fe^{III} photoanodes are the working electrode and a 0.1 M KPi (KH_2PO_4/K_2HPO_4) buffer solution in pH 7, the electrolyte. LSV and CV measurements were carried out at a scan rate of 10 mV s^{-1} in the range of -0.1 to 1.2 $V_{Ag/AgCl}$. Chronoamperometry experiments were performed using the same PEC cell in 0.1 M KPi under light illumination at 0.62 $V_{Ag/AgCl}$ (1.23 V_{RHE}).

3.2.4 TAS measurements

TAS measurements at µs-s time scale were acquired by the same setup described in section 2.2.6. The measurements were conducted on α-Fe_2O_3 and α-Fe_2O_3/Co-NC-Fe photoanodes in the absence and at 0.62 V vs Ag/AgCl (1.23 V_{RHE}) of applied bias, in 0.1 M KPi (KH_2PO_4/K_2HPO_4) buffer solution.

3.2.5 *In situ* characterization: UV-Vis and FTIR spectroscopy measurements

In-situ UV-Visible (UV-Vis) absorption measurements were collected in the range of 300-800 nm at room temperature through Agilent Cary 60 UV-Vis spectrophotometer and using the same three-electrode PEC cell. All UV-Vis measurements were performed in dark conditions under applied bias from -0.1 to 1.0 V vs Ag/AgCl in 0.1 M KPi (pH 7). *In-situ* FTIR experiments were conducted on a Shimadzu Prestige-21 spectrometer equipped with a MCT detector. A three-electrode spectroelectrochemical cell with a CaF_2 window attached to the bottom of the cell was used, as described in the literature.[199] More details about the *in-situ* FTIR system used in this thesis can be found elsewhere.[200] The α-Fe_2O_3, α-Fe_2O_3/Co^{II}-NC-Fe^{II} or α-Fe_2O_3/Co^{II}-NC-Fe^{III} materials were deposited onto gold substrates and used as working electrodes (0.785 cm^2). Prior to record the FTIR spectra, the working electrodes were firstly activated by 10 cycles at 10 mVs^{-1} and then polarized at -0.1 $V_{Ag/AgCl}$ until reaching photocurrent stabilization. Each spectrum

was the average of 164 interferograms with 4 cm^{-1} of resolution in the range of 2000-2200cm^{-1}, region where CN^- stretching mode frequencies are probed in the presence of Fe and Co as function of their oxidation states. The measurements under light illumination were performed using a HAS-320 solar simulator (Asahi Spectra) with a compact xenon light source under AM 1.5 conditions. All the spectra are shown as Transmittance percentage and using the spectra taken at -0.1 V as reference. Thus, positive bands indicate the disappearance and negative bands the generation of species.

3.3 Results and Discussion

FEG-SEM images of the α-Fe_2O_3 and α-Fe_2O_3/Co-NC-Fe films revealed that the oriented α-Fe_2O_3 particles exhibit nanorod shape whereas Co^{II}-NC-Fe^{II} and Co^{II}-NC-Fe^{III}, successfully deposited over the α-Fe_2O_3 surface, show a cubic aspect. From the top-view FEG-SEM images of the pristine α-Fe_2O_3 (Figure 3.3a) and the α-Fe_2O_3/Co-NC-Fe films (Figures 3.3c and e), it can be clearly seen that the Co^{II}-NC-Fe^{II} (~144 nm) and Co^{II}-NC-Fe^{III} (~139 nm) nanocubes are not only at top of α-Fe_2O_3 nanorods (~155 nm), but also distributed between them. This result was also confirmed by EDX spectra obtained at different regions of the cross-section profile (Appendix B – Figures B1 and B2).

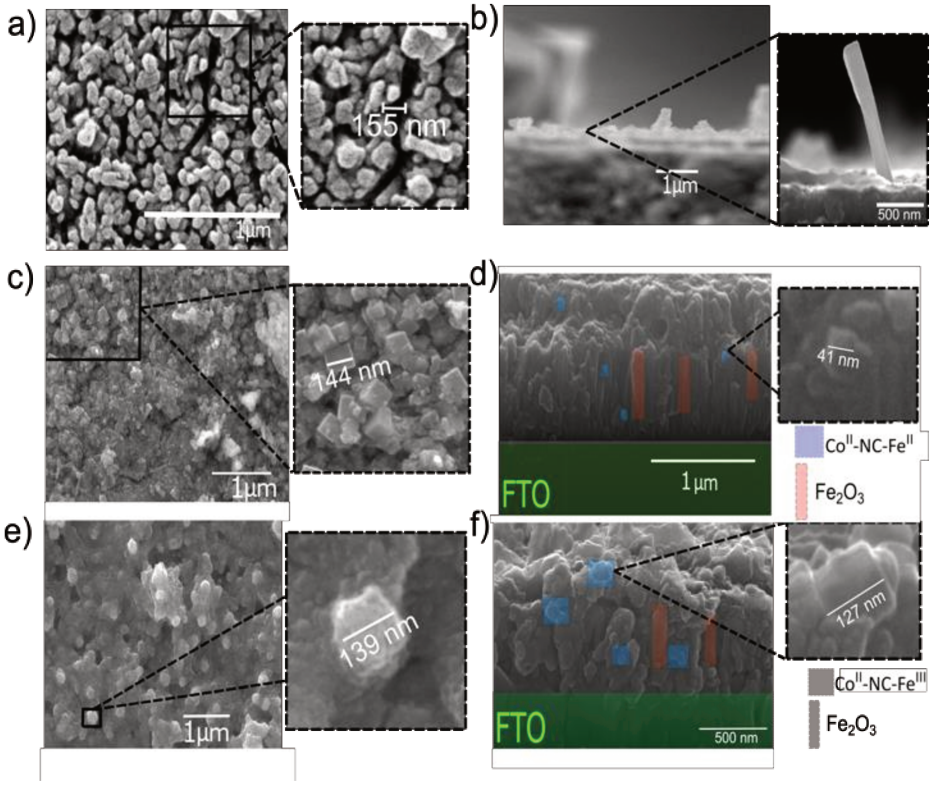


Figure 3.3: Top-view and cross sectional FEG-SEM images of (a-b) Fe_2O_3, (c-d) α-Fe_2O_3/Co^{II}-NC-Fe^{II} and (e-f) α-Fe_2O_3/Co^{II}-NC-Fe^{III}, respectively. The red and blue marks depict the Fe_2O_3 nanorods and Co-NC-Fe nanocubes, respectively.

The chemical composition as well as the oxidation states of the samples were investigated by XPS for the powder materials. The XPS survey spectra (Figure 3.4a) showed the presence of Fe and O for α-Fe_2O_3; for α-Fe_2O_3/Co-NC-Fe samples, Co and N were also identified, indicating the coverage of Co-NC-Fe on α-Fe_2O_3 (Appendix B – Figure B3). XPS spectra of the Fe 2p core levels (Figure 3.4b) show a Fe $2p_{1/2}$ peak at 721.3 eV and a Fe $2p_{3/2}$ peak at 708.3 eV corresponding to binding energies of Fe^{II} (from $[Fe(CN)_6]^{4+}$) and another peak at 723.9 eV corresponding to Fe^{III} oxidation state (corresponding $[Fe(CN)_6]^{3+}$ species). The small signal of Fe^{III} in α-Fe_2O_3/Co^{II}-NC-Fe^{II} can be attributed to Fe^{III} ions from α-Fe_2O_3 surface linked to $[Fe(CN)_6]^{4+}$.[201] According to Co 2p XPS spectra of Fe_2O_3/Co-NC-Fe samples (Figure 3.4c and d), the two distinct spin-orbital peaks of Co $2p_{1/2}$ and Co $2p_{3/2}$ centered at 797.5 and 781.8 eV correspond to binding energies of Co^{II}.[202–205] Figure 3.4d shows the same spin-orbital peaks for α-Fe_2O_3/Co^{II}-NC-Fe^{II} with negligible shift in binding energy, suggesting that Co^{II} oxidation state dominates in both material. However, in α-Fe_2O_3/Co^{II}-NC-Fe^{III}, charge transfer from Co^{II} to Fe^{III} may have occurred, resulting in a little amount of Co^{III} species.[189] where probably Co^{II} is partially oxidized to Co^{III} after mixture with hexacyanoferrate complexes in solution.

This is a result of the spontaneous electron transfer between Co^{II} and Fe^{III} that takes place right after mixing the salts, leading to more stable Co^{III}(ls, low spin)/Fe^{II} configuration.[172] Reactions 1, 2 and 3 show the possible oxidation processes resulting in Fe and Co in their higher oxidation states (III).

First oxidation process

$$K_2Co^{II}[Fe^{II}(CN)_6] \rightarrow KCo^{III}[Fe^{II}(CN)_6] + K^+ + e^- \quad \textbf{(Reaction 1)}$$

Second oxidation process

$$K_2Co_3^{II}[Fe^{II}(CN)_6]_2 \rightarrow Co_3^{II}[Fe^{III}(CN)_6]_2 + 2K^+ + e^- \quad \textbf{(Reaction 2)}$$

Third oxidation process

$$KCo^{III}[Fe^{II}(CN)_6] \rightarrow Co^{III}[Fe^{III}(CN)_6] + K^+ + e^- \quad \textbf{(Reaction 3)}$$

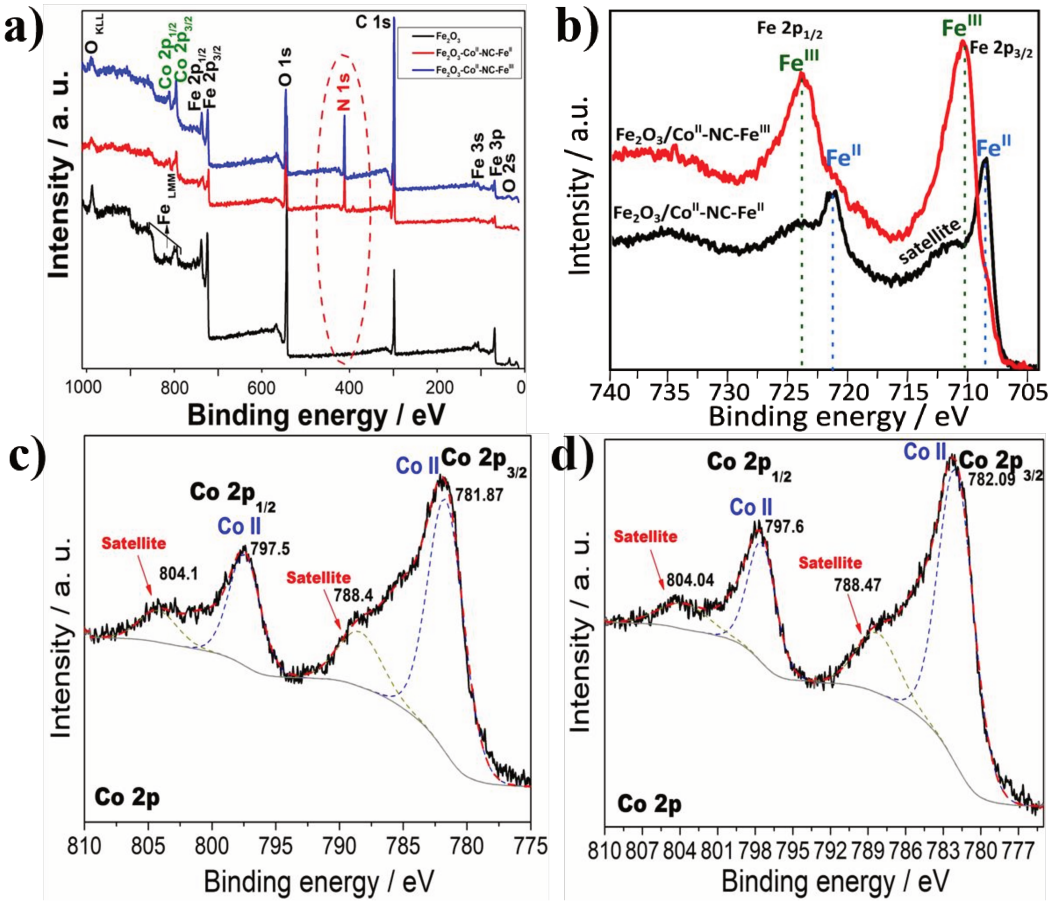


Figure 3.4: XPS a) Survey spectra of α-Fe_2O_3/Co-NC-Fe photoanodes and b) Fe 2p; Co 2p of c) α-Fe_2O_3/Co^{II}-NC-Fe^{II} and d) α-Fe_2O_3/Co^{II}-NC-Fe^{III} photoanodes.

First, it should be pointed out that Co^{II}-NC-Fe^{II} and Co^{II}-NC-Fe^{III} present bluish and reddish aspect, respectively. The characterization of Co-NC-Fe films deposited on FTO included electrochemical and *in-situ* UV-Vis measurements in phosphate buffer aqueous solution (0.1 M KPi, pH 7.0). The current-potential profiles obtained by linear sweep voltammetry revealed remarkable differences for both electrodes (Figure 3.5a). In the dark, while the FTO|Co^{II}-NC-Fe^{II} exhibited only a slight increase in current density for applied potential E > 0.7 V (vs Ag/AgCl), the FTO|Co^{II}-NC-Fe^{III} presented *ca.* 0.08 mA cm^{-2} for 0.6 V < E <0.9 V and a remarkable anodic current for E > 1.0 V, probably associated with the oxygen evolution reaction (OER). Under irradiation, both electrodes exhibited anodic photocurrent.

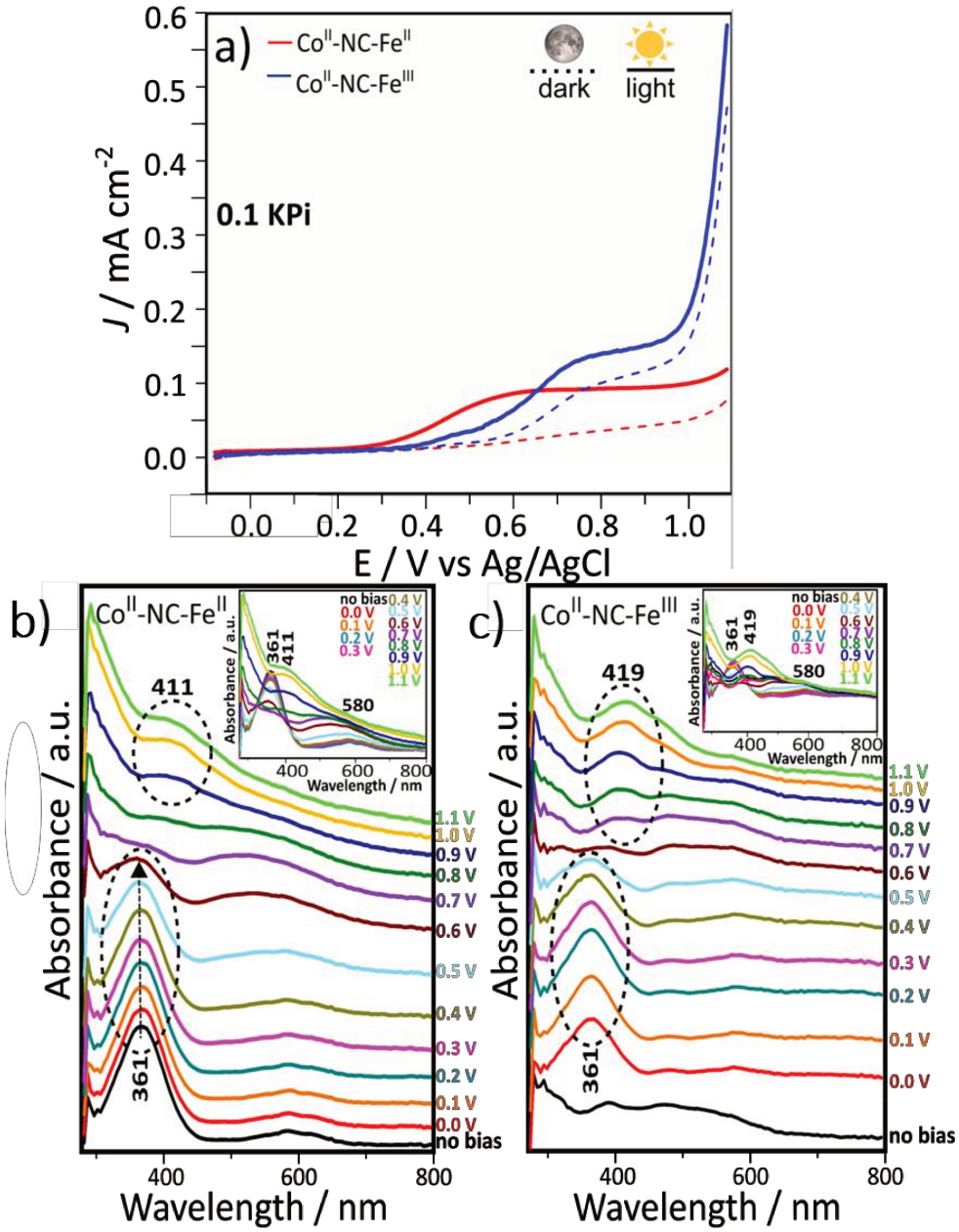


Figure 3.5: a) Current-potential profiles of FTO|Co^{II}-NC-Fe^{II} and FTO|Co^{II}-NC-Fe^{III} electrodes in phosphate buffer solution (0.1M KPi); *in-situ* UV-Vis measurements of b) Co^{II}-NC-Fe^{II} and c) Co^{II}-NC-Fe^{III} films. The inset shows the as obtained spectra as a function of applied bias (vs Ag/AgCl).

In situ UV-Vis absorption spectra of the Co^{II}-NC-Fe^{II} and Co^{II}-NC-Fe^{III} films (Figures 3.5b and c) indicate different absorption profiles with increasing the applied potential. For Co^{II}-NC-Fe^{II} film, the maximum signal at 361 nm, assigned to ligand-to-metal charge transfer (LMCT) of Co^{II}-NC-Fe^{II} units,[206] is completely quenched at 0.7 V, indicating the complete oxidation of reduced species. For Co^{II}-NC-Fe^{III} film, there is a broad charge-transfer band between 500 and 600 nm for spectrum taken for unbiased electrode, ascribed to the presence of mix-valence of Co-NC-Fe species,

$K_{0.4}Co_{1.3}[Fe(CN)_6]$ or $KCo[Fe(CN)_6]$.[207] The slightly growth of 411, 419 (MLCT, metal-to-ligand charge transfer)[178] and 580 nm (d→d electronic transition in cobalt)[208] signals with concomitant decrease of 361 nm signal as the applied potential increases may be ascribed to the formation of oxidized species, and consumption of reduced species, respectively. Additionally, the increase in band signal at 420 nm may be associated to free $Fe(CN)_6$ species and to switching between reduced Co^{II}-Fe^{II} to oxidized Co^{III}-Fe^{II}/Co^{II}-Fe^{III} states.[186] Interestingly, it is noticed that MLCT occurs at lower potential in Co^{II}-NC-Fe^{III} (Figure 3c, 0.7 V) than in Co^{II}-NC-Fe^{II} (Figure 3b, 0.9 V). Moreover, the starting electronic state of Co^{II}-NC-Fe^{III} is achieved at 0.7 V, indicating high stability over applied potential. The broadband at the region around 550 nm is assigned to the charge-transfer (CT) from Fe^{II} to Co^{III}.[209,210]

PEC measurements of bare α-Fe_2O_3, α-Fe_2O_3/Co^{II}-NC-Fe^{II} and α-Fe_2O_3/Co^{II}-NC-Fe^{III} electrodes, are shown in Figure 3.6. It is important to point out that α-Fe_2O_3 photoanodes show better PEC performance in a strongly alkaline electrolyte.[40,211] Mild conditions (neutral pH) were used herein, because PB-analogues present poor stability under alkaline conditions, in which ligand exchange between the CN^- and OH^- results in their complete dissolution.[212] As expected at this pH, a negligible photocurrent density was exhibited by the pristine α-Fe_2O_3 even at high potentials. Upon Co^{II}-NC-Fe^{II} and Co^{II}-NC-Fe^{III} depositions on the α-Fe_2O_3 electrodes (Figure 3.6a), a remarkable enhancement of the PEC performance is observed, indicating a synergistic effect between α-Fe_2O_3 and Co-NC-Fe.[41,189] Although, α-Fe_2O_3/Co^{II}-NC-Fe^{II} has its photocurrent density stabilized at 0.3 V reaching a plateau of about 0.25 mA cm^{-2}, α-Fe_2O_3/Co^{II}-NC-Fe^{III} continues to rise considerably, attaining approximately 1.1 mA cm^{-2} at 1.2 $V_{Ag/AgCl}$. Positive transients in photocurrent under light illumination, associated with the accumulation of holes at the electrode surface[213] were observed, as shown in chopped-light experiment (Figure 3.6b). Although no decrease in the current transients was observed for α-Fe_2O_3/Co^{II}-NC-Fe^{II} during the whole potential sweep, α-Fe_2O_3/Co^{II}-NC-Fe^{III} presented a considerable drop (smaller spikes) at higher potentials, indicating enhanced injection of holes from the electrode to the electrolyte, ready to drive water oxidation. The α-Fe_2O_3/Co-NC-Fe photoanodes are stable and they generate high photocurrent in the range of $mAcm^{-2}$ at neutral pH value, which is desirable for eco-friendly and commercial applications on a practical large scale.[214]

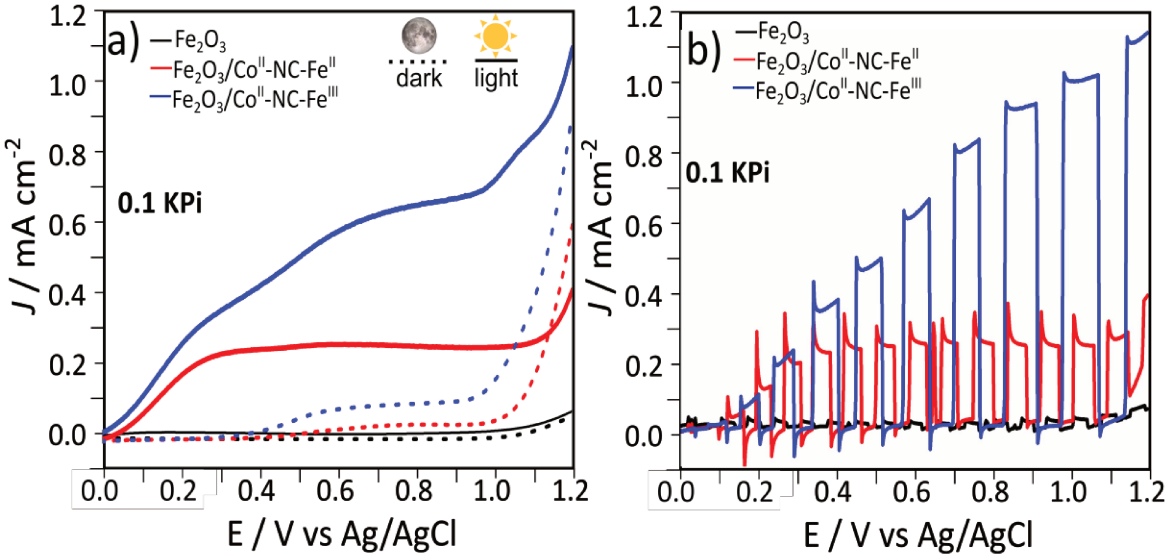


Figure 3.6: α-Fe_2O_3, α-Fe_2O_3/Co^{II}-NC-Fe^{II} and α-Fe_2O_3/Co^{II}-NC-Fe^{III} electrodes in 0.1 M KPi: a) current-potential profile in the dark and under irradiation and b) under intermittent irradiation. The measurements were performed at a scan rate of 10 mVs^{-1}.

The PEC stability of the electrodes was evaluated by chronoamperometry. The photocurrent density was measured while the electrodes were polarized at 0.62 V vs Ag/AgCl (or 1.23 V_{RHE}) during more than 10 hours (Figures 3.7a and b). The photocurrent response considerably decreased almost 75%, resulting in 0.04 $mAcm^{-2}$ for α-Fe_2O_3/Co^{II}-NC-Fe^{II} and 0.14 $mAcm^{-2}$ for α-Fe_2O_3/Co^{II}-NC-Fe^{III}, until it reaches a stability state. Surprisingly, after switching light off and on again, the J x V curves show that the photocurrent density was almost completely retrieved (Figures 3.7c and d), indicating the same performance as that obtained for freshly prepared α-Fe_2O_3/Co-NC-Fe photoanodes, indicating a negligible photocorrosion.

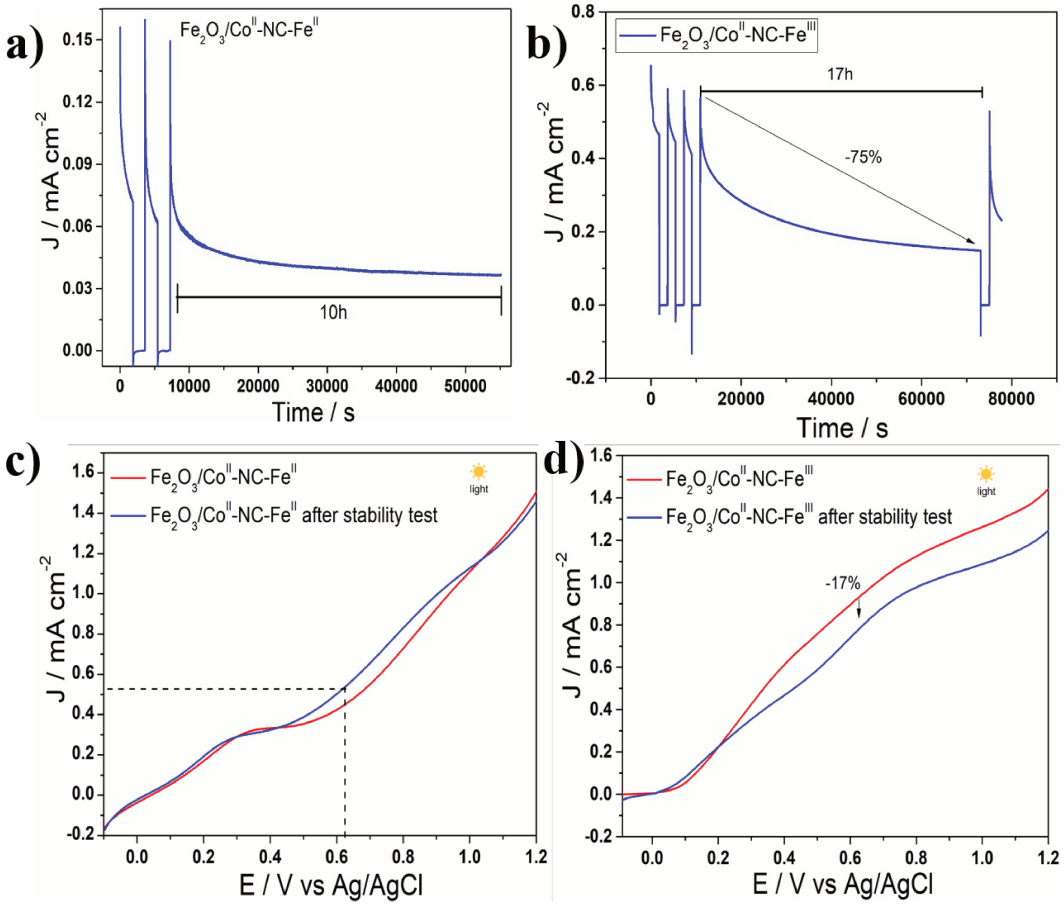


Figure 3.7: Chopped-light chronoamperometry measurements of a) α-Fe_2O_3/Co^{II}-NC-Fe^{II} and b) α-Fe_2O_3/Co^{II}-NC-Fe^{III} photoanodes; J x V curves of c) α-Fe_2O_3/Co^{II}-NC-Fe^{II} and d) α-Fe_2O_3/Co^{II}-NC-Fe^{III} and before and after long-term stability test.

Regarding the spikes associated with the accumulation of holes at the surface,[215] a chopped-light stability test was carried out at different applied potentials (0.1-1.2 V) for both α-Fe_2O_3/Co^{II}-NC-Fe^{II} (Figures 3.8a and b) and α-Fe_2O_3/Co^{II}-NC-Fe^{III} (Figures 3.8 c and d) photoanodes. The photocurrent density values were maintained for measurements performed under intermittent irradiation during 15 min. Higher spikes associated with recombination of charge carriers at lower potentials were observed, which are decreased upon increasing potential. These spikes which can be associated with the accumulation of holes at the surface, also decreased for α-Fe_2O_3/Co-NC-Fe electrodes, indicating an improvement of charge transport upon Co-NC-Fe incorporation.

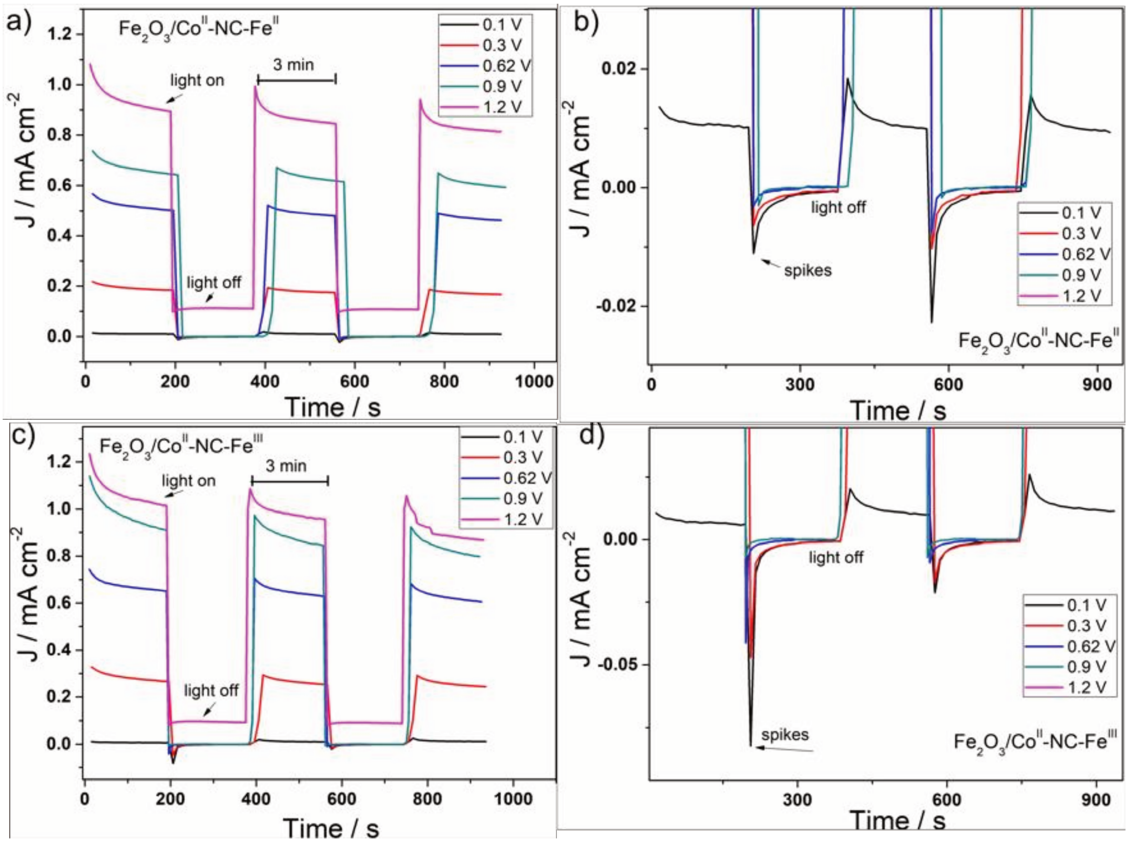


Figure 3.8: *J x V* curves before and after long-term stability of a) α-Fe_2O_3/Co^{II}-NC-Fe^{II} and its (b-c) chopped-light chronoamperometry measurements at different applied potentials (0.1 - 1.2 $V_{Ag/AgCl}$); the same measurements carried out for (d-f) α-Fe_2O_3/Co^{II}-NC-Fe^{III} photoanode. Figures c and f represent the magnification of figures b and e, respectively, and show the spikes associated with charge carriers recombination at pH 7.

The charge carrier dynamics on α-Fe_2O_3 and α-Fe_2O_3/Co-NC-Fe photoanodes, were evaluated by TAS experiments. The transient absorption was probed at 650 nm within µs-s scale without and with the application of an external electrical bias of 0.62 V vs Ag/AgCl (corresponded to 1.23 V vs RHE), as shown in Figure 3.9. The fast decay of holes lifetime on early time scale is well-known in the literature,[92,159] observed in Figure 3.9a. The decay kinetics after Co-NC-Fe modification are shown in Figures 3.9b and c. It is worth mentioning that Co-NC-Fe did not affect the probing of holes at this wavelength. The first observation is the effect of applied bias on the increased signal amplitude for all electrodes, in which much longer lifetime of the photogenerated holes is observed upon Co-NC-Fe modification on α-Fe_2O_3 surface. Moreover, it is noticed a slower power-law decay upon Co-NC-Fe modification, more pronounced for α-Fe_2O_3/Co^{II}-NC-Fe^{III}, corroborating with the best PEC performance

among the samples. The results suggest that ultrafast electron/hole recombination is retarded, leading to the formation of longer lived holes. Interestingly, taking the signal amplitude at 1 ms as reference, the signal of photogenerated holes in pristine α-Fe_2O_3 reaches zero, in contrast to that of the modified α-Fe_2O_3 photoanodes, even for unbiased measurements. Additionally, the signal amplitude of photogenerated holes in α-Fe_2O_3/Co-NC-Fe photoanode is increased by almost 20-fold (Figure 3.9d) compared to that of pristine Fe_2O_3 photoanode followed by a slower decay profile, indicating more effective charge separation.

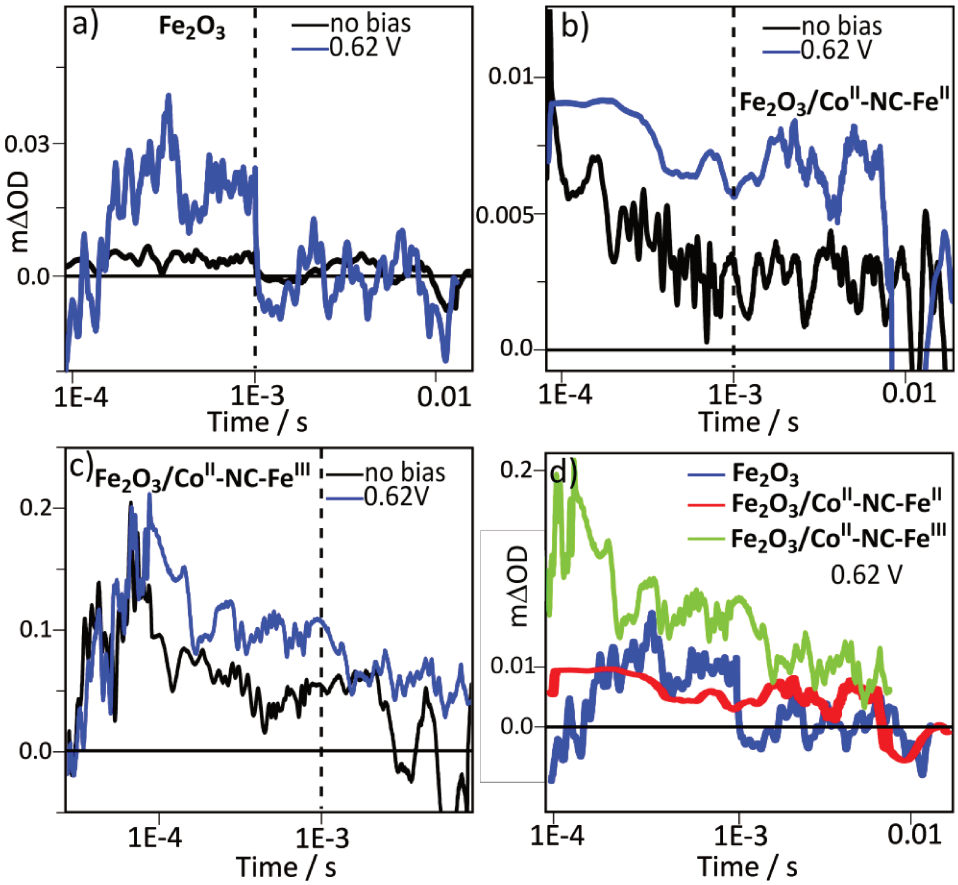


Figure 3.9: Dynamics of photogenerated holes (probed at 650 nm) in a) α-Fe_2O_3, b) α-Fe_2O_3/Co^{II}-NC-Fe^{II} and c) α-Fe_2O_3/Co^{II}-NC-Fe^{III} photoanodes; d) transient absorption decay of the materials at 0.62 $V_{Ag/AgCl}$ (1.23 V_{RHE}). The measurements were carried out in the absence or under 0.62 $V_{Ag/AgCl}$ of applied bias in 0.1 M KPi (pH 7).

IPCE spectra of the electrodes are shown in Appendix B, Figure B4. It is observed an appreciable improvement in the IPCE intensity upon α-Fe_2O_3 modification with Co-NC-Fe. Correlating with PEC performances, it is observed that despite α-Fe_2O_3-Co-NC-Fe^{II} photoanode presents lower photocurrent density in $J\ x\ V$ curves,

its IPCE profile is more intense when compared to α-Fe_2O_3/Co^{II}-NC-Fe^{III} photoanode. This behavior may be associated with the absorption of α-Fe_2O_3-Co-NC-Fe^{II} film in the UV region, as observed in Figure 3.5b. IPCE plots were obtained at a given applied potential (in this case a constant potential of 0.62 V vs Ag/AgCl), and their values are only obtained after the photocurrent stabilization. The α-Fe_2O_3/Co^{II}-NC-Fe^{II} photoanode was observed to be more stable than α-Fe_2O_3/Co^{II}-NC-Fe^{III} in this experiment.

Up to this point, one can see a substantial enhancement of PEC performance of α-Fe_2O_3/Co-NC-Fe in comparison to bare α-Fe_2O_3 photoanodes and an increased lifetime of the photogenerated charge carriers. Nonetheless, the main reason for the boosted photocurrent has not yet been fully elucidated. Likewise, it was perceptible that despite better PEC performance observed for both α-Fe_2O_3/Co-NC-Fe photoanodes, α-Fe_2O_3/Co^{II}-NC-Fe^{III} was found to have stronger influence on photocurrent density generation at higher potentials, whereas α-Fe_2O_3/Co^{II}-NC-Fe^{II} achieved a plateau photocurrent density. In order to understand these observations in terms of potential induced chemical changes, we performed *in situ* UV-vis (in the dark) and FTIR studies (in the dark and under light illumination).

CV measurements of Co-NC-Fe (Figures 3.10a and b) and of α-Fe_2O_3/Co-NC-Fe modified photoanodes (Figures 3.10c and d) were carried out to determine the redox processes that take place under applied bias. Here, pristine Co^{II}-NC-Fe^{II} and Co^{II}-NC-Fe^{III} photoanodes (deposited onto FTO substrates) show two oxidation processes in 0.1 M KPi, both under dark and light illumination conditions, with cathodic peaks observed at 0.85 and 0.4 V, assigned to Co^{II}/Co^{III} and Fe^{II}/Fe^{III} redox pairs.[172] These features were intensified by irradiation, as well as by potential cycling, especially for Co^{II}-NC-Fe^{III} electrode. Interestingly, there is a high effect of light illumination on the redox process in Co^{II}-NC-Fe^{III} at 1.0 $V_{Ag/AgCl}$ from the first to the tenth cycles. The results here, when compared to LSV measurements, suggest that when Co-NC-Fe are incorporated on α-Fe_2O_3 photoanodes certain oxidation processes in Co-CN-Fe are favoured to occur.[216] CV measurements of Fee$_2O_3$/Co^{II}-NC-Fe^{III} photoanode in (Figure 3.10d) also show the occurrence of the oxidation process close to 0.2 $V_{Ag/AgCl}$ under light illumination, which cannot be seen for bare Co-NC-Fe electrode and much higher than that for α-Fe_2O_3/Co^{II}-NC-Fe^{II} photoanode (Figure 3.10b).

Although *in-situ* UV-Vis measurements have shown chemical changes associated with redox processes under applied potential in the dark, *in-situ* FTIR experiments

were performed to gain a deeper understanding about possible changes in oxidation between dark and light conditions. Herein, it is expected that *in-situ* FTIR spectroscopy brings additional evidence about the redox processes observed in CV measurements. Co-NC-Fe is potentially attractive for infrared investigations since its structure contains strongly absorbing CN^- functional group.[217] It is important to point out that Co-NC-Fe samples may exist in four different combinations of Co and Fe oxidation states, i.e.,: Co^{II}/Fe^{II}, Co^{III}/Fe^{II}, Co^{II}/Fe^{III} and Co^{III}/Fe^{III}, in which CN^- stretching mode frequencies are seen at different wavenumbers. To the best of our knowledge, this is the first report about *in-situ* FTIR measurements on Fe_2O_3/Co-NC-Fe, even in the dark and under light illumination.

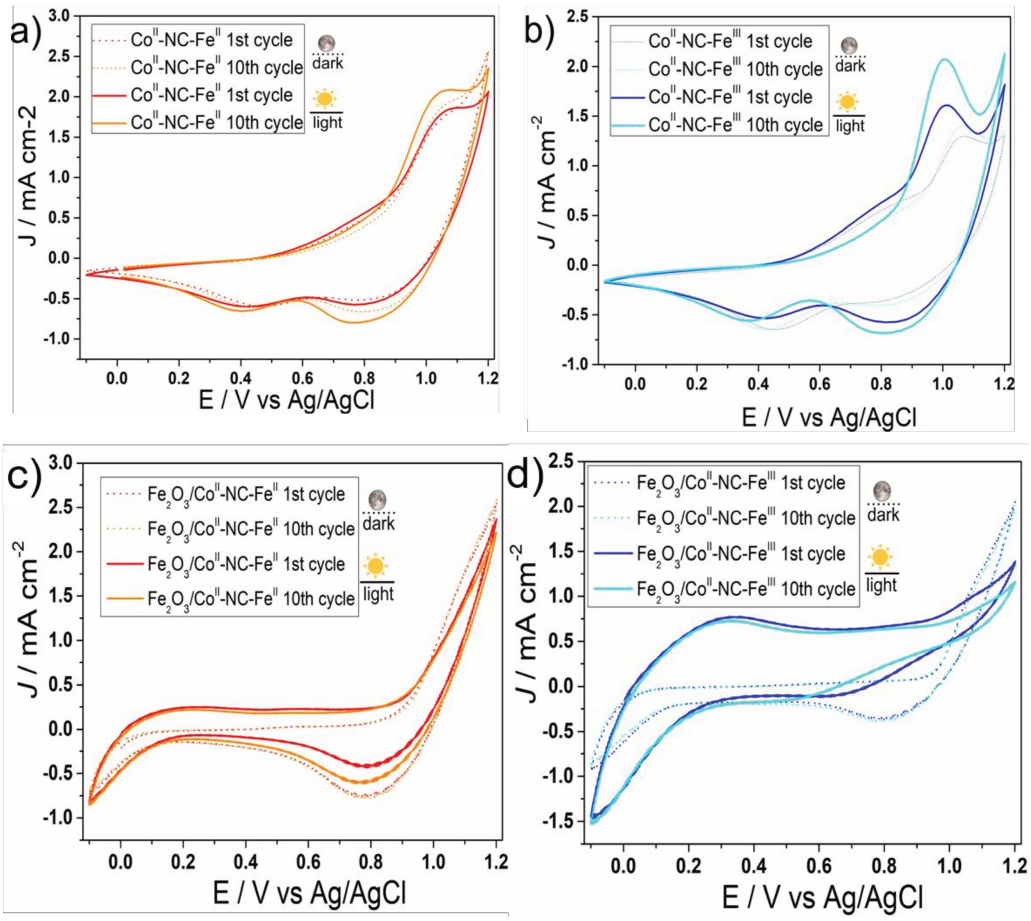


Figure 3.10: Cyclic voltammetry (CV) curves of c) Co^{II}-NC-Fe^{II}, Co^{II}-NC-Fe^{III}, e) α-Fe_2O_3/Co^{II}-NC-Fe^{II} and f) α-Fe_2O_3/Co^{II}-NC-Fe^{III} photoanodes in 0.1 M KPi. All CV curves depict the first (1^{st}) and tenth (10^{th}) cycles.

Prior to FTIR *in-situ* experiments, CV measurements of each material on gold substrates were performed (see in Apendix B – Figures B5a and b) to attain a stationary state. Afterwards, the measurements in the dark of Co^{II}-NC-Fe^{II}, α-Fe_2O_3/Co^{II}-NC-Fe^{II}, Co^{II}-NC-Fe^{III} and α-Fe_2O_3/Co^{II}-NC-Fe^{III} were performed in 0.1 M

KPi media (Figure 3.11), as function of applied bias. Figure 3.11 shows only signals coming from the species formed (negative signals) during the increase of electrochemical potential. The consumed species (seen as positive signals) are shown in the full spectra in Apendix B, Figure B6.

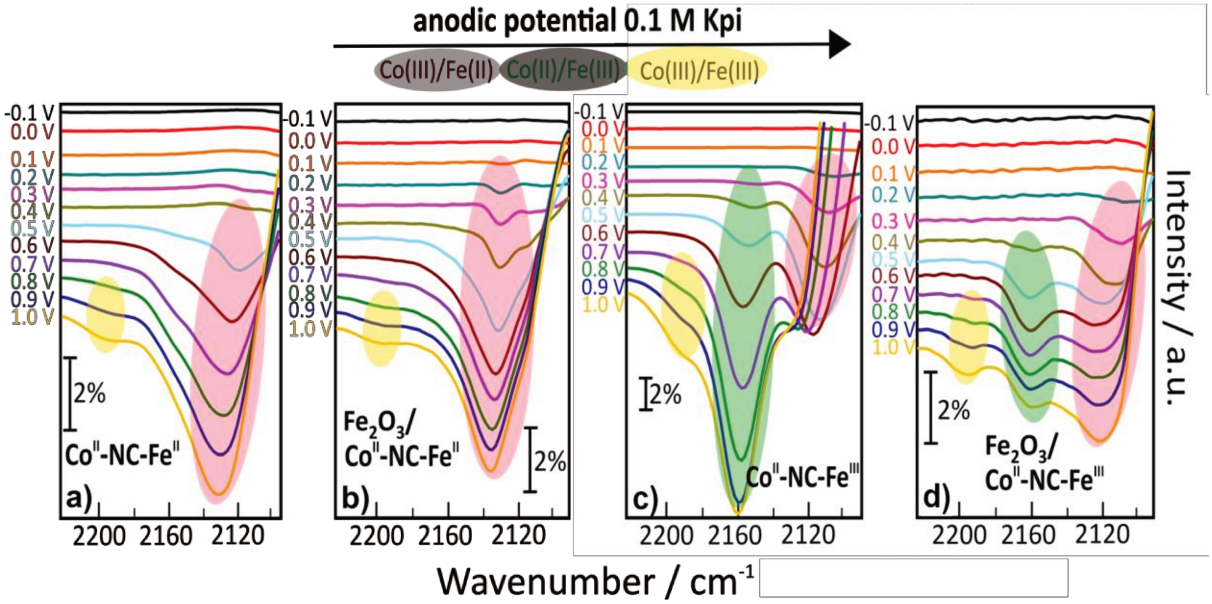


Figure 3.11: *In-situ* FTIR spectra of a) Co^{II}-NC-Fe^{II}, b) α-Fe_2O_3/Co^{II}-NC-Fe^{II}, c) Co^{II}-NC-Fe^{III} and d) α-Fe_2O_3/Co^{II}-NC-Fe^{III} in the dark. The spectra were recorded in the range of -0.1 to 1.0 V vs Ag/AgCl (1 mV s^{-1}) in 0.1 M KPi (pH 7).The circles depict the appearance of the Co^{III}/Fe^{II} (rose), Co^{II}/Fe^{III} (green) and Co^{III}/Fe^{III} (yellow) oxidized species as a function of applied bias.

Bands due to the oxidation of Co^{II} and/or Fe^{II} were observed, in accordance with XPS results. The attribution of the bands was based on the literature[186,187] and in spectra obtained with standards ($K_3Fe(CN)_6$ and $K_4Fe(CN)_6.3H_2O$ precursors) in solutions (Appendix B, Figure B7) and a summary of the band assignments can be found in Table 2. The observed νC≡N modes in the region of ~2125, ~2160 and ~2190 cm^{-1} are assigned to $Co^{III}(ls,t_2g^6e_g^0)$-CN-$Fe^{II}(t_2g^6e_g^0)$, $Co^{II}(hs, t_2g^5e_g^2)$-CN-$Fe^{III}(t_2g^5e_g^0)$ and $Co^{III}(ls,t_2g^6e_g^0)$-CN-$Fe^{III}(t_2g^5e_g^0)$, where hs and ls represents high-spin and low-spin configuration respectively.[210] It is worth mentioning that the strong ligand field of CN^- leads to a low-spin state of cobalt ion rather than a high-spin state, turning $Co^{III}(ls, t_2g^6e_g^0)$ more stable,[209] also favoring the formation of Co^{III}-NC-Fe^{II} species in the as-prepared material.

Table 2: νC≡N stretching mode frequencies[a] of each material. The measurements were carried out in dark conditions.

Sample	Co^{II}/Fe^{II} (cm^{-1})[b]	Co^{III}/Fe^{II}(cm^{-1})	Co^{II}/Fe^{III}(cm^{-1})	Co^{III}/Fe^{III}(cm^{-1})
Co^{II}-NC-Fe^{II}	2082	2132	-	2192
Co^{II}-NC-Fe^{III}	2083	2114	2160	2191
Fe_2O_3/Co^{II}-NC-Fe^{II}	2077	2126	-	2193
Fe_2O_3/Co^{II}-NC-Fe^{III}	2078	2115	2156	2192

[a] The values (cm^{-1}) correspond to the stretching mode frequencies at 0.9 V (maximum signal);[b] the values correspond to the stretching mode frequencies of the reduced species.

Figures 3.11a and b in the dark show that the presence of α-Fe_2O_3 strongly impacts the results for Co^{II}-NC-Fe^{III}. A band around 2115 cm^{-1} arises at 0.1-0.2V due to the stretching of CN-Co^{III}/Fe^{II} configuration, indicating the oxidation of Co^{II} to Co^{III} [176] (CN^- was set in front of the oxidation state of the ions to indicate that we are referring to the stretching mode and not the material). All the bands changed their frequencies with the electrochemical potential, which is due to the well-known Stark effect.[218]

Very interestingly, the band at 2160 cm^{-1} is almost exclusive for Co^{II}-NC-Fe^{III} and α-Fe_2O_3/Co^{II}-CN-Fe^{III}, and can be assigned to the regeneration of Fe^{III} after the application of a positive bias. The full oxidization of Fe^{II} to Fe^{III} is a process limited by the diffusion of K^+ ions, and its kinetics demands two-K^+ extraction from the framework of the Co-NC-Fe structure for the charge balance of the compounds within the lattice[219] (Reaction 2), which may be assumed as the reason for the absence of CN-Co^{II}/Fe^{III} signal at 2160 cm^{-1} under applied bias for Co^{II}-NC-Fe^{II} and α-Fe_2O_3/Co^{II}-CN-Fe^{II}. As observed in Figures 3.11c and d, Co^{II}-NC-Fe^{III} and α-Fe_2O_3/Co^{II}-CN-Fe^{III} presented reversible intercalation kinetics, since both Co and Fe ions can be reduced/oxidized during the application of an external bias. On the other hand, Co^{II}-NC-Fe^{II} and α-Fe_2O_3/Co^{II}-CN-Fe^{II} did not present this feature, as consequence the band at 2160 cm^{-1} was not detected, even at higher potentials.

Finally, a relatively low intensity band emerges at 2190 cm^{-1} due to the formation of either CN-Co^{III}-Fe^{III} or a second type of Co^{II}-NC-Fe^{III} species,[219] which only

appears at higher potentials (≥0.8V) and seems to be more intense for Co^{II}-NC-Fe^{III}. In Figures 3.12a and b under light illumination, despite the bands are the same as in dark, the Co^{III}-NC-Fe^{II} signal appears at lower potentials and is greatly enhanced especially for α-Fe_2O_3/Co^{II}-NC-Fe^{III} (Appendix B – Figure B8) which presented higher intense band signal at 2125 cm^{-1}, indicating the preferential formation of Fe^{II} species. Meanwhile, the signal of Co^{III}/Fe^{III} for α-Fe_2O_3/Co^{II}-NC-Fe^{III} (Figure 3.12b) is also increased at higher potentials, indicating that Fe ions have their both 2+ and 3+ oxidation states formed simultaneously under light illumination with the application of an external bias.

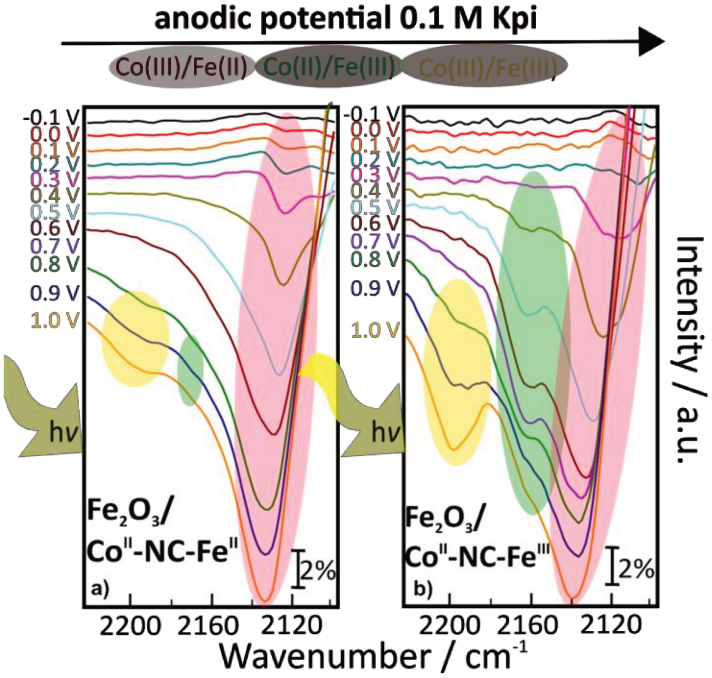


Figure 3.12: *In-situ* FTIR spectra of a) α-Fe_2O_3/Co^{II}-NC-Fe^{II} and b) α-Fe_2O_3/Co^{II}-NC-Fe^{III} under light illumination. The measurements were carried out for materials deposited onto gold substrates.

Returning to the voltammograms in Figures 3.6a and correlating them with the *in-situ* FTIR spectra, we assign the dark current to the oxidation of Fe^{II} to Fe^{III} in the Co-NC-Fe catalyst under applied bias and not to any water oxidation process. *In-situ* FTIR spectra show the oxidation of Fe^{II} to Fe^{III} starting at ~0.4V, region where the dark current starts to increase. *In-situ* FTIR allowed us to follow the oxidation of Co and Fe ions induced by the electrochemical potential in Co-NC-Fe and α-Fe_2O_3/Co-NC-Fe. The results in the dark demonstrate that the first oxidation reaction is the Co^{II}/Co^{III} redox specie at lower potentials (0.1-0.2 $V_{Ag/AgCl}$), and then Fe^{II}/Fe^{III} ions (0.4 $V_{Ag/AgCl}$), in which the latter is observed exclusively for Co^{II}-NC-Fe^{III}-based

photoanodes. Considering the strong synergistic effect of the light and α-Fe_2O_3/Co^{II}-NC-Fe^{III} photoanode, these experiments clearly suggest that the formation of the Co^{III}/Fe^{II} pair is crucial towards an optimal PEC performance.

In the results obtained by *in-situ* FTIR experiments, the most noticeable feature is that the formation of Co^{II}/Fe^{III} specie (at 2160 cm^{-1}) is observed only for Co^{II}-NC-Fe^{III} with and without α-Fe_2O_3. The use of $[Fe(CN)_6]^{3-}$/$[Fe(CN)_6]^{4-}$ as redox mediator[220] in Z-scheme applications under neutral condition has been studied and shows excellent activity for water oxidation using Fe^{III} as electron acceptor. Yamamoto and co-workers[221] have shown that upon band gap excitation of titania nanosheets, Prussian blue (Fe^{III}-CN-Fe^{II}) can be photoreduced to Prussian white (Fe^{II}-CN-Fe^{II}) by receiving electrons from titania nanosheets. Figure 3.13 shows the schematic illustration of α-Fe_2O_3/Co-NC-Fe phoanode during PEC characterization. As illustrated in the scheme in Figure 3.13, when α-Fe_2O_3/Co-NC-Fe photoanode is photoexcited, electron/hole pairs are created. The electrons are transferred along α-Fe_2O_3 nanorods towards FTO substrate and then to the counter electrode (Pt wire) to drive proton reduction (H^+/H_2) – (reaction 1 in Figure 3.13), whereas holes are accumulated at the photoanode/electrolyte interface to drive water oxidation (H_2O/O_2 – reaction 2 in Figure 3.13), as expected for an n-type semiconductor.

As observed in Figure 3.13, even the CB position of α-Fe_2O_3[17,222] is below that of proton reduction, it is still above Fe(t_{2g}) of Co-NC-Fe.[220] We propose the third reaction (reaction 3 in Figure 3.13) associated with the photoreduction of Co^{II}-NC-Fe^{III} by the electron transfer from CB of α-Fe_2O_3 to $[Fe(CN)_6]^{3-}$ species in Co-NC-Fe. This reaction is proposed in the situation where the photogenerated electrons, while migrating along the nanorod boundary of α-Fe_2O_3 find a Co^{II}-NC-Fe^{III} specie before reaching the FTO substrate and then taking part of Fe^{III} reduction. Such mechanism is supported by *in-situ* FTIR experiments where under light illumination, Co^{III}-NC-Fe^{II} species have their signal intensified, indicating the photoreduction of Fe^{III} ions by the electrons in the CB of α-Fe_2O_3 at higher potentials. Correlating these data with TAS measurements, holes at VB of α-Fe_2O_3 have their lifetime prolonged, suppressing electron/hole recombination and consequently enhancing the photocurrent density at high potentials. The collection of these electrons at the boundaries of the nanorods (Figure 3.13 - left) led holes to accumulate at the surface remaining available to oxidize water. This would not be expected if Co-NC-Fe particles are in contact with α-Fe_2O_3 nanorods only at the electrode surface.

Such observations can also be supported by the FEG-SEM imagens, with the presence of Co-NC-Fe catalyst not only at the top of the film but also inside and between the α-Fe_2O_3 nanorods. This suggests that α-Fe_2O_3 nanorods are in close contact with Co-NC-Fe particles at the boundaries. Hence, the generated electrons can be captured by the Co^{II}-NC-Fe^{III} particles inside the film, reducing Fe^{III} to Fe^{II}. Meanwhile, Fe^{III} regeneration may be achieved by the application of an external bias, as observed in the increase of 2190 cm^{-1} signal under light illumination (E = 1.0 V, Figure 3.12b), suggesting the backward reaction forming $[Fe(CN)_6]^{3-}$.

In contrast, *in-situ* FTIR spectra did not show a significant evidence of Fe^{II} oxidation in Co^{II}-NC-Fe^{II} as well as α-Fe_2O_3/Co^{II}-NC-Fe^{II}. Another evidence for the resistance towards oxidation of Fe^{II} to Fe^{III} in Co^{II}-NC-Fe^{II} is the CV curves in Figure B5 (Appendix B) where smaller capacitive current were observed for α-Fe_2O_3/Co^{II}-NC-Fe^{II} photoanode, compared to the other Co-NC-Fe material. These facts will probably affect the charge carrier recombination rate since electrons from CB of α-Fe_2O_3 cannot be transferred to Fe^{III} species and reduce them. Consequently, electron/hole recombination reaction overwhelms water oxidation. The greater photocurrent density for α-Fe_2O_3/Co^{II}-NC-Fe^{II} compared to bare α-Fe_2O_3 photoanode is probably influenced by modification of surface states turning charge transfer kinetically favorable.[41]

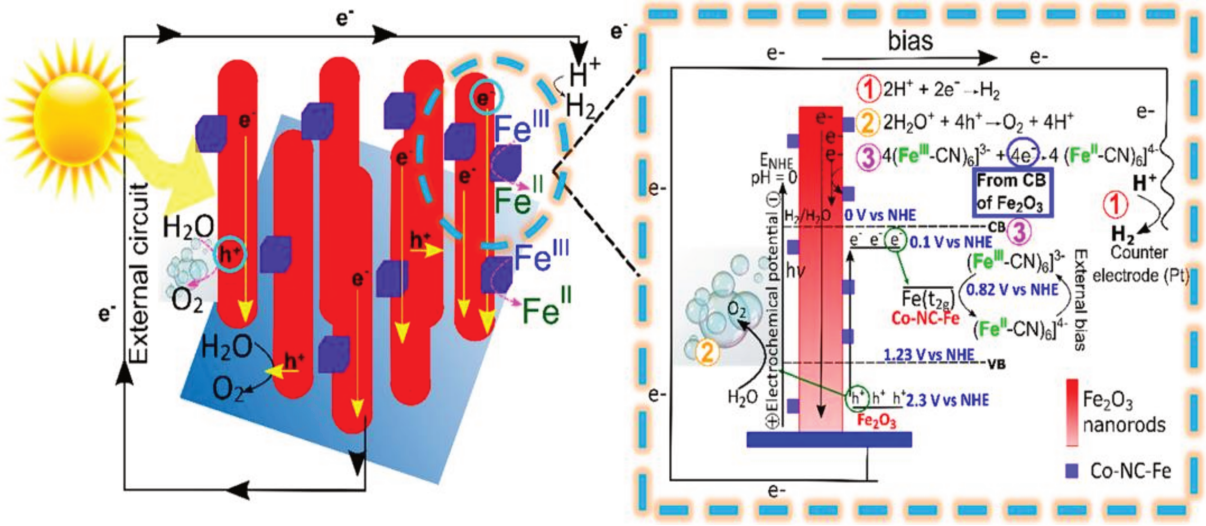


Figure 3.13: Schematic illustration of charge carrier transport in α-Fe_2O_3/Co^{II}-NC-Fe^{III} photoanode and an energy diagram depicting the three proposed reactions during PEC characterization, one of which is the photoinduced electron transfer from the CB of α-Fe_2O_3 to $[Fe(CN)_6]^{3-}$ in Co-NC-Fe. The band edge positions are shown at pH = 0 relative to NHE.[17,221]

Apart from the intrinsic property of the materials, the synergistic effect, and the energy level modification of the surface states in the α-Fe_2O_3 photoanodes suggested by recent works,[41,189] we have shown, based on our recent outcomes by *in-situ* characterization that the PEC performance of α-Fe_2O_3/Co-NC-Fe photoanodes is also dependent on the difference in the oxidation states of the elements in the Co-NC-Fe structure analogues in their starting materials. In addition, the whole process demands thermodynamic and kinetic properties, and the efficiency of the PEC performance is fundamentally governed by the morphology, defect sites, photoactive area of the electrode and stoichiometric ratio which in fact affect the capability of the surface to avoid electron trapping or recombination by photogenerated holes.[223]

In this work, the incorporation of Co-NC-Fe has proven to greatly impact such properties towards the achievement of better PEC performance. *In-situ* FTIR shows the oxidation of Co^{II} to Co^{III} in both photoanodes, however, solar light enhances the generation of reversible Fe^{II}/Fe^{III} redox pairs, supporting the process proposed in Figure 3.13, which could be the main cause for the electron/hole pair lifetime enhancement measured by TAS. Due to intrinsic drawbacks of α-Fe_2O_3 that hamper its use as an effective photoanode, the Co-NC-Fe incorporation showed a promising potential for other semiconductors and for the development of electrocatalysts for PEC water splitting, especially under mild and neutral conditions.

3.4 Partial conclusion

In this section, it was observed a substantial improvement in photocurrent density of α-Fe_2O_3/Co-NC-Fe photoanode compared to bare α-Fe_2O_3. Given the complexity of chemical changes that take place in α-Fe_2O_3/Co-NC-Fe photoanodes, we showed the fundamental understanding of different mechanisms with the contribution of *in-situ* techniques for materials characterization. Despite both Co-NC-Fe materials led to higher PEC performance, Co^{II}-NC-Fe^{III} showed stronger influence on photocurrent generation. In summary, owing to synergistic effect between α-Fe_2O_3 and Co-NC-Fe particles, the resulting α-Fe_2O_3/Co^{II}-NC-Fe^{III} photoanode exhibited better PEC performance compared to the α-Fe_2O_3/Co^{II}-NC-Fe^{II} photoanode.

The difference between their PEC performances was understood that besides the modified surface state in both photoanodes, in the former, the reversibility of Fe^{II}/Fe^{III} redox process was indispensable to boost photocurrent density generation. In this work, we showed the vital importance of understanding the mechanisms underlying charge separation and transport, for the materials development of better photoanodes. Further

efforts have to be made to synthesize stable (α-Fe_2O_3/Co-NC-Fe)-based materials as a viable approach with appropriate band-edge alignments for oxygen evolution experiments without the need of applied bias and under mild conditions.

Chapter 4

SnO_2 as thin conformal layer over $BiVO_4$ surface for enhanced charge carrier separation towards O_2 evolution

In this third and final chapter, it will be discussed a general introduction of the fundamental aspects of PC (suspended photocatalysts) water splitting. Bismuth vanadate ($BiVO_4$) photocatalysts has their surface modified by SnO_2 particles, acting a conformal layer coating to prevent charge recombination and improve stability. A investigation with surface photovoltage spectroscopy (SPS) technique will be explored to get information about the photochemical charge generation, separation and transport at interfaces. This technique is a powerful tool to probe contact potential difference changes ($\triangle$CPD) on photocatalysts upon illumination. The findings shed light on the importance of protecting the surface of semiconductors against charge recombination and may be useful for developing efficient photocatalysts for oxygen evolution reaction. This work was performed during the PhD internship at the University of California (UC-Davis) in 2017 under the supervision of Prof. Frank. E. Osterloh.

4.1 Introduction

Recently, bismuth vanadate ($BiVO_4$) has been attracted substantial attention for photocatalytic applications owing to its many advantages as semiconductor to drive water oxidation.[21] Despite possessing promising characteristics to be applied in photocatalysis, the fast electron-hole pairs recombination is still one of the biggest drawbacks involving this semiconductor. The use of conformal layers in order to minimize such limitation and to improve charge separation is the aim of this chapter. Herein, it will be reported on the use of SnO_2 as a conformal coating layer over the $BiVO_4$ surface for O_2 evolution reaction. The incorporation of SnO_2 over the $BiVO_4$ surface showed the beneficial effect in O_2 evolution compared to the pristine material, resulting in 490 µmol after 6h of irradiation. Transient absorption and surface photovoltage spectroscopies indicate enhanced charge carrier separation and transport by passivating $BiVO_4$ with SnO_2 thin layer. Even though the O_2 evolution tests were carried out without the presence of a cocatalyst, the use of a thin conformal coating of SnO_2 over $BiVO_4$ showed promising results for further studies.

4.1.1 Bismuth Vanadate ($BiVO_4$)

Over the recent years, there has been a considerable emphasis on ternary metal oxides (TMO) as photoelectrode materials for water splitting,[224] and the amount of possible TMO as photoelectrodes is vast. TMO semiconductors offer a variety of appropriate band gaps (~ 1.6 – 2.3 eV) and modest band edge positions certainly achieve high PEC activity with theoretically 10% of STH efficiency. Generally, the VB of most TMO nanomaterials is composed of a hybridization of O 2p orbital with a d^0 or d^{10} orbitals of one metal cation and the CB is composed by the other metal cation. However, since there is a hybridization of the O 2p with the metal cation in the VB, the resulted VB is pushed upward and thus, the band gap of these semiconductors is usually decreased slightly compared to binary metal oxides.[225]

Sheelite monoclinic bismuth vanadate ($BiVO_4$) has emerged as a promising n-type candidate for water oxidation, since this material presents the ability to absorb visible light (bandgap of ~2.4 eV), relative stability in near-neutral aqueous electrolytes, is non-toxic and earth abundant.[21,226–228] Due to its moderate band gap, $BiVO_4$ can absorb ~11% of solar light and achieve a theoretical maximum AM1.5G photocurrent of 7.6 mA cm^{-2}, resulting in a STH efficiency of 9.3%.

The electronic structure of monoclinic scheelite-type $BiVO_4$ presents higher photocatalytic activity compared to zircon-type $BiVO_4$ due to its band gap value of 2.4 eV which permits to absorb higher amount of visible light compared to zircon-type $BiVO_4$ (2.9 eV) and also due to the difference of electronic states between these two phases, as predicted by DFT (density-functional theory) calculations,[229] as demonstrated in Figure 4.1.

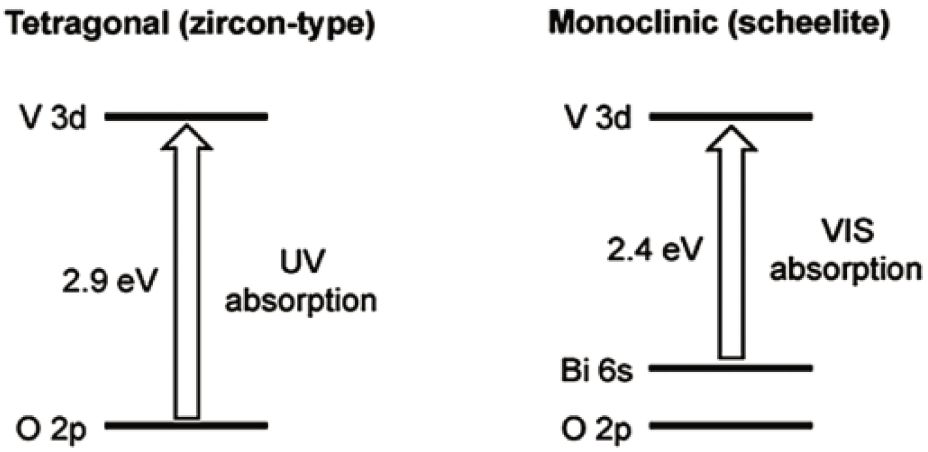


Figure 4.1: Bands structure of tetragonal zircon-type $BiVO_4$ and monoclinic scheelite $BiVO_4$.[230]

For zircon-type $BiVO_4$, the band gap transition is due to charger transfer from O 2p orbitals to empty V 3d (Figure 4.1a). In contrast, the smaller band gap of monoclinic scheelite $BiVO_4$ is due to the 6s state position of Bi^{3+}, which is above the O 2p and the transition from Bi 6s (or hybrid Bi $6s^2$-O 2p) to the V 3d becomes possible (Figure 4.1b).[229] In this case, the VB of monoclinic scheelite $BiVO_4$[230] is composed by the hybridization of O 2p with Bi 6s orbitals,[224,229] through the Bi-O bond.

Although, its CB edge position is just below the water reduction potential, preventing the generation of H_2, unless an external bias is applied.[231] The poor performance for unmodified $BiVO_4$ is limited by electron-hole recombination, slow carrier transport and slow water oxidation kinetics.[232,233] In addition, unmodified $BiVO_4$ typically achieves photocurrent density of ~1 mA cm^{-2} at 1.23 V vs RHE, which is far from the theoretical maximum. Among some drawbacks, one can include: a) relatively short hole diffusion length (~70-100nm)[234], ii) low absorption coefficient of light, iii) poor electrical conductivity,[235] iv) sluggish water oxidation kinetics[236] and v) chemical instability in strongly acidic and/or basic conditions.[237] In consequence, extensive works have been paid in overcoming these shortcomings.

Charge separation plays a key role in determining the potential of conventional semiconductors for photocatalytic applications.[238,239] Several modifications have been proposed to conquer this problem and enhance the photoactivity of $BiVO_4$, including morphology modification,[240,241] thermal annealing in oxygen-deficient condition,[101] crystal-facet engineering,[242] doping,[243–246] loading of the oxygen-evolution-reaction (OER) catalyst[247,248] and crystallographic orientation control.[249]

4.1.2 Charge carrier dynamics on $BiVO_4$

Previous studies of transient absorption in $BiVO_4$ photoelectrodes have reported that several competing processes affect the decay dynamics of photogenerated holes: bi-molecular recombination that takes place from µs to ms, assigned to trapping-detrapping processes,[250] ii) back electron hole recombination (BER), which takes place from ms to s, similar to time scale of water oxidation (~ 100 ms to 1 s)[251] and occurs when phogenerated electrons re-enter the material and recombine with holes, and iii) the reaction of holes with water molecules.[236] Charge carrier recombination in unmodified $BiVO_4$ on ms-s time scales has been assigned to back electron/hole recombination. This slow recombination kinetically competes with water oxidation, limiting the photoanode efficiency.[236]

4.1.3 Conformal layer coatings

The passivation of trapping states, which are commonly attributed as the cause of the need of large overpotential in $BiVO_4$, appears to be a promising strategy to overcome the deleteriours surface recombination and defects by the using of conformal overlayers. Surface passivation layers[251] can enhance the charger transfer in the photoelectrode by supressing surface state density, protecting its surface from chemical photocorrosion and thus, significantly enhancing overall PEC water splitting performance.[44] Passivation layers can be very thin (typically <100 nm), thus preventing parasitic light absorption and can be readily incorporated onto high surface area of high aspect ratio nanostructures.[252] Conformal deposition layer of Al_2O_3,[253] SnO_2,[254] FeOOH,[255] TiO_2[158] over α-Fe_2O_3 photoanodes already showed substantial improvement in charge-separation and charge-transfer processes across semiconductor-liquid interfaces and consequently increased photocurrent. The incorporation of such overlayers can decrease the overpotential required to photo-oxizide water (Figure 4.2a). Figure 4.2b shows the surface defect states in the band structure, leading to high charge recombination. By using an OER catalyst (Figure 4.2c) or a thin noncatalytic surface

layer, defect states are passivated, supressing surface recombination and improving water oxidation.[44]

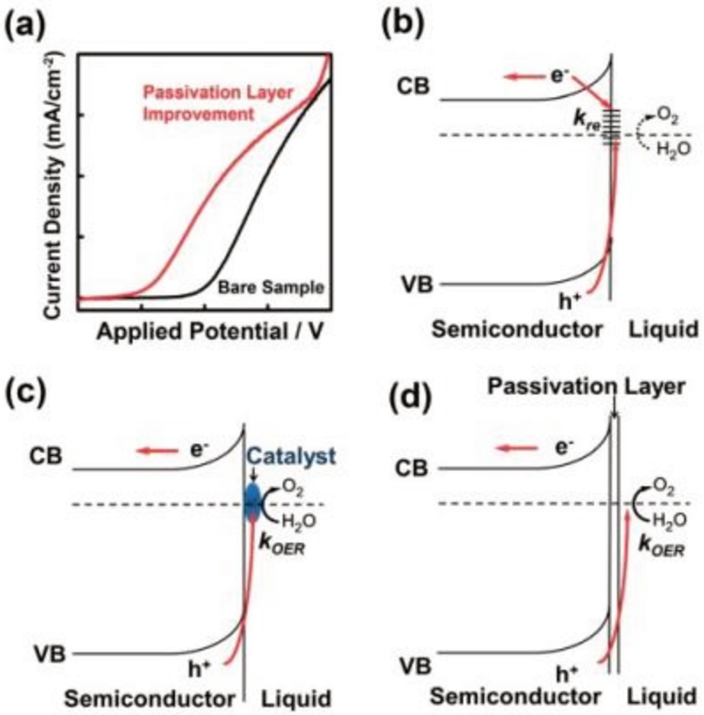


Figure 4.2: a) *J-V* curves of an photoanode before and after surface passivation, b) surface defect states in the band structure, facilitating charge recombination, c) deposition of an OER catalyst layer, promoting facile hole transfer and d) deposition of a very thin noncatalytic surface layer to passivate surface states, supressing charge carrier recombination at the surface for improving water oxidation.[44]

Figure 4.3a and b shows the ultrathin layer of FeOOH deposited by precipitation method over α-Fe_2O_3 nanostructure and the improvement in photocurrent with applied potential (0.612 → 1.21 mA cm^{-2} at 1.23 V_{RHE}), which was attributed to the improved water oxidation kinectics and the passivation of the surface states of the Fe_2O_3. HRTEM images show the highly conformal coating of α-Fe_2O_3 by amorphous FeOOH layers, which act as a cocatalyst to suppress the surface electron-hole recombination. The authors also mentioned that both higher photocurrent and onset potential shift to cathodic region (Figure 4.3c) for FeOOH/α-Fe_2O_3 originate from the improved surface charge separation efficiency.[253]

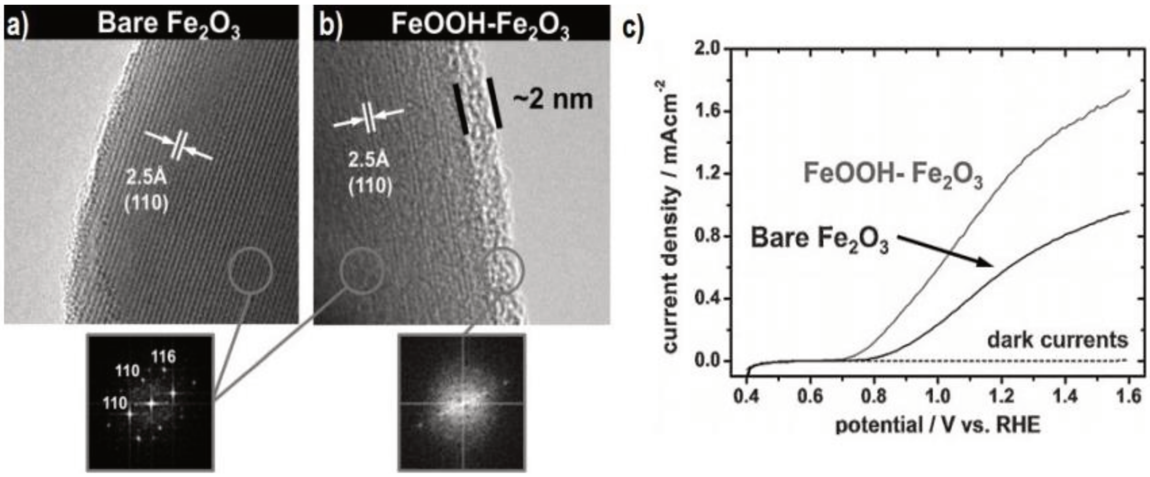


Figure 4.3: HRTEM images of a) the bare α-Fe_2O_3 and b) FeOOH/α-Fe_2O_3 thin films. The thickness of the amorphous FeOOH layer is about 2 nm; c) current density-potential curves recorded at pH 13.6 under 1 sun simulated solar light irradiation.[253]

In addition to the above-mentioned strategies, an interesting and promising way is the surface coating of a thin and homogenous conformal layer over the photocatalyst surface to decrease the recombination rates of charge carriers,[251,256,257] as well as protecting photocatalysts against photocorrosion.[44] Krol et al.[258] showed that the insertion of SnO_2 interfacial layer (~10nm) between FTO and $BiVO_4$ could address the charge collection problem by avoiding recombination at defect states at FTO/$BiVO_4$ interface, acting as a hole mirror. Therefore, the use of conformal coatings on this metal oxide is a promising approach to avoid recombination processes, usually assigned as the main problem in using $BiVO_4$ for photocatalytic reactions.[259]

The use of $BiVO_4$/SnO_2 systems for enhanced PEC performance toward water splitting have been already described on the literature.[258,260–264] However, there is still a lack of detailed works introducing this composite for O_2 evolution experiments as well as a study on the lifetime of the photogenerated charge carriers. Herein, it will be described the deposition of a thin SnO_2 conformal layer over the $BiVO_4$ surface in order to prevent charge recombination to improve its performance for O_2 evolution. TAS measurements have shown higher signal for photogenerated holes, indicating the beneficial effect of passivating $BiVO_4$ surface with SnO_2 in decreasing charge recombination, even without the aid of a cocatalyst. With SPS technique, it was possible to attribute the stronger photovoltage signals for $BiVO_4$@SnO_2 photocatalysts compared to unmodified $BiVO_4$, to better electrons injection into the FTO substrate, enhancing charge separation. This led to higher activity for O_2 gas evolved under visible light illumination during water oxidation experiments.

Objectives

The main goal of this final part of the thesis is to develop a good method to synthesize $BiVO_4$-based suspended photocatalysts on microscale with their surface passivated by SnO_2 as a thin conformal coating and study the enhancement of their photocatalytic activities toward OER using the advanced TAS and SPS techniques.

4.2 Experimental Section

4.2.1 Synthesis of $BiVO_4$ and $BiVO_4$@SnO_2 particles

In a typical procedure,[242] for the synthesis of $BiVO_4$ particles, NH_4VO_3 (36 mmol) and $Bi(NO_3)_3 \cdot 5H_2O$ (36 mmol) were dissolved in 300 mL of 2.0 M nitric acid solution, and the pH value of the solution was then adjusted to 2.0 with the addition of 0.5 M NH_4OH aqueous solution under stirring until the formation of a yellow precipitate. After about 2 h of aging, the precipitate was transferred into a Teflon-lined stainless steel autoclave with a capacity of 30 mL and hydrothermally treated at 200 °C for 24 h. SnO_2 nanoparticles were prepared using the hydrothermal method,[265] in which 300 mg of $SnCl_4.2H_2O$ was dissolved in 30 mL of 2-propanol and distilled water solution with a ratio of 4:1. The solution was adjusted to pH 12 by the addition of 0.5 M NaOH solution, and then transferred into a stainless autoclave, and heated at 150 °C for 24 h. The reaction was cooled down at room temperature and the final powder was filtered and washed with distilled water and ethanol. Afterwards, the SnO_2 material was dried at 60°C and stored for subsequent depositions. The deposition of SnO_2 over $BiVO_4$ particles were carried out by a slow drop of a suspension with different amount of SnO_2 into a flask containing 500 mg of $BiVO_4$ particles in the sonicator, as depicted in Figure 4.4. The weight ratios of SnO_2 to $BiVO_4$ were controlled to be 0.5, 1.0, and 3.0 wt%). The final material was filtered and washed several times to remove any residue. The powder was dried at room temperature.

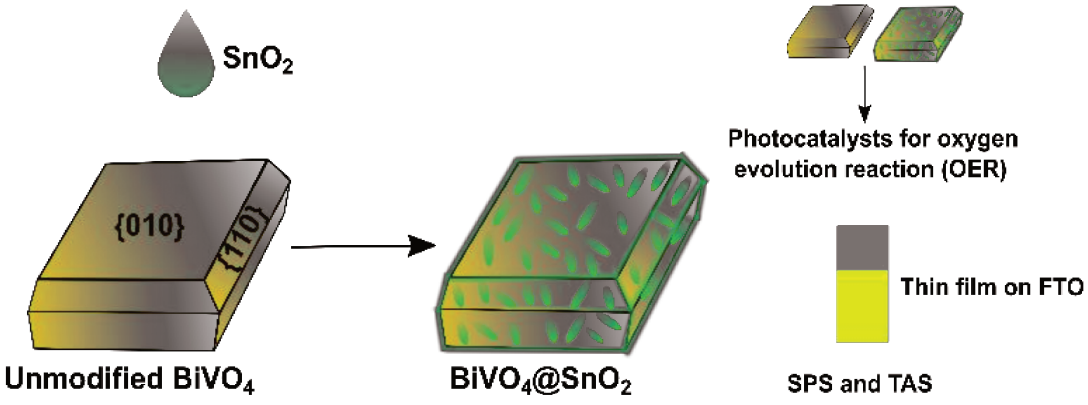


Figure 4.4: Illustration of the monoclinic $BiVO_4$ crystal before and after SnO_2 conformal layer deposition. {010} and {110} depict the dual-facet $BiVO_4$. The powder materials were used for OER and for SPS and TAS measurements as photoanodes on cleaned FTO.

4.2.2 Materials Characterization

X-ray diffraction (XRD) patterns were collected on a Shimadzu model XRD-7000 diffractometer using Cu Kα radiation (0.154 nm) at 40 kV and 30 mA with a rate of 0.01 ° s-1 for 2θ values from 10 to 90°. Ultraviolet/visible diffuse reflectance measurements were carried out in a Thermo Scientific Evolution 220 Spectrometer, using the Kubelka Munk function. The images of the materials were taken using the transmission electron microscopy (TEM) using a Philips CM-120 Biotwin Lens models at an acceleration voltage of 80 kV. For TEM, the samples were prepared by the deposition of a dispersion containing the samples onto a carboncoated copper TEM grid (400 mesh). Scanning electron microscopy (SEM) images were obtained using a Philips XL-30 Scanning Electron Microscopy. For UV-vis and XRD, the measurements were performed using films of the samples. The films were prepared by drop-casting the aqueous suspensions of the materials on fluorine-doped tin oxide (FTO).

4.2.3 O_2 evolution reactions

All photocatalytic oxygen evolution tests were carried out in a closed gas circulation system. For $BiVO_4$ and $BiVO_4$@SnO_2 photocatalysts, 70 mg of powder was dispersed in 100 mL of 0.05 M $AgNO_3$ aqueous solution and the pH was adjusted to 4.5. Prior to irradiation, the dispersion containing the photocatalysts was sonicated in order to disperse the powder with the solvent. The flask was previously evacuated and refilled with Ar four times to remove the dissolved gases. A 300 W Xe lamp was used as the light source with a 420 nm cutoff filter (0.22 M $NaNO_2$). The irradiation system was connected to an SRI 8610C gas chromatograph to quantify the amount of evolved gases.

4.2.4 Photoelectrochemical (PEC) measurements

Prior to PEC measurements, the $BiVO_4$ and $BiVO_4$@SnO_2 photoanodes were deposited by drop-casting 10 mg/mL suspension of $BiVO_4$ or $BiVO_4$@SnO_2 on cleaned FTO. The films were annealed at 450 °C for 60 min. The PEC experiments were carried out under ambient conditions using a potentiostat/galvanostat (μAutolab III). The three-electrode cell configuration was composed of $BiVO_4$, $BiVO_4$@SnO_2 0.5, 1 and 3% photoanodes (1 cm x 1 cm) as the working electrodes (WE), Ag/AgCl in saturated KCl (3 mol L^{-1}) as the reference electrode (RE) and a platinum wire as the counter electrode

(CE). The electrolyte was a solution of 0.5 M Na_2SO_4 in pH 7. The Ag/AgCl electrode potential was converted to RHE by Nernst formula 2.1 (Section 2.2.5.)

4.2.5 Surface Photovoltage Spectroscopy (SPS)

The deposition of $BiVO_4$ and $BiVO_4@SnO_2$ powder by drop casting onto the FTO substrate was carried out for the SPS measurements. The experiments were carried out using the same description in section 2.2.7.

4.2.6 Transient Absorption Spectroscopy (TAS)

TAS measurements at µs-s time scale were acquired by the same setup described in section 2.2.6. The measurements were conducted on $BiVO_4$, $BiVO_4@SnO_2$ 1% and $BiVO_4@SnO_2$ 3% and α-Fe_2O_3/Co-NC-Fe photoanodes in the absence and at 0.62 V vs Ag/AgCl (1.23 V_{RHE}) of applied bias, in 0.1 M KPi (KH_2PO_4/K_2HPO_4) buffer solution.

4.3 Results and Discussion

The monoclinic $BiVO_4$ particles were synthesized by a hydrothermal method described in the experimental session and can be obtained as a yellow powder. The morphology of the unmodified $BiVO_4$ as well as the $BiVO_4$@SnO_2 3% particles was characterized by transmission electron microscopy (TEM), as shown in Figures 4.5a-d. Based on the procedure for the synthesis of the as-prepared $BiVO_4$, it is possible to observe that large crystal size and controllable exposed facets were well obtained (Figures 4.5a and b). The unmodified $BiVO_4$ particles in size of 5 µm present a smooth surface and a regular decahedron shape with well-defined edges.

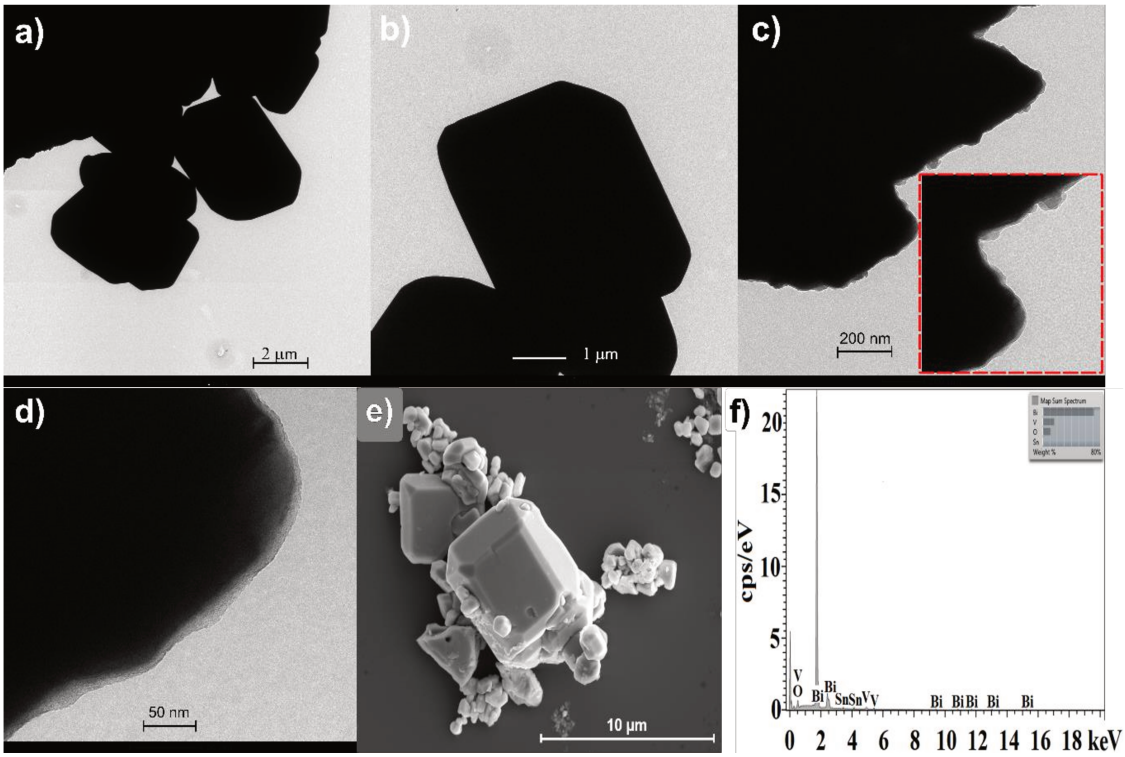


Figure 4.5: TEM images of (a-b) unmodified $BiVO_4$ and (c-d) $BiVO_4$@SnO_2 3% samples. The inset in c) shows the zoomed-in image; e) FEG-SEM image and f) EDX spectrum of $BiVO_4$@SnO_2 3% sample.

The particles present dual-faceted $BiVO_4$, one {010} and the other {110},[242,266] already characterized in the literature. In Figures 4.5c and d, $BiVO_4$@SnO_2 particles structure clearly demonstrate the well coverage of $BiVO_4$ surface after SnO_2 deposition (see also in Appendix C - Figures C1, C2 and C3). The incorporation of SnO_2 created a thin layer around its surface, with thickness in size of ~10 nm, which is desirable for water splitting applications, expected to maintain the light absorption of the semiconductor material. This conformal layer should protect the surface of the

photocatalyst without blocking the UV-light absorption. Whereafter, additional information about the morphology of the particles as well as their chemical composition, were obtained by FEG-SEM combined with EDX element mapping as shown in Figures 4.5e-f.

In Figure 4.5e, the SEM image exhibits similar dodecahedral shape of $BiVO_4$ particles with size of about 5 µm for larger particles (see more in Appendix C - Figure C1). The EDX analysis in Figure 4.5f shows that the $BiVO_4$@SnO_2 sample presents in majority higher amount of bismuth, vanadium and oxygen atoms and a little amount of Sn in the sample, suggesting that the concentration of SnO_2 around the $BiVO_4$ particles is very small, and could only be seen by TEM images, in Figures 4.5c and d. The related element mapping images are presented in Figures C4 and C5 in Appendix C.

The XRD spectra of unmodified $BiVO_4$ and $BiVO_4$@SnO_2 3% were obtained in order to characterize the diffraction peaks of the as-prepared materials. XRD patterns in Figure 4.6a show that the as-prepared $BiVO_4$ deposited films consist entirely of single-phase scheeelite monoclinic structure (JCPDS 14-0688), with good crystallinity. After the coverage of $BiVO_4$ surface with thin conformal layer of SnO_2, the crystalline phases of $BiVO_4$ was preserved, in addition to the appearance of three small peaks at $\theta = 26.5$, 33.8 and 51.7° assigned to the (110), (101) and (211) reflection planes of tetragonal SnO_2 (JCPDS 46-1088), respectively. The optical properties of $BiVO_4$@SnO_2 are displayed in Figure 4.6b. Diffuse reflectance spectra of unmodified $BiVO_4$ and $BiVO_4$@SnO_2 samples plotted with the Kubelka-Munk function. The Kubelka-Munk function reveals that the band gap values of $BiVO_4$ and $BiVO_4$ 1% are similar (2.41 eV), whereas for $BiVO_4$@SnO_2 3% the higher amount of SnO_2 decreased to 2.34 eV. The coverage of $BiVO_4$ surface with a little amount of SnO_2 did not change significantly the light absorption in the visible range, which seems to change only upon increasing the thickness of the SnO_2 conformal layer.

The $BiVO_4$ and $BiVO_4$@SnO_2 (0.5; 1.0 and 3.0% of SnO_2 w/w) photocatalysts were tested in the photocatalytic O_2 evolution reactions, as shown in Figure 4.7. The reactions were conducted under visible light (0.22 M $NaNO_2$ UV filter) in the presence of 0.05 M $AgNO_3$ as a sacrificial agent with 100 mg of suspended photocatalysts. The low activity of unmodified $BiVO_4$ for oxygen evolution in $AgNO_3$ might be due to slow kinetics as well as high charge carrier recombination rate[236] due to accumulation of charge species on {010} and {110} facets on $BiVO_4$.[266] It has been claimed that the relative exposure of these facets may drastically affect charge

recombination.[267] The time courses of gas evolution clearly show the beneficial effect of SnO_2 incorporation on the increase of O_2 production, reaching the amount of 490 µmol from $BiVO_4$@SnO_2 1.0%. By increasing the concentration of SnO_2 to 3.0%, the O_2 evolution decreased significantly. This might be due to the formation of recombination sites of charge carrier through the agglomeration of SnO_2 particles around the $BiVO_4$ particles.

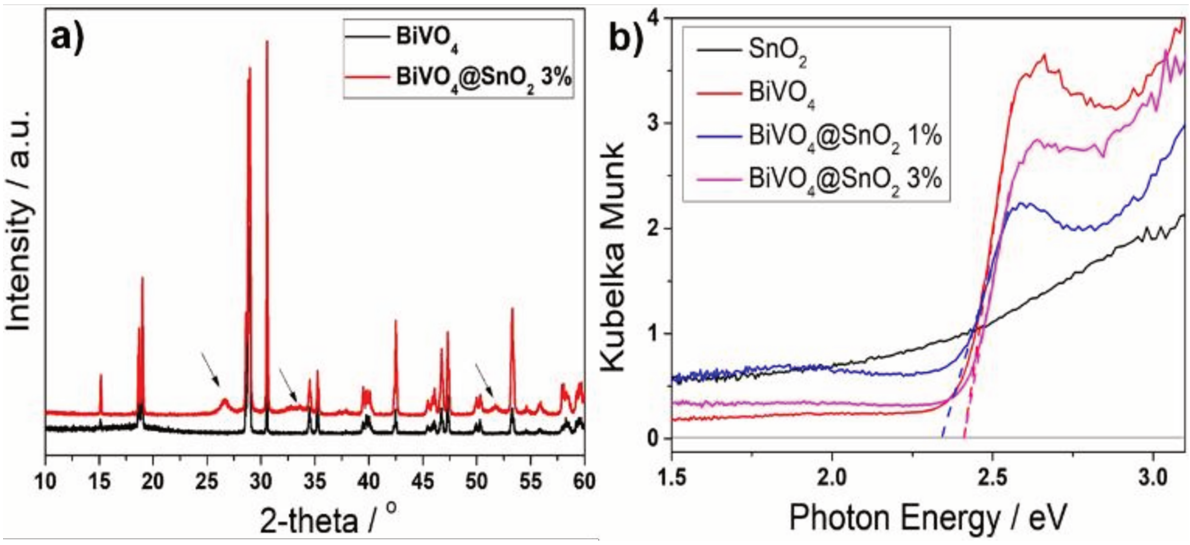


Figure 4.6: a) XRD diffraction peaks and b) Kubelka-Munk converted UV/Vis diffuse reflectance plots of unmodified $BiVO_4$ and $BiVO_4$@SnO_2 samples on FTO substrate.

After 6h of irradiation, the amount of O_2 evolved from $BiVO_4$ particles remained the same. Although $BiVO_4$ semiconductor offers promising advantages in photocatalytic water splitting,[229] its photoactivity is still limited by the high recombination rates of charge carriers.[251] The incorporation of SnO_2 particles over $BiVO_4$ surface increased 7.4 times the oxygen production over time. This improvement can be attributed to the electron transfer from $BiVO_4$ to SnO_2, and consequently, supressing the surface electron-hole recombination.[260] $BiVO_4$@SnO_2 1% wt% presented the highest amount of O_2 evolved after 6h of irradiation, 490 µmol. Despite this value is much higher than that produced by pristine $BiVO_4$ (69 µmol), the photoactivity of this material is limited by electron-hole recombination in the surface, which can be overcome by the incorporation of cocatalysts.[268]

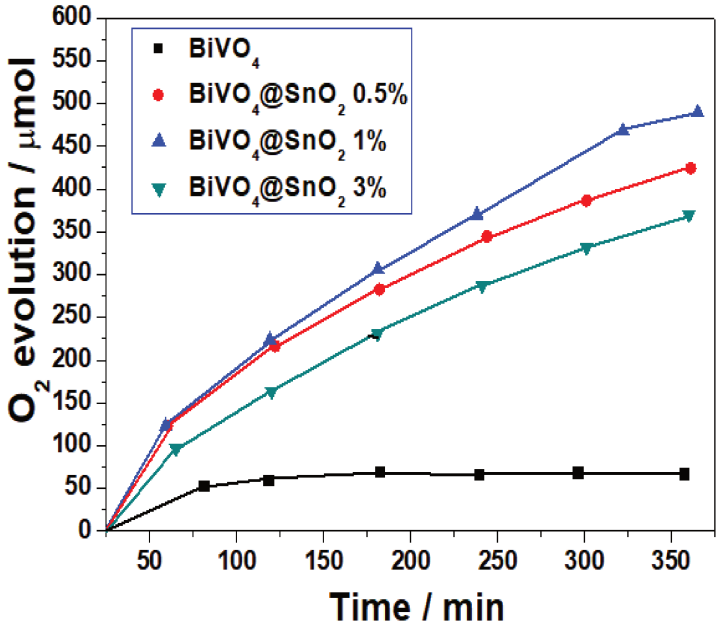


Figure 4.7: Time courses of O_2 evolution over 70 mg of $BiVO_4$ and $BiVO_4$@SnO_2 0.5, 1.0, and 3.0% samples suspended in 100 mL of 0.05 M $AgNO_3$ solution under stirring. The suspension was irradiated with a 300 W Xe arc lamp in the presence of a 0.22 M $NaNO_2$ UV filter ($\lambda > 400$ nm).

The current-potential performance measurements were carried out with the same samples employed in this study. Figure 4.8 shows the chopped linear sweep voltammetry measurements for unmodified $BiVO_4$ and $BiVO_4$@SnO_2 photoanodes in 0.5 M Na_2SO_4 aqueous solution as electrolyte under AM1.5G. All photoanodes show photoanodic behavior for photon-induced O_2 evolution. The photocurrent density in the μA range generated by unmodified $BiVO_4$ photoanodes with large dedecahedron shape is well demonstrated and in agreement with the value reported in the literature.[242] Since the holes difusion length in $BiVO_4$ is ~100 nm,[269] charge recombination are more favorable to take place in large particles.

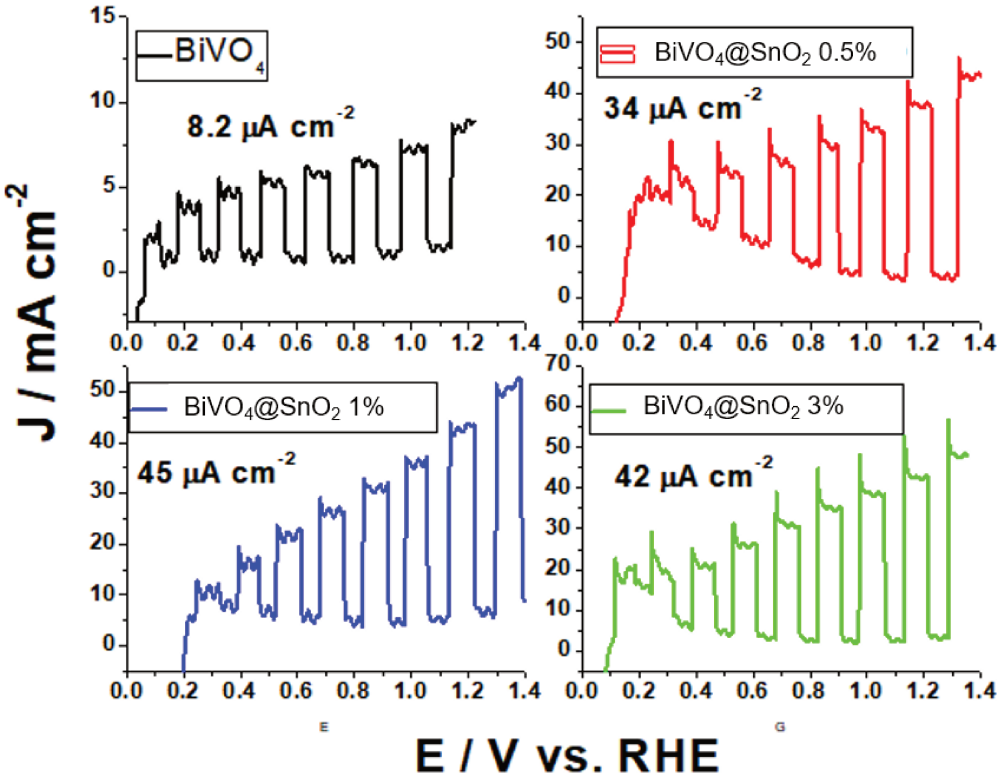


Figure 4.8: Chopped linear sweep photocurrent density vs potential of a) unmodified $BiVO_4$ b) $BiVO_4$@SnO_2 0.5%, c) $BiVO_4$@SnO_2 1% and d) $BiVO_4$@SnO_2 3% photoanodes. The measurements were carried out in 0.1 M KPi electrolyte (pH 7), Scan rate: 10 mVs^{-1}. The illustrated values indicate the photocurrent density obtained at 0.62 V (vs Ag/AgCl) corresponded to 1.23 V (vs RHE).

The chopped-light irradiation upon external bias shows that the incorporation of a thin SnO_2 conformal layer around the $BiVO_4$ particles was able to increase the anodic photocurrent density for all the samples, reaching ~40 µa cm^{-2}. This improvement indicates the better charge carrier separation and transport by the incorporation of SnO_2 particles.[270] Although the photocurrents of the $BiVO_4$@SnO_2 samples are very similar, the difference between them with that of unmodified $BiVO_4$ resulted in 5-fold enhancement, indicating the beneficial coupling between $BiVO_4$ and SnO_2 particles. The results reveal that $BiVO_4$@SnO_2 shows higher potential to be used as a O_2 evolution photocatalyst under visible light, when compared to the unmodified material due to enhanced charge carrier separation and increased O_2 evolution rate.

The following discussion on SPS and TAS measurements address unmodified $BiVO_4$ with the superior and inferior performer of $BiVO_4$@SnO_2 photocatalysts, which are 1 and 3% wt% samples. In order to further characterize the difference between the

photocatalysts properties regarding their intrinsic photochemistry, surface photovoltage spectroscopy (SPS) measurements on $BiVO_4$ and $BiVO_4$@SnO_2 1% and 3% wt% were carried out. Such technique is able to probe the photochemical charge separation on a FTO substrate and also show the effective bandgap of the materials.[271] It worth mentioning that the aliquot used for the material deposition is the same for all films, and therefore the thickness effect is not relevant for the ΔCPD values obainted here. As observed for all materials, the negative signal (Figure 4.9a) reveals the n-type character for $BiVO_4$ semiconductor, meaning that electrons from the CB of $BiVO_4$ are transferred to the FTO substrate. Importantly, the lower effective band gap of $BiVO_4$@SnO_2 3% (~2.4 eV) compared that for $BiVO_4$@SnO_2 1% and unmodified $BiVO_4$ given by the SPS signals, agrees well with the band gap value obtained by the Kubelka-Munk function in 4.6b and the values reported in the literature.[272]

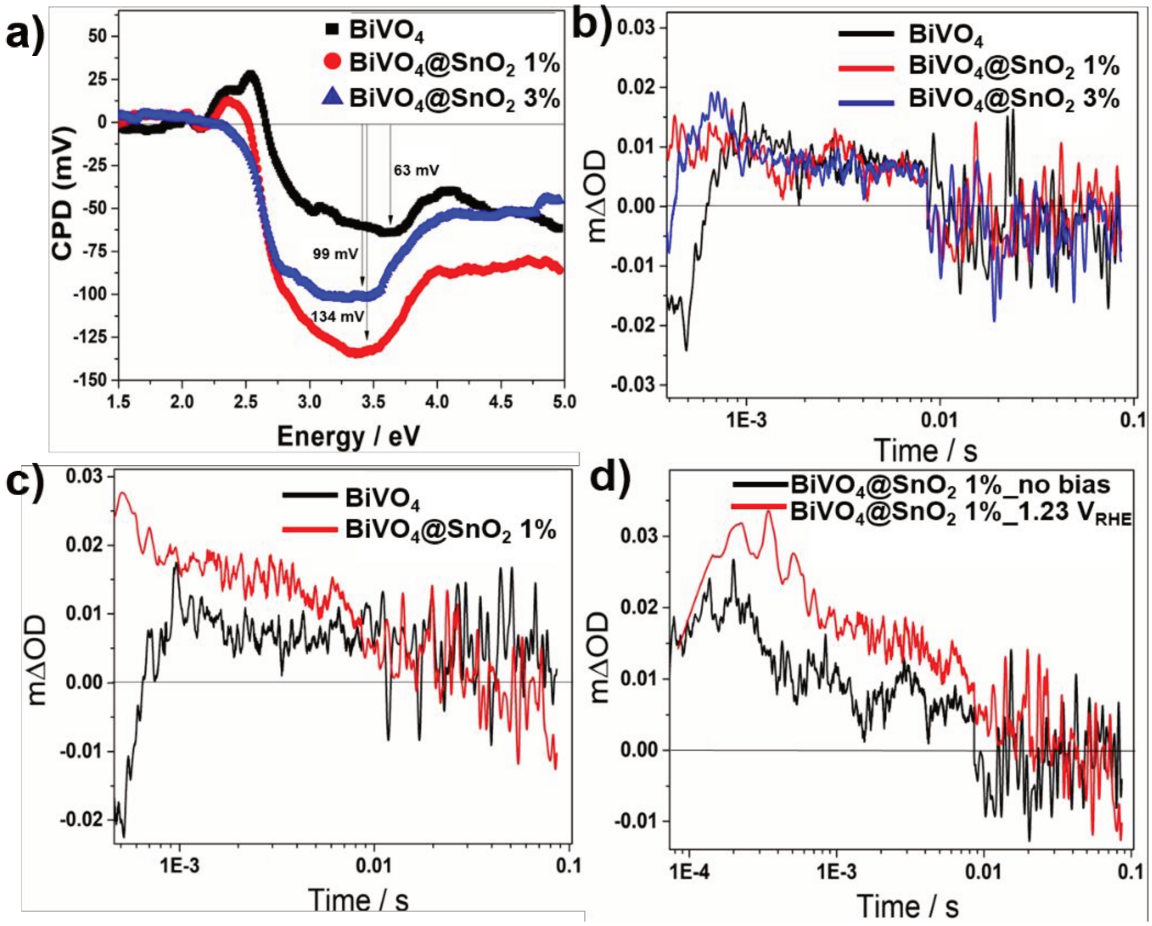


Figure 4.9: a) SPS spectra of unmodified $BiVO_4$, $BiVO_4$@SnO_2 1% and $BiVO_4$@SnO_2 3% under vaccum conditions. The films were prepared by drop-casting an aqueous suspension containing the particles onto FTO substrate. Transient absorption spectra of b) unmodified $BiVO_4$ and $BiVO_4$@SnO_2 1% and 3% in the absence of an applied

bias, c) at 1.23 V_{RHE} for $BiVO_4$ and $BiVO_4$@SnO_2 1% and d) for $BiVO_4$@SnO_2 1% without applied bias and at 1.23 V_{RHE}.

According to the band alignment of $BiVO_4$, SnO_2 and FTO, electrons can be easily transferred from the conduction band of $BiVO_4$ to that of SnO_2 and then to the FTO substrate, whereas the holes remain in the film.[264] The increase in the CPD signal of the $BiVO_4$@SnO_2 1% and 3% samples (more negative signals) indicates the higher photochemical charge separation by incorporation of SnO_2. Even though the 3% of SnO_2 signal was lower than that of 1%, both showed higher photovoltage than pristine $BiVO_4$, indicating the positive effect in charge separation process, where more electrons can be tranferred towards the FTO substrate and away from the Kelvin probe, due to the good coupling between $BiVO_4$ and SnO_2 particles.

Transient absorption spectroscopy (TAS) was used to examine the charge carrier dynamics of ultra-thin SnO_2 passivation layer on $BiVO_4$ and are presented in Figures 4.9b-d. The charge carrier dynamics on $BiVO_4$-based photoelectrodes were probed within a microsecond to second time scale, in 0.1 M phosphate buffer (KPi) as electrolyte. Both unmodified $BiVO_4$ and $BiVO_4$@SnO_2 samples present an absorption decay profile at ~550 nm, previously attributed to photogenerated holes.[236] It can be clearly seen that in the absence of an external bias (Figure 4.9b), the amplitude of mΔOD as well as the lifetime of photogenerated holes are exactly the same for unmodified and $BiVO_4$@SnO_2 samples. As the applied potential is increased, unmodified $BiVO_4$ presents exactly the same behavior as for unbiased profile, indicating that charge recombination still prevails in the sample. For $BiVO_4$@SnO_2 1%, which is the sample that generated the highest amount O_2, it is observed a significant enhancement of the mΔOD signal compared to unmodified $BiVO_4$, although the lifetime of the photogenerated holes was analogous. Finally, observing the unbiased spectrum and that at 1.23 V_{RHE}, $BiVO_4$@SnO_2 1% presents aproximately a two-fold enhancement of mΔOD signal, indicating that more holes, that did not recombine with electrons, are obtained upon increasing the applied potential. Despite no significant change in the lifetime of the photogenerated holes, the higher mΔOD signal of $BiVO_4$@SnO_2 1% compared to that for 3% and unmodified $BiVO_4$, corroborated with SPS and O_2 evolution tests.

Regarding the poor activity of unmodified $BiVO_4$ for O_2 evolution, it might be resulted from the effect of relative exposure of {010} and {110} facets. As mentioned, it has been reported that {010} facet is more efficient for photooxidation performance.[242] Dodecahedron geometry for $BiVO_4$ can result in two different shapes. One is the

truncated bipyramid shape, which presents greater extent of electron trapping, resulting in inferior performance, and the second is the platelike shape, where larger {010} facets, associated with superior photooxidation activity.[266] Our obtained $BiVO_4$ particles were found to be closer to truncated bipyramid shape (see in Figure C1b – Appendix C), resulting in high electron-hole recombination and poor performance for O_2 evolution. However, after the incorporation of thin SnO_2 conformal layer over $BiVO_4$ surface, charge recombination became less pronounced, resulting in boosted O_2 evolution.

In this study, the results showed that ultra-thin SnO_2 conformal layer was indispensable to inhibit surface recombination on $BiVO_4$, resulting in higher evolved O_2, during water oxidation tests. Although poor activity was obtained for unmodified $BiVO_4$ photocatalyst, better charge separation and transport were obtained for $BiVO_4$@SnO_2 materials. Further studies are needed in order to optime the size distribution of the $BiVO_4$ particles, since despite larger particles are positive for surface coverage with thin passivation layers, in PEC experiments, such behavior trends to affect charge carrier recombination.

4.4 Partial conclusion

In conclusion, this work described the improvement in O_2 evolution rate upon SnO_2 incorporation over $BiVO_4$ surface, acting as an effective conformal layer. Photoelectrochemical and TAS measurements have shown that higher photocurrent followed by higher amount of photogenerated holes. The results reveal that an optimal thickness must be thin enough to avoid charge recombination and maintain light absorption by $BiVO_4$ particles. Further experiments need to be carried out to well control size and morphology with the addition of proper cocatalysts for an achievement of higher performance toward O_2 evolution with better stability as well as reproducibility.

5. Final Remarks

In the first part of this thesis, the addition of SLG onto α-Fe_2O_3 photoanode showed a substantial improvement in the photocurrent density by suppressing charge recombination at surface states. Despite plenty of works have already shown this improvements, the real role of graphene is still unclear. By the outcomes obtained using TAS and SPS techniques in this work, it was possible to conclude that the addition of SLG was crucial for increasing the lifetime of the photogenerated holes and consequently, obtaining higher photocurrent density.

In the second part, Co-NC-Fe addition over α-Fe_2O_3 photoanode showed that even at mild conditions, higher PEC performance can be obtained with enhanced photostability. In addition, the use of *in-situ* UV-Vis and FTIR techniques was of major importance in obtaining accurate results to elucidate important chemical processes responsible for better performance towards water oxidation.

In the final part of this thesis, it was shown the importance of protecting the $BiVO_4$ surface against charge recombination and photocorrosion for enhanced O_2 evolution. By combining all results, it is important to mention that despite better performances can be obtained by using a wide range of surface modifications, no material can overcome the major drawbacks by itself, it is always necessary the addition of a second material to extract synergistic effects.

In summary, this thesis reported the importance of modifying the surface of the semiconductors to improve their stability and efficiency for PEC applications. It is worthy to mention that despite possessing many advantage for using as a semiconductor for PEC photoanodes, their application under mild condition is a vital importance to the development of suitable systems for commercial applications, considering cost, stability and affordability.

Despite much progress, the understanding of the fundamental aspects of the processes that take place under operating conditions is indispensable to gain more precise insights for the development of efficient nanomaterials for solar enegy conversion applications. Therefore, the use of a robust and powerful set of techniques for probing charge carrier dynamics and structureal properties of short-lives excited states during PEC water splitting has proven the vital importance of understanding the mechanisms underlying charge separation and transport for materials development of better photoanodes.

7. References

1 M. Z. Jacobson, *Energy Environ. Sci.*, 2009, 2, 148–173.

2 *Proc. Natl. Acad. Sci.*, 2007, **104**, 20142.

3 W. Li, H. Wang, X. Jiang, J. Zhu, Z. Liu, X. Guo and C. Song, *RSC Adv.*, 2018, 8, 7651–7669.

4 http://berkeleyearth.org/ - Accessed on 7 October, 2020.

5 https://ourworldindata.org/ - Accessed on 7 October, 2020.

6 https://scied.ucar.edu/learning-zone/impacts-climate-change/predictions-future-global-climate - Accessed on 13 October, 2020.

7 I. Staffell, D. Scamman, A. Velazquez Abad, P. Balcombe, P. E. Dodds, P. Ekins, N. Shah and K. R. Ward, *Energy Environ. Sci.*, 2019, 12, 463–491.

8 https://www.climatewatchdata.org/ - Accessed on 9 October, 2020.

9 S. Y. Tee, K. Y. Win, W. S. Teo, L. D. Koh, S. Liu, C. P. Teng and M. Y. Han, *Adv. Sci.*, 2017, 4, 1600337.

10 R. D. Tentu and S. Basu, *Curr. Opin. Electrochem.*, 2017, 5, 56–62.

11 https://www.nortonrosefulbright.com/en/knowledge/publications/e9f3153d/the-potential-of-hydrogen - Accessed on 11 October, 2020.

12 B. Dou, H. Zhang, Y. Song, L. Zhao, B. Jiang, M. He, C. Ruan, H. Chen and Y. Xu, *Sustain. Energy Fuels*, 2019, 3, 314–342.

13 M. Balat, *Int. J. Hydrogen Energy*, 2008, **33**, 4013–4029.

14 T. A. Napp, A. Gambhir, T. P. Hills, N. Florin and P. S. Fennell, *Renew. Sustain. Energy Rev.*, 2014, 30, 616–640.

15 M. Ball and M. Weeda, *Int. J. Hydrogen Energy*, 2015, **40**, 7903–7919.

16 J. Su and L. Vayssieres, *ACS Energy Lett.*, 2016, 1, 1, 121–135.

17 A. G. Tamirat, J. Rick, A. A. Dubale, W. N. Su and B. J. Hwang, *Nanoscale Horizons*, 2016, 1, 243–267.

18 M. D. Bhatt and J. S. Lee, *J. Mater. Chem. A*, 2015, **3**, 10632–10659.

19 S. Chen, D. Huang, P. Xu, W. Xue, L. Lei, M. Cheng, R. Wang, X. Liu and R. Deng, *J. Mater. Chem. A*, 2020, 8, 2286–2322.

20 J. Tang, J. R. Durrant and D. R. Klug, *J. Am. Chem. Soc.*, 2008, **130**, 13885–13891.

21 M. Tayebi and B. K. Lee, *Renew. Sustain. Energy Rev.*, 2019, 111, 332–343.

22 P. Dias, T. Lopes, L. Meda, L. Andrade and A. Mendes, *Phys. Chem. Chem. Phys.*, 2016, **18**, 5232–5243.

23 D. M. F. Santos, C. A. C. Sequeira and J. L. Figueiredo, *Quim. Nova*, 2013, **36**, 1176–1193.

24 F. E. Osterloh, *ACS Energy Lett.*, 2017, 2, 2, 445–453.

25 K. Maeda, *J. Photochem. Photobiol. C Photochem. Rev.*, 2011, 12, 4, 237–268.

26 X. Yang and D. Wang, *ACS Appl. Energy Mater.*, 2018, 1, 12, 6657–6693.

27 A. Fujishima and K. Honda, *Nature*, 1972, **235**, 37–38.

28 Y. Yang, S. Niu, D. Han, T. Liu, G. Wang and Y. Li, *Adv. Energy Mater.*, 2017, 7, 1700555.

29 T. Hisatomi, J. Kubota and K. Domen, *Chem. Soc. Rev.*, 2014, 43, 7520–7535.

30 K. S. Joya, Y. F. Joya, K. Ocakoglu and R. Van De Krol, *Angew. Chemie* -

Int. Ed., 2013, 52, 10426–10437.

31 T. Horita and H. Yokokawa, in *Materials for Energy Conversion Devices: A Volume in Woodhead Publishing Series in Electronic and Optical Materials*, 2005, p. Chapter 2.

32 S. A. Razek, M. R. Popeil, L. Wangoh, J. Rana, N. Suwandaratne, J. L. Andrews, D. F. Watson, S. Banerjee and L. F. J. Piper, *Electron. Struct.*, , DOI:10.1088/2516-1075/ab7d86.

33 K. Takanabe, *ACS Catal.*, 2017, **7**, 8006–8022.

34 L. M. Peter, in *RSC Energy and Environment Series*, 2016, p. Chapter 1, 10.

35 Gurudayal, P. S. Bassi, T. Sritharan and L. H. Wong, *J. Phys. D. Appl. Phys.*, 2018, 51, 473002.

36 C. Jiang, S. J. A. Moniz, A. Wang, T. Zhang and J. Tang, *Chem. Soc. Rev.*, 2017, 46, 4645–4660.

37 C. Ros, T. Andreu and J. R. Morante, *J. Mater. Chem. A*, 2020, 8, 10625–10669.

38 J. Zhang and S. Eslava, *Sustain. Energy Fuels*, 2019, 3, 1351–1364.

39 O. F. Sankey, *J. Vac. Sci. Technol. B Microelectron. Nanom. Struct.*, 1985, **3**, 1162–1166.

40 P. Y. Tang and J. Arbiol, *Nanoscale Horizons*, 2019, **4**, 1256–1276.

41 P. Y. Tang, L. J. Han, F. S. Hegner, P. Paciok, M. Biset-Peiró, H. C. Du, X. K. Wei, L. Jin, H. B. Xie, Q. Shi, T. Andreu, M. Lira-Cantú, M. Heggen, R. E. Dunin-Borkowski, N. López, J. R. Galán-Mascarós, J. R. Morante and J. Arbiol, *Adv. Energy Mater.*, 2019, **9**, 1901836.

42 J. Zhang and S. Eslava, *Sustain. Energy Fuels*, 2019, 3,1351-1364.

43 A. Annamalai, A. Subramanian, U. Kang, H. Park, S. H. Choi and J. S. Jang, *J. Phys. Chem. C*, 2015, **119**, 3810–3817.

44 R. Liu, Z. Zheng, J. Spurgeon and X. Yang, *Energy Environ. Sci.*, 2014, 7, 2504–2517.

45 R. M. Cornell and U. Schwertmann, *The Iron Oxides*, 2003.

46 K. Sivula, F. Le Formal and M. Grätzel, *ChemSusChem*, 2011, 4, 432–449.

47 K. Sivula, R. Zboril, F. Le Formal, R. Robert, A. Weidenkaff, J. Tucek, J. Frydrych and M. Grätzel, *J. Am. Chem. Soc.*, 2010, **132**, 7436–7444.

48 B. Iandolo, B. Wickman, I. Zorić and A. Hellman, *J. Mater. Chem. A*, 2015, **3**, 16896–16912.

49 J. Y. Kim, G. Magesh, D. H. Youn, J. W. Jang, J. Kubota, K. Domen and J. S. Lee, *Sci. Rep.*, 2013, **3**, 2681.

50 P. Dias, A. Vilanova, T. Lopes, L. Andrade and A. Mendes, *Nano Energy*, 2016, **23**, 70–79.

51 P. Tang, H. Xie, C. Ros, L. Han, M. Biset-Peiró, Y. He, W. Kramer, A. P. Rodríguez, E. Saucedo, J. R. Galán-Mascarós, T. Andreu, J. R. Morante and J. Arbiol, *Energy Environ. Sci.*, 2017, **10**, 2124–2136.

52 P. S. Archana, N. Pachauri, Z. Shan, S. Pan and A. Gupta, *J. Phys. Chem. C*, 2015, **119**, 15506–15516.

53 Q. Wu, J. Zhao, K. Liu, H. Wang, Z. Sun, P. Li and S. Xue, *Int. J. Hydrogen Energy*, 2015, **40**, 6763–6770.

54 K. Maabong, A. G. J. Machatine, B. S. Mwankemwa, A. Braun, D. K. Bora, R.

Toth and M. Diale, *Phys. B Condens. Matter*, 2018, **535**, 67–71.

55 D. H. Kim, D. M. Andoshe, Y. S. Shim, C. W. Moon, W. Sohn, S. Choi, T. L. Kim, M. Lee, H. Park, K. Hong, K. C. Kwon, J. M. Suh, J. S. Kim, J. H. Lee and H. W. Jang, *ACS Appl. Mater. Interfaces*, , DOI:10.1021/acsami.6b05366.

56 I. S. Cho, H. S. Han, M. Logar, J. Park and X. Zheng, *Adv. Energy Mater.*, 2016, **6**, 1501840.

57 S. Shen, S. A. Lindley, X. Chen and J. Z. Zhang, *Energy Environ. Sci.*, 2016, 9, 2744–2775.

58 J. Y. Kim, D. H. Youn, J. H. Kim, H. G. Kim and J. S. Lee, *ACS Appl. Mater. Interfaces*, 2015, **7**, 14123–14129.

59 Y. J. Chen and L. Y. Chen, in *Energy Procedia*, 2014, pp. 61, 2046–2049.

60 S. Shen, J. Zhou, C. L. Dong, Y. Hu, E. N. Tseng, P. Guo, L. Guo and S. S. Mao, *Sci. Rep.*, 2014, **15**, 6627.

61 X. Guo, L. Wang and Y. Tan, *Nano Energy*, 2015, **16**, 320–328.

62 J. Liu, M. Shahid, Y. S. Ko, E. Kim, T. K. Ahn, J. H. Park and Y. U. Kwon, *Phys. Chem. Chem. Phys.*, 2013, **15**, 9775–9782.

63 M. T. Mayer, Y. Lin, G. Yuan and D. Wang, *Acc. Chem. Res.*, 2013, **46**, 1558–1566.

64 J. Young Kim, J. W. Jang, D. Hyun Youn, J. Yul Kim, E. Sun Kim and J. Sung Lee, *RSC Adv.*, , DOI:10.1039/c2ra21169f.

65 J. Deng, X. Lv, J. Gao, A. Pu, M. Li, X. Sun and J. Zhong, *Energy Environ. Sci.*, 2013, **6**, 1965–1970.

66 T. J. Smart and Y. Ping, *J. Phys. Condens. Matter*, , DOI:10.1088/1361-

648X/aa7e3d.

67 N. J. Cherepy, D. B. Liston, J. A. Lovejoy, H. Deng and J. Z. Zhang, *J. Phys. Chem. B*, 1998, **102**, 770–776.

68 I. Concina, Z. H. Ibupoto and A. Vomiero, *Adv. Energy Mater.*, 2017, 7, 1700706.

69 B. Iandolo, H. Zhang, B. Wickman, I. Zorić, G. Conibeer and A. Hellman, *RSC Adv.*, 2015, **5**, 61021.

70 B. Iandolo and A. Hellman, *Angew. Chemie*, 2014, **53**, 13404–13408.

71 L. Palmolahti, H. Ali-Löytty, R. Khan, J. Saari, N. V. Tkachenko and M. Valden, *J. Phys. Chem. C*, 2020, **124**, 13094–13101.

72 A. M. Dos Santos, D. Beliaev, L. M. R. Scolfaro and J. R. Leite, *Brazilian J. Phys.*, 1999, **29**, 775–778.

73 J. Brillet, M. Comuz, F. Le Formal, J. H. Yum, M. Grätzel and K. Sivula, *J. Mater. Res.*, 2010, **25**, 17–24.

74 C. A. Mesa, L. Steier, B. Moss, L. Francàs, J. E. Thorne, M. Grätzel and J. R. Durrant, *J. Phys. Chem. Lett.*, 2020, **11**, 7285–7290.

75 C. A. Mesa, L. Francàs, K. R. Yang, P. Garrido-Barros, E. Pastor, Y. Ma, A. Kafizas, T. E. Rosser, M. T. Mayer, E. Reisner, M. Grätzel, V. S. Batista and J. R. Durrant, *Nat. Chem.*, 2020, **12**, 82–89.

76 F. Le Formal, E. Pastor, S. D. Tilley, C. A. Mesa, S. R. Pendlebury, M. Grätzel and J. R. Durrant, *J. Am. Chem. Soc.*, 2015, **137**, 6629–6637.

77 B. Klahr, S. Gimenez, F. Fabregat-Santiago, T. Hamann and J. Bisquert, *J. Am. Chem. Soc.*, 2012, **134**, 4294–4302.

78 N. Guijarro, M. S. Prévot and K. Sivula, *Phys. Chem. Chem. Phys.*, 2015, 17(24), 15655–15674.

79 Y. Zhang, H. Zhang, H. Ji, W. Ma, C. Chen and J. Zhao, *J. Am. Chem. Soc.*, 2016, **138**, 2705–2711.

80 Y. Zhang, H. Zhang, A. Liu, C. Chen, W. Song and J. Zhao, *J. Am. Chem. Soc.*, 2018, **140**, 3264–3269.

81 Y. Liu, F. Le Formal, F. Boudoire and N. Guijarro, *ACS Appl. Energy Mater.*, 2019, **2**, 6825–6833.

82 M. Barroso, S. R. Pendlebury, A. J. Cowan and J. R. Durrant, *Chem. Sci.*, 2013, 4, 2724–2734.

83 F. Le Formal, S. R. Pendlebury, M. Cornuz, S. D. Tilley, M. Grätzel and J. R. Durrant, *J. Am. Chem. Soc.*, 2014, **136**, 2564–2574.

84 R. F. G. Gardner, F. Sweett and D. W. Tanner, *J. Phys. Chem. Solids*, 1963, **24**, 1183–1186.

85 I. Cesar, K. Sivula, A. Kay, R. Zboril and M. Grätzel, *J. Phys. Chem. C*, 2009, **113**, 772–782.

86 L. M. Peter, K. G. U. Wijayantha and A. A. Tahir, *Faraday Discuss.*, 2012, **155**, 309–322.

87 S. M. Ahmed, J. Leduc and S. F. Haller, *J. Phys. Chem.*, 1988, **92**, 6655–6660.

88 G. Horowitz, *J. Electroanal. Chem.*, 1983, **159**, 421–436.

89 C. Ruckebusch, M. Sliwa, P. Pernot, A. de Juan and R. Tauler, *J. Photochem. Photobiol. C Photochem. Rev.*, 2012, 13, 1, 1–27.

90 A. M. Peiró, C. Colombo, G. Doyle, J. Nelson, A. Mills and J. R. Durrant, *J.*

Phys. Chem. B, 2006, **110**, 23255–23266.

91 C. C. Hung, A. Yabushita, T. Kobayashi, P. F. Chen and K. S. Liang, *Chem. Phys. Lett.*, 2017, **683**, 691--624.

92 G. X. Pei, J. H. J. Wijten and B. M. Weckhuysen, *Phys. Chem. Chem. Phys.*, 2018, **20**, 9806.

93 Z. Huang, Y. Lin, X. Xiang, W. Rodríguez-Córdoba, K. J. McDonald, K. S. Hagen, K. S. Choi, B. S. Brunschwig, D. G. Musaev, C. L. Hill, D. Wang and T. Lian, *Energy Environ. Sci.*, 2012, 5, 8923–8926.

94 J. Wang, J. Zhao and F. E. Osterloh, *Energy Environ. Sci.*, 2015, **8**, 2970–2976.

95 D. Cavalcoli and A. Cavallini, *Phys. Status Solidi Curr. Top. Solid State Phys.*, 2010, **7**, 1293–1300.

96 M. A. Melo, Z. Wu, B. A. Nail, A. T. De Denko, A. F. Nogueira and F. E. Osterloh, *Nano Lett.*, 2018, **18**, 805–810.

97 J. Zhao, B. A. Nail, M. A. Holmes and F. E. Osterloh, *J. Phys. Chem. Lett.*, 2016, **7**, 3335–3340.

98 T. L. Shelton, N. Harvey, J. Wang and F. E. Osterloh, *Appl. Catal. A Gen.*, 2016, **521**, 168–173.

99 S. D. Singh, S. Porwal, A. K. Sinha and T. Ganguli, *Semicond. Sci. Technol.*, 2017, **32**, 1–8.

100 M. A. Melo, S. A. Carminati, J. Bettini and A. F. Nogueira, *Sustain. Energy Fuels*, 2018, **2**, 958–967.

101 H. L. Tan, A. Suyanto, A. T. De Denko, W. H. Saputera, R. Amal, F. E. Osterloh and Y. H. Ng, *Part. Part. Syst. Charact.*, 2017, **34**, 1600290.

102 J. Zhao and F. E. Osterloh, *J. Phys. Chem. Lett.*, 2014, **5**, 782–786.

103 H. Nguyen Bich and H. Nguyen Van, *Adv. Nat. Sci. Nanosci. Nanotechnol.*, 2016, 7, 2.

104 C. A. Mesa, A. Kafizas, L. Francàs, S. R. Pendlebury, E. Pastor, Y. Ma, F. Le Formal, M. T. Mayer, M. Grätzel and J. R. Durrant, *J. Am. Chem. Soc.*, 2017, **139**, 11537–11543.

105 S. R. Pendlebury, M. Barroso, A. J. Cowan, K. Sivula, J. Tang, M. Grätzel, D. Klug and J. R. Durrant, *Chem. Commun.*, 2011, **47**, 716–718.

106 K. E. Whitener and P. E. Sheehan, *Diam. Relat. Mater.*, 2014, 46, 25–34.

107 C. Biswas and Y. H. Lee, *Adv. Funct. Mater.*, 2011, 21, 20, 3806–3826.

108 S. F. Duan, C. L. Tao, Y. Y. Geng, X. Q. Yao, X. W. Kang, J. Z. Su, I. Rodríguez-Gutiérrez, M. Kan, M. Romero, Y. Sun, Y. X. Zhao, D. D. Qin and Y. Yan, *ChemCatChem*, 2019, **11**, 729–736.

109 Y. R. Kim, S. Bong, Y. J. Kang, Y. Yang, R. K. Mahajan, J. S. Kim and H. Kim, *Biosens. Bioelectron.*, 2010, **25**, 2366–2369.

110 Y. Wang, Y. Wan and D. Zhang, *Electrochem. commun.*, 2010, **12**, 187–190.

111 L. Yang, X. Li, G. Zhang, P. Cui, X. Wang, X. Jiang, J. Zhao, Y. Luo and J. Jiang, *Nat. Commun.*, 2017, **8**, 16049.

112 C. Berger, Z. Song, X. Li, X. Wu, N. Brown, C. Naud, D. Mayou, T. Li, J. Hass, A. N. Marchenkov, E. H. Conrad, P. N. First and W. A. De Heer, *Science (80-.).*, 2006, **312**, 1191–1196.

113 K. S. Kim, Y. Zhao, H. Jang, S. Y. Lee, J. M. Kim, K. S. Kim, J. H. Ahn, P. Kim, J. Y. Choi and B. H. Hong, *Nature*, 2009, **457**, 706–710.

114 M. Sang, J. Shin, K. Kim and K. J. Yu, *Nanomaterials*, 2019, 9, 3, 374.

115 T. Zhong and M. Wu, *Phys. Chem. Chem. Phys.*, 2020, **22**, 12039.

116 Q. Xu, W. Li, L. Ding, W. Yang, H. Xiao and W. J. Ong, *Nanoscale*, 2019, 11, 1475–1504.

117 J. Fayos, *J. Solid State Chem.*, 1999, **148**, 278–285.

118 X. Li, Y. Zhu, W. Cai, M. Borysiak, B. Han, D. Chen, R. D. Piner, L. Colomba and R. S. Ruoff, *Nano Lett.*, 2009, **9**, 4359–4363.

119 X. Xie, K. Kretschmer and G. Wang, *Nanoscale*, 2015, **7**, 13278–13292.

120 X. Liu, Y. Wen, Z. Chen, H. Lin, R. Chen, K. Cho and B. Shan, *AIP Adv.*, 2013, **3**, 052126.

121 A. Pérez-Tomás, A. Mingorance, D. Tanenbaum and M. Lira-Cantú, in *The Future of Semiconductor Oxides in Next-Generation Solar Cells*, 2018, p. Chapter 10, 395-437.

122 J. Plutnar, M. Pumera and Z. Sofer, *J. Mater. Chem. C*, 2018, 6, 6082–6101.

123 T. Lin, Y. Tang, Y. Wang, H. Bi, Z. Liu, F. Huang, X. Xie and M. Jiang, *Energy Environ. Sci.*, 2013, **6**, 1283–1290.

124 S. Pei and H. M. Cheng, *Carbon N. Y.*, 2012, **50**, 3210–3228.

125 M. Liu, X. Zhang, W. Wu, T. Liu, Y. Liu, B. Guo and R. Zhang, *Chem. Eng. J.*, 2019, **355**, 181–185.

126 N. I. Zaaba, K. L. Foo, U. Hashim, S. J. Tan, W. W. Liu and C. H. Voon, in *Procedia Engineering*, 2017, pp. 184, 469–477.

127 M. S. A. Sher Shah, A. R. Park, K. Zhang, J. H. Park and P. J. Yoo, *ACS Appl. Mater. Interfaces*, 2012, **4**, 3893–3901.

128 A. Cao, Z. Liu, S. Chu, M. Wu, Z. Ye, Z. Cai, Y. Chang, S. Wang, Q. Gong and Y. Liu, *Adv. Mater.*, 2010, **22**, 103–106.

129 G. Williams, B. Seger and P. V. Kamt, *ACS Nano*, 2008, **2**, 1487–1491.

130 S. Do Amaral Carminati, F. L. Souza and A. F. Nogueira, *ChemPhysChem*, 2016, **17**, 170–177.

131 M. P. Cardona, M. Li, W. Li, J. McCall, D. Wang, Y. Li and C. Yang, *Mater. Today Energy*, 2018, **8**, 8–14.

132 C. Das, B. Ananthoju, A. K. Dhara, M. Aslam, S. K. Sarkar and K. R. Balasubramaniam, *Adv. Mater. Interfaces*, 2017, **4**, 1700271.

133 R. M. Jacobberger, R. Machhi, J. Wroblewski, B. Taylor, A. L. Gillian-Daniel and M. S. Arnold, *J. Chem. Educ.*, 2015, **92**, 1903–1907.

134 S. Chaitoglou, E. Bertran and J. L. Andujar, in *Graphene Materials - Structure, Properties and Modifications*, 2017.

135 X. Li, P. S. Bassi, P. P. Boix, Y. Fang and L. H. Wong, *ACS Appl. Mater. Interfaces*, 2015, **7**, 16960–16966.

136 L. Vayssieres, N. Beermann, S. E. Lindquist and A. Hagfeldt, *Chem. Mater.*, 2001, **13**, 233–235.

137 N. M. Ito, W. M. Carvalho, D. N. F. Muche, R. H. R. Castro, G. M. Dalpian and F. L. Souza, *Phys. Chem. Chem. Phys.*, 2017, **19**, 25025–25032.

138 L. C. C. Ferraz, W. M. Carvalho, D. Criado and F. L. Souza, *ACS Appl. Mater. Interfaces*, 2012, **4**, 5515–5523.

139 G. B. Barin, Y. Song, I. D. F. Gimenez, A. G. S. Filho, L. S. Barreto and J. Kong, *Carbon N. Y.*, 2015, **84**, 82–90.

140 N. A. Nayan and N. Ramli, *Int. J. Appl. Eng. Res.*, 2016, **11**, 7815–7822.

141 A. Annamalai, P. S. Shinde, T. H. Jeon, H. H. Lee, H. G. Kim, W. Choi and J. S. Jang, *Sol. Energy Mater. Sol. Cells*, , DOI:10.1016/j.solmat.2015.09.016.

142 M. Cornuz, M. Grätzel and K. Sivula, *Chem. Vap. Depos.*, 2010, **16**, 291–295.

143 W. M. Carvalho and F. L. Souza, *ChemPhysChem*, 2016, **17**, 2710–2717.

144 T. W. Hamann, *Dalt. Trans.*, 2012, **41**, 7830–7834.

145 P. Qiu, H. Yang, L. Yang, Q. Wang and L. Ge, *Electrochim. Acta*, 2018, **266**, 431–440.

146 R. H. Gonçalves, B. H. R. Lima and E. R. Leite, *J. Am. Chem. Soc.*, 2011, **133**, 6012–6019.

147 T. Choi, H. Jung, C. W. Lee, K. Y. Mun, S. H. Kim, J. Park and H. Kim, *Appl. Surf. Sci.*, 2015, **343**, 128–132.

148 A. Fujimoto, Y. Yamada, M. Koinuma and S. Sato, *Anal. Chem.*, , DOI:10.1021/acs.analchem.6b01327.

149 J. W. Suk, A. Kitt, C. W. Magnuson, Y. Hao, S. Ahmed, J. An, A. K. Swan, B. B. Goldberg and R. S. Ruoff, *ACS Nano*, , DOI:10.1021/nn201207c.

150 O. Frank, M. Mohr, J. Maultzsch, C. Thomsen, I. Riaz, R. Jalil, K. S. Novoselov, G. Tsoukleri, J. Parthenios, K. Papagelis, L. Kavan and C. Galiotis, *ACS Nano*, 2011, **5**, 2231–2239.

151 C. Metzger, S. Rémi, M. Liu, S. V. Kusminskiy, A. H. Castro Neto, A. K. Swan and B. B. Goldberg, *Nano Lett.*, 2010, **10**, 6–10.

152 J. W. Suk, A. Kitt, C. W. Magnuson, Y. Hao, S. Ahmed, J. An, A. K. Swan, B. B. Goldberg and R. S. Ruoff, *ACS Nano*, 2011, **5**, 6916–6924.

153 J. Qu, Y. X. Yin, Y. Q. Wang, Y. Yan, Y. G. Guo and W. G. Song, *ACS Appl. Mater. Interfaces*, 2013, **5**, 3932–3936.

154 X. Zhang, J. Zhou, H. Song, C. Liu, S. Zhang and X. Chen, *Carbon N. Y.*, 2016, **99**, 370–374.

155 G. Xie, K. Zhang, B. Guo, Q. Liu, L. Fang and J. R. Gong, *Adv. Mater.*, 2013, 25, 3820–3839.

156 L. J. Yang, Q. L. Liu, M. X. Wang, L. S. Gu, Y. H. Luo and B. W. Sun, *Spectrochim. Acta - Part A Mol. Biomol. Spectrosc.*, 2016, **166**, 1–7.

157 R. A. Segura, F. Olivares, J. Maze, P. Häberle and R. Henríquez, *J. Nanomater.*, 2016, 1–6.

158 M. G. Ahmed, I. E. Kretschmer, T. A. Kandiel, A. Y. Ahmed, F. A. Rashwan and D. W. Bahnemann, *ACS Appl. Mater. Interfaces*, 2015, **7**, 24053–24062.

159 S. R. Pendlebury, X. Wang, F. Le Formal, M. Cornuz, A. Kafizas, S. D. Tilley, M. Grätzel and J. R. Durrant, *J. Am. Chem. Soc.*, 2014, **136**, 9854–9857.

160 A. Iqbal, S. Yuan, Z. Wang and K. H. Bevan, *J. Phys. Chem. C*, 2018, **122**, 23878–23889.

161 A. G. Tamirat, A. A. Dubale, W. N. Su, H. M. Chen and B. J. Hwang, *Phys. Chem. Chem. Phys.*, 2017, **19**, 20881–20890.

162 K. D. Rasamani, Z. Li and Y. Sun, *Nanoscale*, 2016, **8**, 18621–18625.

163 B. P. Bloom, M. N. Mendis, E. Wierzbinski and D. H. Waldeck, *J. Mater. Chem. C*, 2016, **4**, 704–712.

164 O. Zandi and T. W. Hamann, *Phys. Chem. Chem. Phys.*, 2015.

165 O. Zandi and T. W. Hamann, *J. Phys. Chem. Lett.*, 2014, **5**, 1522–1526.

166 B. Klahr and T. Hamann, *J. Phys. Chem. C*, 2014, **118**, 10393–10399.

167 P. J. Ferko, J. R. Withers, H. Nguyen, J. Ema, T. Ema, C. Allison, C. Dornhoefer, N. P. Rath and S. M. Holmes, *J. Chem. Educ.*, 2017, **94**, 95–100.

168 S. Pintado, S. Goberna-Ferrón, E. C. Escudero-Adán and J. R. Galán-Mascarós, *J. Am. Chem. Soc.*, 2013, **135**, 13270–13273.

169 A. Paolella, C. Faure, V. Timoshevskii, S. Marras, G. Bertoni, A. Guerfi, A. Vijh, M. Armand and K. Zaghib, *J. Mater. Chem. A*, 2017, 5, 18919.

170 P. Nie, L. Shen, H. Luo, B. Ding, G. Xu, J. Wang and X. Zhang, *J. Mater. Chem. A*, 2014, **2**, 5852–5857.

171 S. Bonhommeau, N. Pontius, S. Cobo, L. Salmon, F. M. F. De Groot, G. Molnár, A. Bousseksou, H. A. Dürr and W. Eberhardt, *Phys. Chem. Chem. Phys.*, 2008, **10**, 5882–5889.

172 F. Zhao, Y. Wang, X. Xu, Y. Liu, R. Song, G. Lu and Y. Li, *ACS Appl. Mater. Interfaces*, 2014, **6**, 11007–11012.

173 Z. Qin, Y. Li and N. Gu, *Adv. Healthc. Mater.*, 2018, 7, 1800347.

174 F. S. Hegner, J. R. Galán-Mascarós and N. López, *Inorg. Chem.*, 2016, **55**, 12851–12862.

175 G. Liu, P. Li, G. Zhao, X. Wang, J. Kong, H. Liu, H. Zhang, K. Chang, X. Meng, T. Kako and J. Ye, *J. Am. Chem. Soc.*, 2016, **138**, 9128–9136.

176 B. Moss, F. S. Hegner, S. Corby, S. Selim, L. Francàs, N. López, S. Giménez, J. R. Galán-Mascarós and J. R. Durrant, *ACS Energy Lett.*, 2019, **4**, 337–342.

177 Y. Surendranath, M. W. Kanan and D. G. Nocera, *J. Am. Chem. Soc.*, 2010, **132**, 16501–16509.

178 M. Aller-Pellitero, J. Fremeau, R. Villa, G. Guirado, B. Lakard, J. Y. Hihn and F. J. del Campo, *Sensors Actuators, B Chem.*, 2019, **290**, 591–597.

179 S. H. Lee, J. H. Chung, H. K. Park and G. J. Lee, *J. Sensors*, 2016, **2016**, 1859292.

180 A. A. Karyakin, *Curr. Opin. Electrochem.*, 2017, 5, 92–98.

181 B. M. Pires, P. L. Dos Santos, V. Katic, S. Strohauer, R. Landers, A. L. B. Formiga and J. A. Bonacin, *Dalt. Trans.*, 2019, **48**, 4811–4822.

182 E. P. Alsaç, E. Ülker, S. V. K. Nune, Y. Dede and F. Karadas, *Chem. - A Eur. J.*, 2018, **24**, 4856–4863.

183 B. Rodríguez-García, Á. Reyes-Carmona, I. Jiménez-Morales, M. Blasco-Ahicart, S. Cavaliere, M. Dupont, D. Jones, J. Rozière, J. R. Galán-Mascarós and F. Jaouen, *Sustain. Energy Fuels*, 2018, **2**, 589–597.

184 F. S. Hegner, I. Herraiz-Cardona, D. Cardenas-Morcoso, N. López, J. R. Galán-Mascarós and S. Gimenez, *ACS Appl. Mater. Interfaces*, 2017, **9**, 37671–37681.

185 X. Wu, M. Sun, S. Guo, J. Qian, Y. Liu, Y. Cao, X. Ai and H. Yang, *ChemNanoMat*, 2015, **1**, 188–193.

186 E. Kholoud, H. Watanabe, A. Takahashi, M. M. Emara, B. A. Abd-El-Nabey, M. Kurihara, K. Tajima and T. Kawamoto, *J. Mater. Chem. C*, 2017, **5**, 8921–8926.

187 R. O. Lezna, R. Romagnoli, N. R. De Tacconi and K. Rajeshwar, *J. Phys. Chem. B*, 2002, **106**, 3612–3621.

188 S. Zerdane, M. Cammarata, L. Balducci, R. Bertoni, L. Catala, S. Mazerat, T. Mallah, M. N. Pedersen, M. Wulff, K. Nakagawa, H. Tokoro, S. I. Ohkoshi and E. Collet, *Eur. J. Inorg. Chem.*, 2018, 272–277.

189 F. S. Hegner, D. Cardenas-Morcoso, S. Giménez, N. López and J. R. Galan-Mascaros, *ChemSusChem*, 2017, **10**, 4552–4560.

190 W. Cui, W. Niu, R. Wick-Joliat, T. Moehl and S. D. Tilley, *Chem. Sci.*, 2018, **9**, 6062–6097.

191 Y. Yuan, M. Li, Z. Bai, G. Jiang, B. Liu, T. Wu, Z. Chen, K. Amine and J. Lu, *Adv. Mater.*, 2019, 31, 1805609.

192 J. Cen, Q. Wu, M. Liu and A. Orlov, *Green Energy Environ.*, 2017, 2, 100–111.

193 Z. Liang, Q. Zou, Y. Wang and Y.-C. Lu, *Small Methods*, 2017, **1**, 1700150.

194 S. Sarker, J. J. Lamb, D. R. Hjelme and K. M. Lien, *Fuel*, 2018, 226, 686–697.

195 R. Nakamura, A. Imanishi, K. Murakoshi and Y. Nakato, *J. Am. Chem. Soc.*, 2003, **125**, 7443–7450.

196 J. J. Murcia, M. C. Hidalgo, J. A. Navío, J. Araña and J. M. Doña-Rodríguez, *Appl. Catal. B Environ.*, 2013, **142**, 205–213.

197 J. C. S. Wu and Y. T. Cheng, *J. Catal.*, 2006, **237**, 393–404.

198 S. Amaral Carminati, A. do Nascimento Barbosa, A. Luiz Martins de Freitas, F. L. Freire, F. L. Souza and A. F. Nogueira, *J. Catal.*, 2019, **372**, 109–118.

199 T. Iwasita and F. C. Nart, *Prog. Surf. Sci.*, 1997, 55, 271–340.

200 J. L. Bott-Neto, M. V. F. Rodrigues, M. C. Silva, E. B. Carneiro-Neto, G. Wosiak, J. C. Mauricio, E. C. Pereira, S. J. A. Figueroa and P. S. Fernández, *ChemElectroChem*, 2020, **7**, 1–9.

201 P. Li, E. Y. Jiang and H. L. Bai, *J. Phys. D. Appl. Phys.*, 2011, **44**, 075003.

202 Y. Zhu, P. Chen, Y. Zhou, W. Nie and Y. Xu, *J. Mater. Sci.*, 2018, **53**, 12467–

12476.

203 L. Qian and X. Yang, *Talanta*, 2006, **69**, 957–962.

204 K. Lu, B. Song, X. Gao, H. Dai, J. Zhang and H. Ma, *J. Power Sources*, 2016, **303**, 347–353.

205 K. Lu, B. Song, K. Li, J. Zhang and H. Ma, *J. Power Sources*, 2017, **370**, 98–105.

206 M. Yamada, M. Arai, M. Kurihara, M. Sakamoto and M. Miyake, *J. Am. Chem. Soc.*, 2004, **126**, 9482–9483.

207 L. H. Shi, T. Wu, M. J. Wang, D. Li, Y. J. Zhang and J. H. Li, *Chinese J. Chem.*, 2005, **23**, 149–154.

208 H. B. Gray and N. A. Beach, *J. Am. Chem. Soc.*, 1963, **85**, 2922–2927.

209 O. Sato, Y. Einaga, A. Fujishima and K. Hashimoto, *Inorg. Chem.*, 1999, **38**, 4405–4412.

210 P. J. Zambiazi, A. T. N. de Moraes, R. R. Kogachi, G. O. Aparecido, A. L. B. Formiga and J. A. Bonacin, *J. Braz. Chem. Soc.*, 2020, **0**, 1–12.

211 J. Y. Kim, J. W. Jang, D. H. Youn, G. Magesh and J. S. Lee, *Adv. Energy Mater.*, 2014, **4**, 1400476.

212 Y. Yang, C. Brownell, N. Sadrieh, J. May, A. Del Grosso, D. Place, E. Leutzinger, E. Duffy, R. He, F. Houn, R. Lyon and P. Faustino, *Clin. Toxicol.*, 2007, **45**, 776.

213 G. Gurudayal, S. Y. Chiam, M. H. Kumar, P. S. Bassi, H. L. Seng, J. Barber and L. H. Wong, *ACS Appl. Mater. Interfaces*, 2014, **6**, 5862–5859.

214 T. Wang, S. Zhou, C. Zhang, J. Lian, Y. Liang and W. Yuan, *New J. Chem.*,

2014, **38**, 46–49.

215 P. Zhang, W. Wang, H. Wang, Y. Li and C. Cui, *ACS Catal.*, 2020, **10**, 10427–10435.

216 W. R. Cai, G. Y. Zhang, T. Song, X. J. Zhang and D. Shan, *Electrochim. Acta*, 2016, **198**, 32–39.

217 P. J. Kulesza, M. A. Malik, A. Denca and J. Strojek, *Anal. Chem.*, 1996, **68**, 2442–2446.

218 F. C. Nart and T. Iwasita, in *Encyclopedia of Electrochemistry*, 2003.

219 M. Berrettoni, M. Giorgetti, S. Zamponi, P. Conti, D. Ranganathan, A. Zanotto, M. L. Saladino and E. Caponetti, *J. Phys. Chem. C*, 2010, **114**, 6401–6407.

220 Y. Miseki and K. Sayama, *Catal. Sci. Technol.*, 2019, **9**, 2019–2014.

221 T. Yamamoto, N. Saso, Y. Umemura and Y. Einaga, *J. Am. Chem. Soc.*, 2009, **131**, 13196–13197.

222 C. Baumanis, J. Z. Bloh, R. Dillert and D. W. Bahnemann, *J. Phys. Chem. C*, 2011, **115**, 25442–25450.

223 K. C. Bedin, D. N. F. Muche, M. A. Melo, A. L. M. Freitas, R. V. Gonçalves and F. L. Souza, *ChemCatChem*, 2020, 12, 3156–3169.

224 H. He, A. Liao, W. Guo, W. Luo, Y. Zhou and Z. Zou, *Nano Today*, 2019, 28, 100763.

225 F. F. Abdi and S. P. Berglund, *J. Phys. D. Appl. Phys.*, 2017, 50, 193002.

226 C. Martinez Suarez, S. Hernández and N. Russo, *Appl. Catal. A Gen.*, 2015, **504**, 158–170.

227 B. S. Kalanoor, H. Seo and S. S. Kalanur, *Mater. Sci. Energy Technol.*, 2018, **1**, 49–62.

228 B. J. Trześniewski and W. A. Smith, *J. Mater. Chem. A*, 2016, **4**, 2919–2926.

229 Y. Park, K. J. Mc Donald and K. S. Choi, *Chem. Soc. Rev.*, 2013, **42**, 2321–2337.

230 A. Kudo, K. Omori and H. Kato, *J. Am. Chem. Soc.*, 1999, **121**, 11459–11467.

231 W. J. Jo, H. J. Kang, K. J. Kong, Y. S. Lee, H. Park, Y. Lee, T. Buonassisi, K. K. Gleason and J. S. Lee, *Proc. Natl. Acad. Sci. U. S. A.*, 2015, **112**, 13774–13778.

232 Z. Zhang, Y. Li, X. Jiang, W. Han, M. Xie, F. Wang and E. Xie, *Nanoscale*, 2017, **9**, 14015–14022.

233 D. Coelho, J. P. R. S. Gaudêncio, S. A. Carminati, F. W. P. Ribeiro, A. F. Nogueira and L. H. Mascaro, *Chem. Eng. J.*, 2020, **399**, 125836.

234 A. J. E. Rettie, H. C. Lee, L. G. Marshall, J. F. Lin, C. Capan, J. Lindemuth, J. S. McCloy, J. Zhou, A. J. Bard and C. B. Mullins, *J. Am. Chem. Soc.*, 2013, **135**, 11389–11396.

235 M. Ziwritsch, S. Müller, H. Hempel, T. Unold, F. F. Abdi, R. Van De Krol, D. Friedrich and R. Eichberger, *ACS Energy Lett.*, 2016, **1**, 888–894.

236 Y. Ma, S. R. Pendlebury, A. Reynal, F. Le Formal and J. R. Durrant, *Chem. Sci.*, 2014, **5**, 2964–2973.

237 S. Zhang, M. Rohloff, O. Kasian, A. M. Mingers, K. J. J. Mayrhofer, A. Fischer, C. Scheu and S. Cherevko, *J. Phys. Chem. C*, 2019, **123**, 23410–23418.

238 X. Zhou and H. Dong, *ChemCatChem*, 2019, 11, 3688–3715.

239 S. A. Razek, M. R. Popeil, L. Wangoh, J. Rana, N. Suwandaratne, J. L. Andrews, D. F. Watson, S. Banerjee and L. F. J. Piper, *Electron. Struct.*, 2020, **2**, 023001.

240 K. K. Dey, S. Gahlawat and P. P. Ingole, *J. Mater. Chem. A*, 2019, **7**, 21207–21221.

241 J. H. Kim and J. S. Lee, *Adv. Mater.*, 2019, 31, 1806938.

242 R. Li, F. Zhang, D. Wang, J. Yang, M. Li, J. Zhu, X. Zhou, H. Han and C. Li, *Nat. Commun.*, 2013, **4**, 1432.

243 X. Zhao, J. Hu, S. Chen and Z. Chen, *Phys. Chem. Chem. Phys.*, 2018, **20**, 13637–13645.

244 M. Rohloff, B. Anke, S. Zhang, U. Gernert, C. Scheu, M. Lerch and A. Fischer, *Sustain. Energy Fuels*, 2017, **1**, 1830–1846.

245 M. Tayebi and B. K. Lee, *Catal. Today*, , DOI:10.1016/j.cattod.2020.03.066.

246 K. H. Ye, H. Li, D. Huang, S. Xiao, W. Qiu, M. Li, Y. Hu, W. Mai, H. Ji and S. Yang, *Nat. Commun.*, 2019, **10**, 3687.

247 Y. Liang and J. Messinger, *Phys. Chem. Chem. Phys.*, 2014, **16**, 12014–12020.

248 Y. Zhang, L. Shi, Z. Geng, T. Ren and Z. Yang, *Sci. Rep.*, 2019, **9**, 19090.

249 H. S. Han, S. Shin, D. H. Kim, I. J. Park, J. S. Kim, P. S. Huang, J. K. Lee, I. S. Cho and X. Zheng, *Energy Environ. Sci.*, 2018, **11**, 1299–1306.

250 A. Reynal, J. Willkomm, N. M. Muresan, F. Lakadamyali, M. Planells, E. Reisner and J. R. Durrant, *Chem. Commun.*, 2014, **50**, 12768–12771.

251 A. Kafizas, X. Xing, S. Selim, C. A. Mesa, Y. Ma, C. Burgess, M. A. McLachlan and J. R. Durrant, *Catal. Today*, 2019, **321**–**322**, 59–66.

252 Y. J. Hwang, C. Hahn, B. Liu and P. Yang, *ACS Nano*, 2012, **6**, 5060–5069.

253 F. Le Formal, N. Tétreault, M. Cornuz, T. Moehl, M. Grätzel and K. Sivula, *Chem. Sci.*, 2011, **2**, 743.

254 R. L. Spray, K. J. McDonald and K. S. Choi, *J. Phys. Chem. C*, 2011, **115**, 3497–3506.

255 J. Y. Kim, D. H. Youn, K. Kang and J. S. Lee, *Angew. Chemie - Int. Ed.*, 2016, **55**, 10854–10858.

256 F. Le Formal, N. Tétreault, M. Cornuz, T. Moehl, M. Grätzel and K. Sivula, *Chem. Sci.*, 2011, **2**, 737–743.

257 J. Y. Kim, D. H. Youn, K. Kang and J. S. Lee, *Angew. Chemie - Int. Ed.*, 2016, **128**, 11012–11016.

258 Y. Liang, T. Tsubota, L. P. A. Mooij and R. Van De Krol, *J. Phys. Chem. C*, 2011, **115**, 17594–17598.

259 C. Zachäus, F. F. Abdi, L. M. Peter and R. Van De Krol, *Chem. Sci.*, 2017, **8**, 3712–3719.

260 S. Byun, B. Kim, S. Jeon and B. Shin, *J. Mater. Chem. A*, 2017, **5**, 6905–6913.

261 S. Bera, S. A. Lee, C. M. Kim, H. Khan, H. W. Jang and S. H. Kwon, *Chem. Mater.*, 2018, **30**, 8501–8509.

262 S. Y. Chen, J. S. Yang and J. J. Wu, *ACS Appl. Energy Mater.*, 2018, **1**, 2143–2149.

263 S. Bai, K. Tian, J. C. Meng, Y. Zhao, J. Sun, K. Zhang, Y. Feng, R. Luo, D. Li and A. Chen, *J. Alloys Compd.*, , DOI:10.1016/j.jallcom.2020.156780.

264 J. Liu, J. Li, M. Shao and M. Wei, *J. Mater. Chem. A*, 2019, **7**, 6327–6336.

265 H. C. Chiu and C. S. Yeh, *J. Phys. Chem. C*, 2007, **111**, 7256–7259.

266 H. L. Tan, X. Wen, R. Amal and Y. H. Ng, *J. Phys. Chem. Lett.*, 2016, **7**, 1400–1405.

267 J. Yang, D. Wang, X. Zhou and C. Li, *Chem. - A Eur. J.*, 2013, **19**, 1320–1326.

268 Y. Lu, J. Su, J. Shi and D. Zhou, *ACS Appl. Energy Mater.*, , DOI:10.1021/acsaem.0c01474.

269 A. J. E. Rettie, H. C. Lee, L. G. Marshall, J. F. Lin, C. Capan, J. Lindemuth, J. S. McCloy, J. Zhou, A. J. Bard and C. B. Mullins, *J. Am. Chem. Soc.*, 2013, **135**, 11389–11396.

270 S. Zhou, R. Tang, L. Zhang and L. Yin, *Electrochim. Acta*, 2017, **248**, 593–602.

271 J. Zhao and F. E. Osterloh, *J. Phys. Chem. Lett.*, 2014, **5**, 782–286.

272 M. V. Malashchonak, E. A. Streltsov, D. A. Kuliomin, A. I. Kulak and A. V. Mazanik, *Mater. Chem. Phys.*, 2017, **201**, 189–193.

6. APPENDIX A – Chapter 2

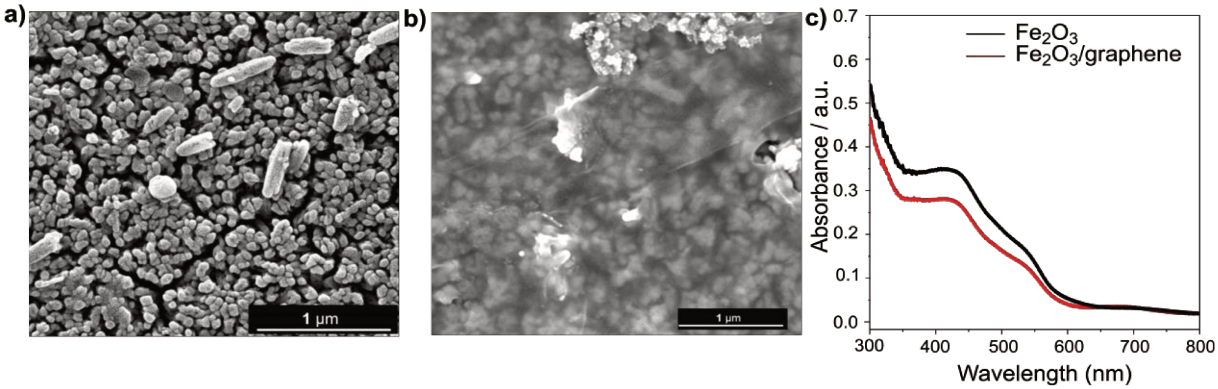


Figure A1: Top-view FEG-SEM images of a) the vertically oriented α-Fe_2O_3 and b) α-Fe_2O_3/graphene films; c) UV-Vis spectra of α-Fe_2O_3 and α-Fe_2O_3/graphene films.

APPENDIX B – Chapter 3

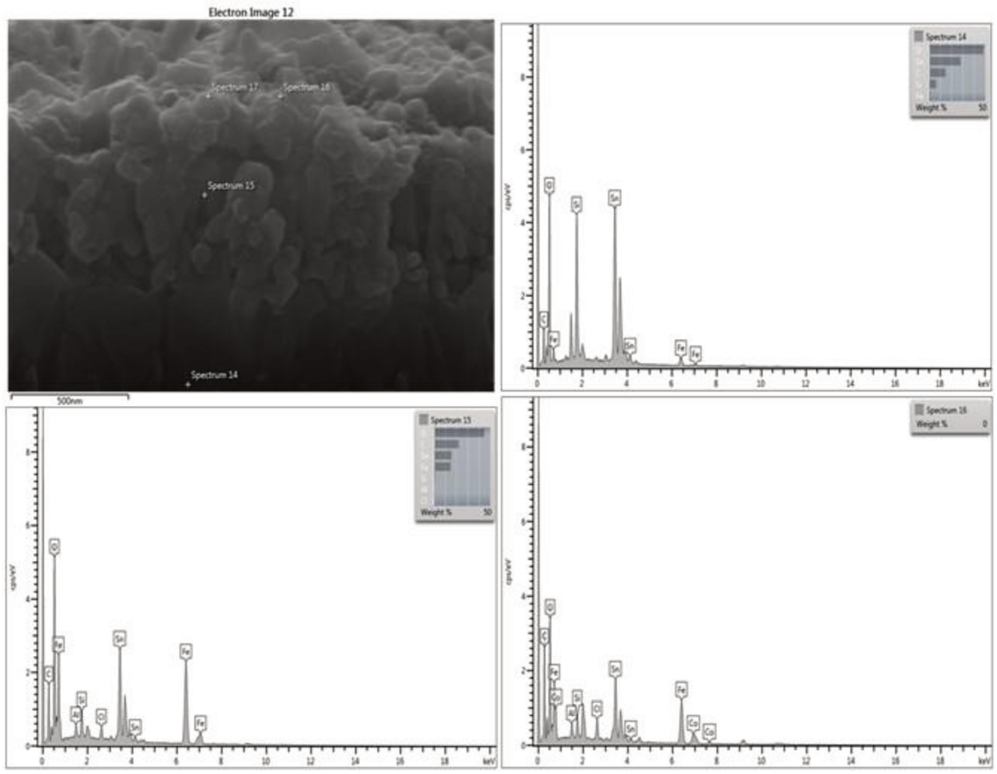


Figure B1: EDX spectra of α-Fe_2O_3/Co^{II}-NC-Fe^{II} at different regions of the cross-sectional profile.

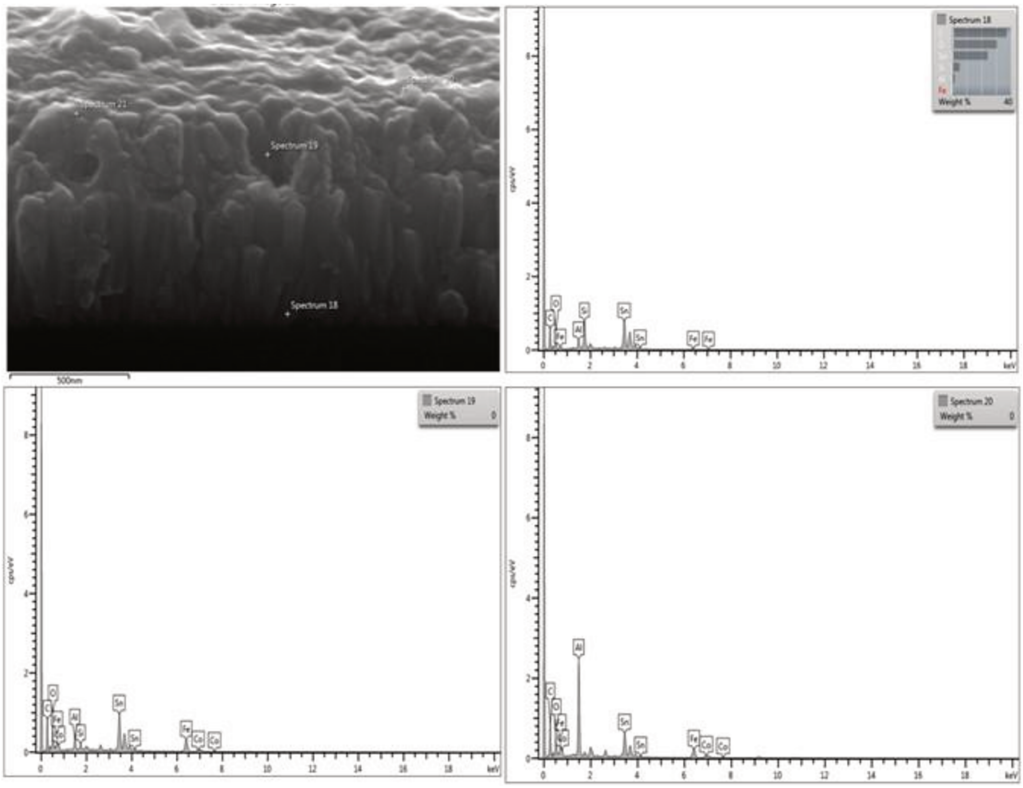


Figure B2: EDX spectra of α-Fe_2O_3/Co^{II}-NC-Fe^{III} at different regions of the cross-sectional profile.

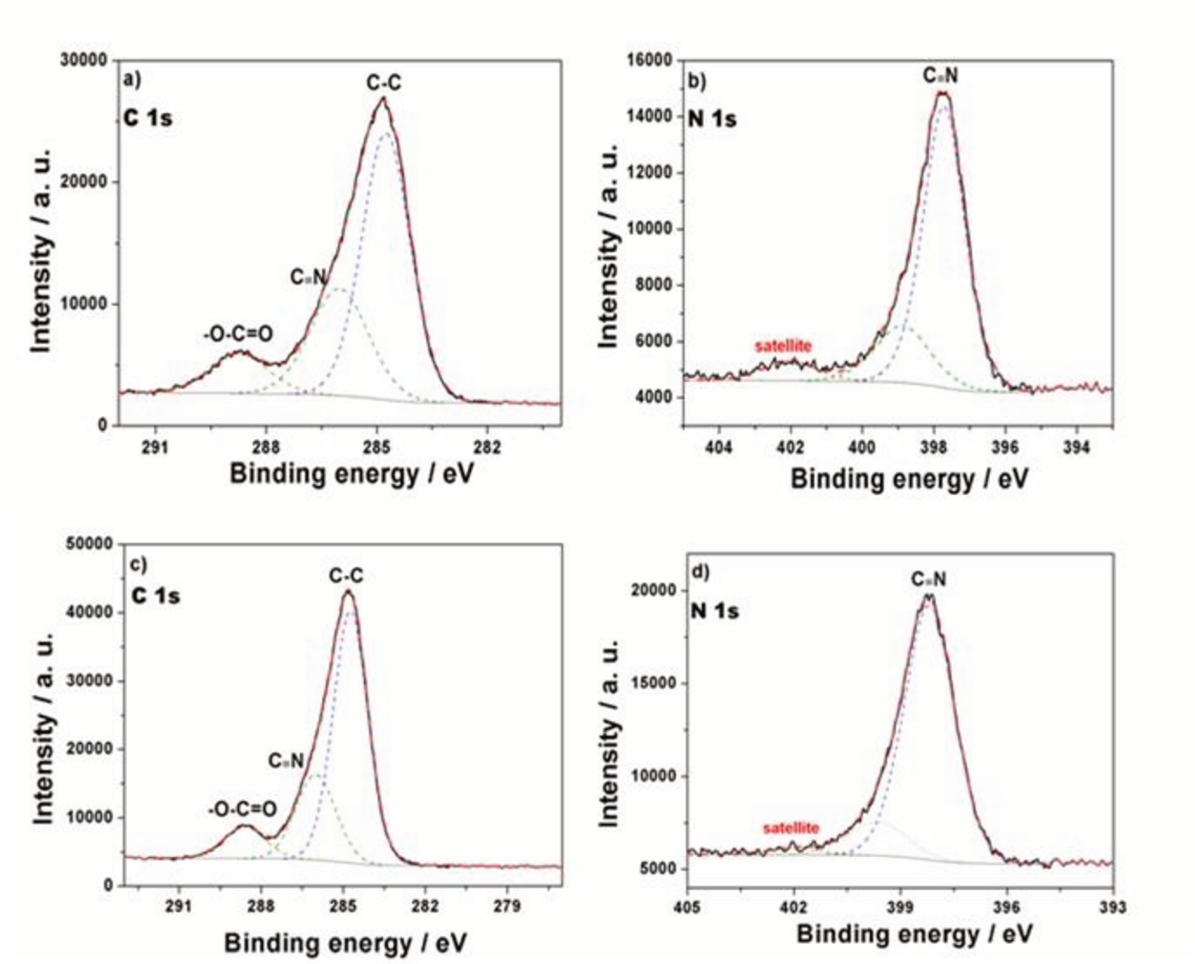


Figure B3: XPS spectra of α-Fe_2O_3/Co^{II}-NC-Fe^{II}: a) C 1s and b) N 1s and α-Fe_2O_3/Co^{II}-NC-Fe^{III}: c) C 1s and d) N 1s.

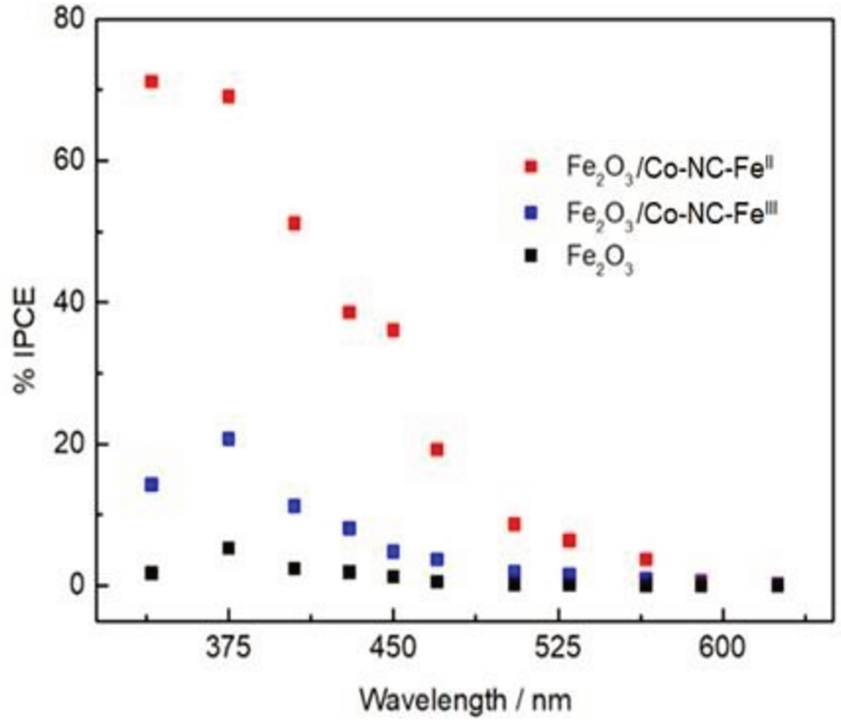


Figure B4: IPCE plots of α-Fe_2O_3, α-Fe_2O_3/Co-NC-Fe^{II}, α-Fe_2O_3/Co-NC-Fe^{III} photoanodes recorded at 0.62 V vs Ag/AgCl in 0.1 M KPi aqueous solution.

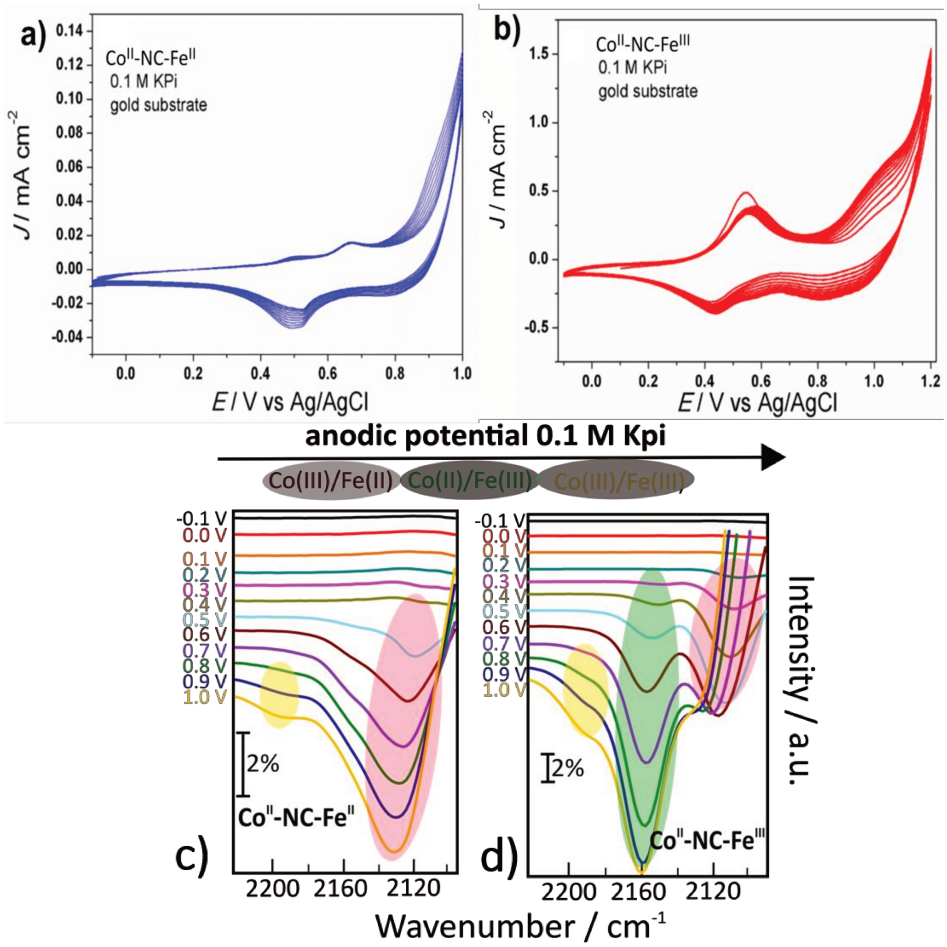


Figure B5: Cyclic voltammograms in the dark of a) Co^{II}-NC-Fe^{II} and Co^{II}-NC-Fe^{III} All measurents were carried out on gold substrates; *In-situ* FTIR spectra of c) Co^{II}-NC-Fe^{II} and d) Co^{II}-NC-Fe^{III}. The spectra were recorded in the dark from -0.1 to 1.0 V vs Ag/AgCl (1 mV s^{-1}). CV and in-situ FTIR measurements were carried out in 0.1 M KPi.

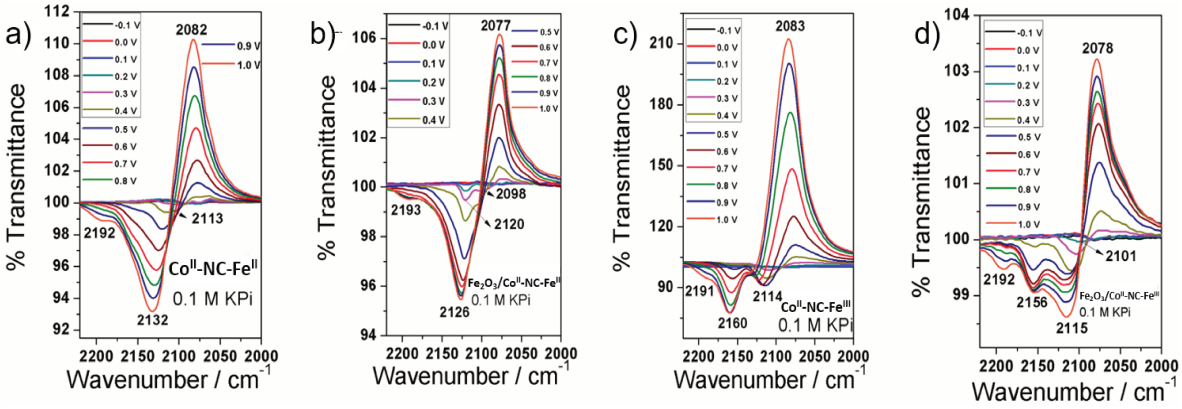


Figure B6: *In-situ* FTIR spectra of a) Co^{II}-NC-Fe^{II}, b) α-Fe_2O_3/Co^{II}-NC-Fe^{II}, c) Co^{II}-NC-Fe^{III} and d) α-Fe_2O_3/Co^{II}-NC-Fe^{III} in 0.1 M KPi. All the spectra were recorded in the range of 2200-2000 cm^{-1}. The negative signals correpond to formed oxidized species whereas positive signals correspond to consumed species as function of applied bias.

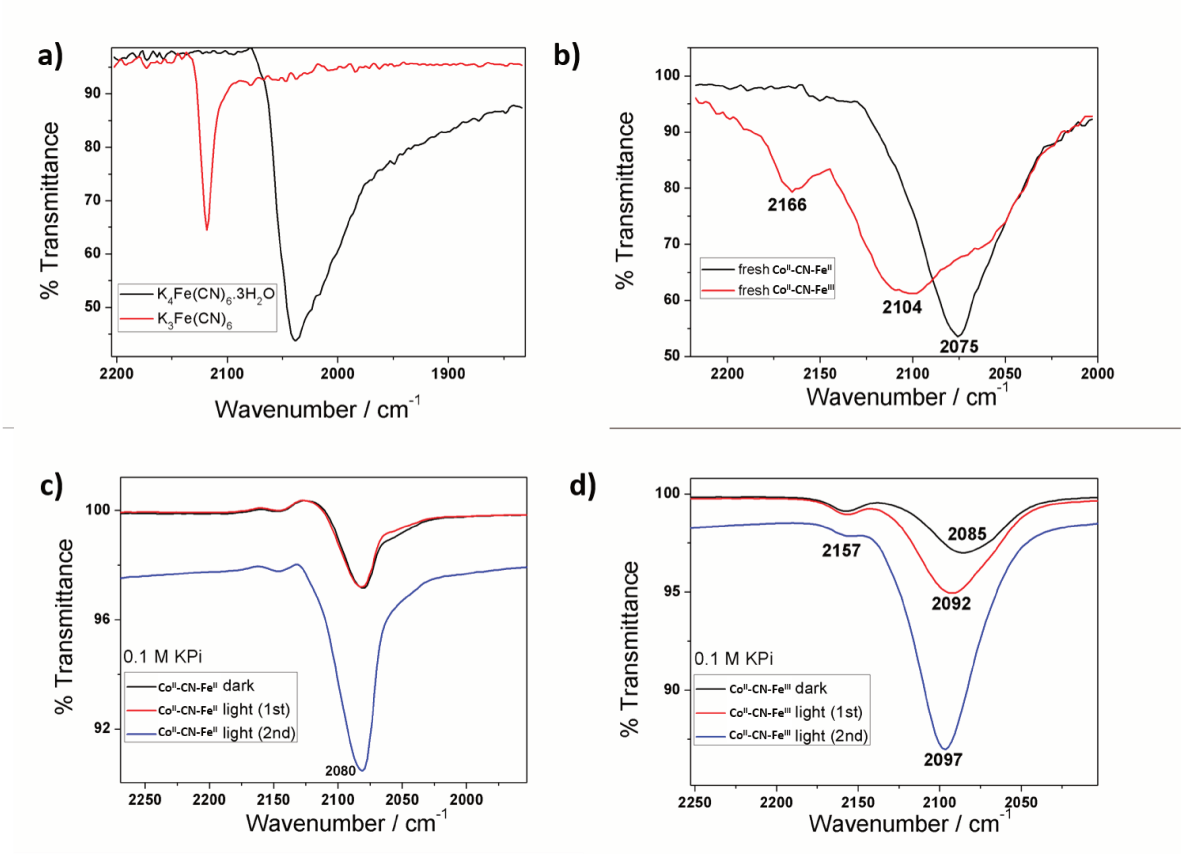


Figure B7: FTIR spectra of the a) $K_3Fe(CN)_6$ and $K_4Fe(CN)_6.3H_2O$ precursors salts depicting the formation of Co^{III}/Fe^{II} at lower potentials b) Co^{II}-NC-Fe^{II} and c) Co^{II}-NC-Fe^{III} in the dark and under light illumination in the absence of applied bias.

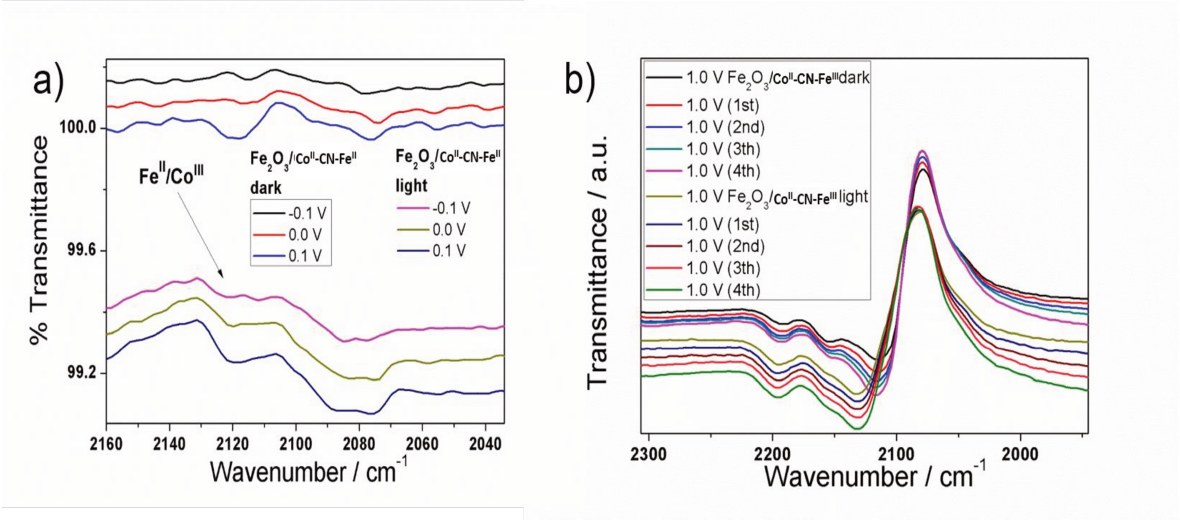


Figure B8: In-situ FTIR spectra of a) α-Fe_2O_3/Co^{II}-NC-Fe^{II} depicting the formation of Co^{III}/Fe^{II} at lower potentials and of b) α-Fe_2O_3/Co^{II}-NC-Fe^{III} at 1.0 V with 5 subsequent spectra at the same potential.

APPENDIX C – Chapter 4

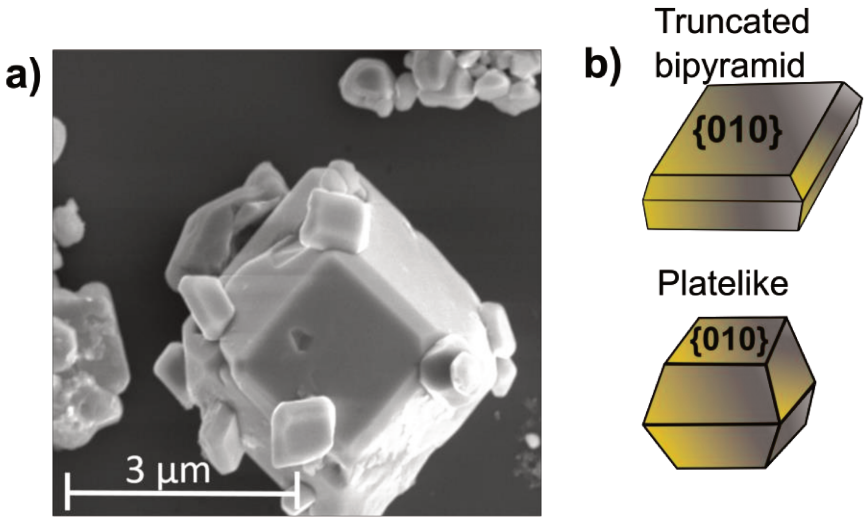


Figure C1: a) FEG-SEM image of the as-prepared $BiVO_4$ and b) schematic illustration of the truncated bipyramid and platelike geometries of $BiVO_4$ with their {010} exposed facet.

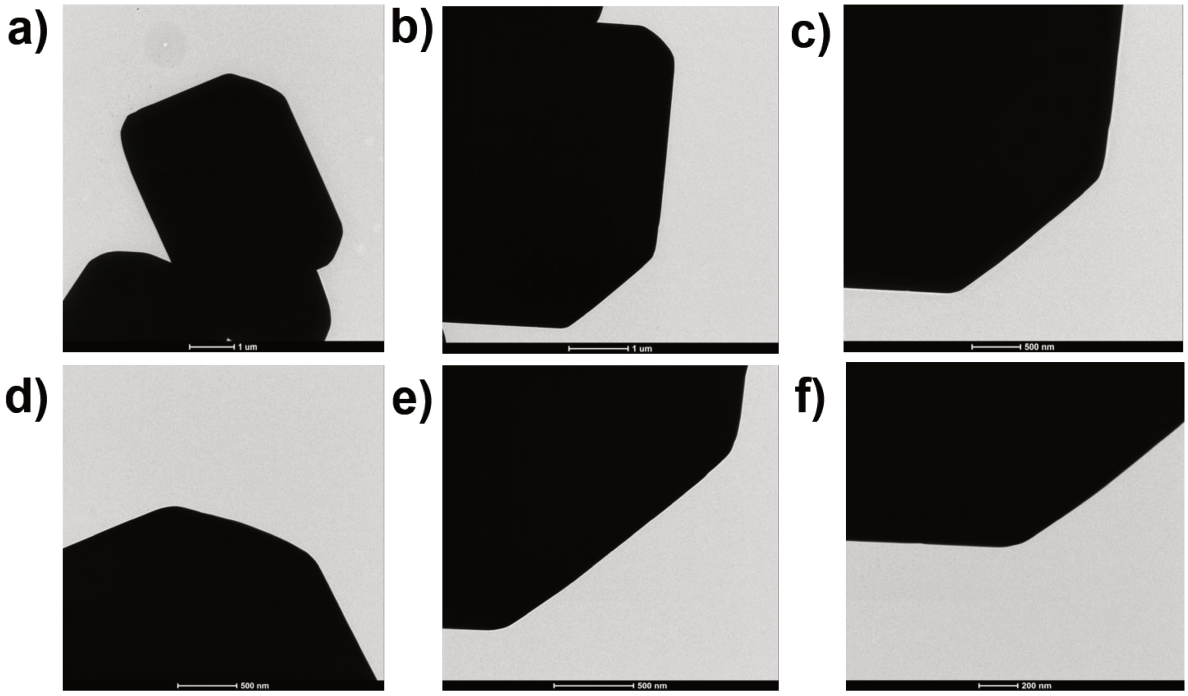


Figure C2: (a-f) TEM images of unmodified $BiVO_4$ depiciting its smooth surface.

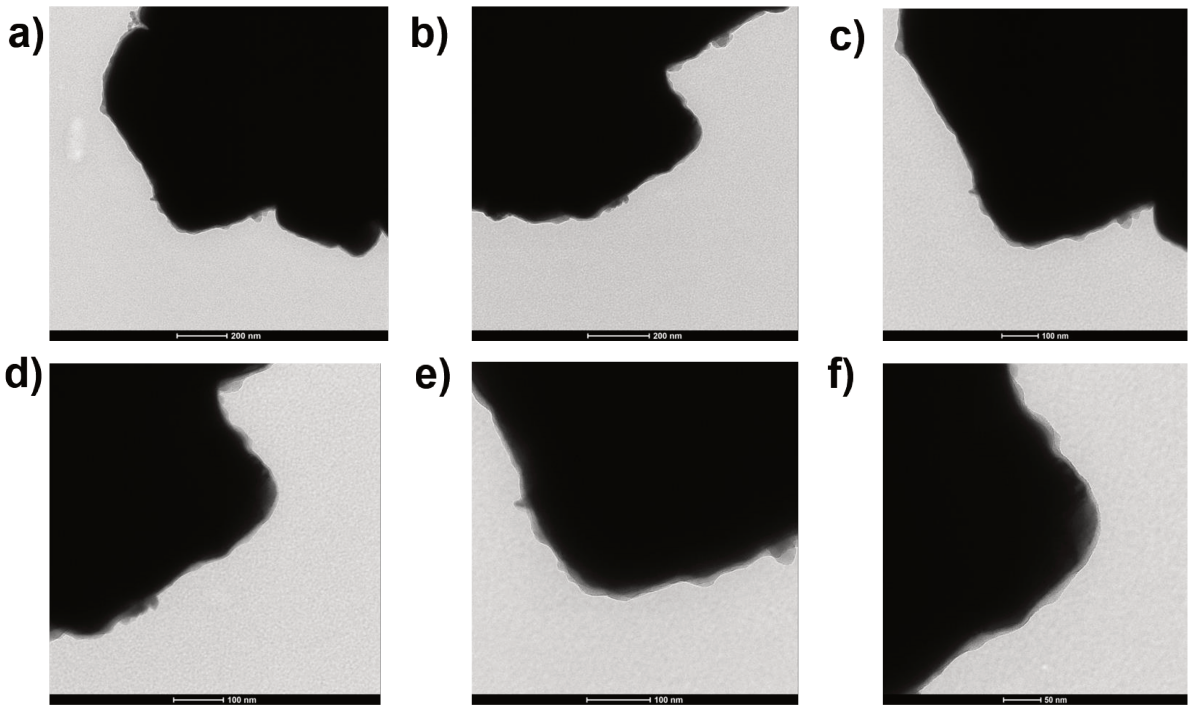


Figure C3: (a-f) TEM images of $BiVO_4$@SnO_2 3% depiciting the thin SnO_2 conformal layer over $BiVO_4$ surface.

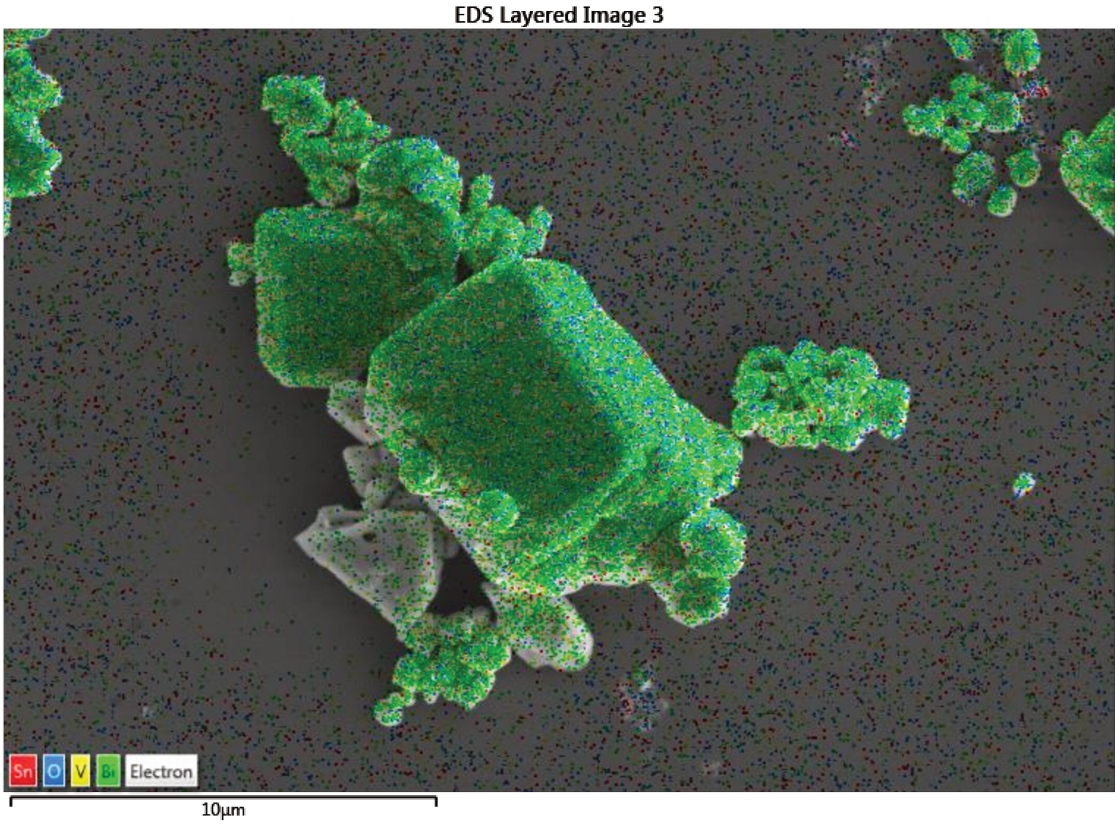


Figure C4: FEG-SEM image combined with EDX for element mapping on $BiVO_4$@SnO_2 3% photocatyst.

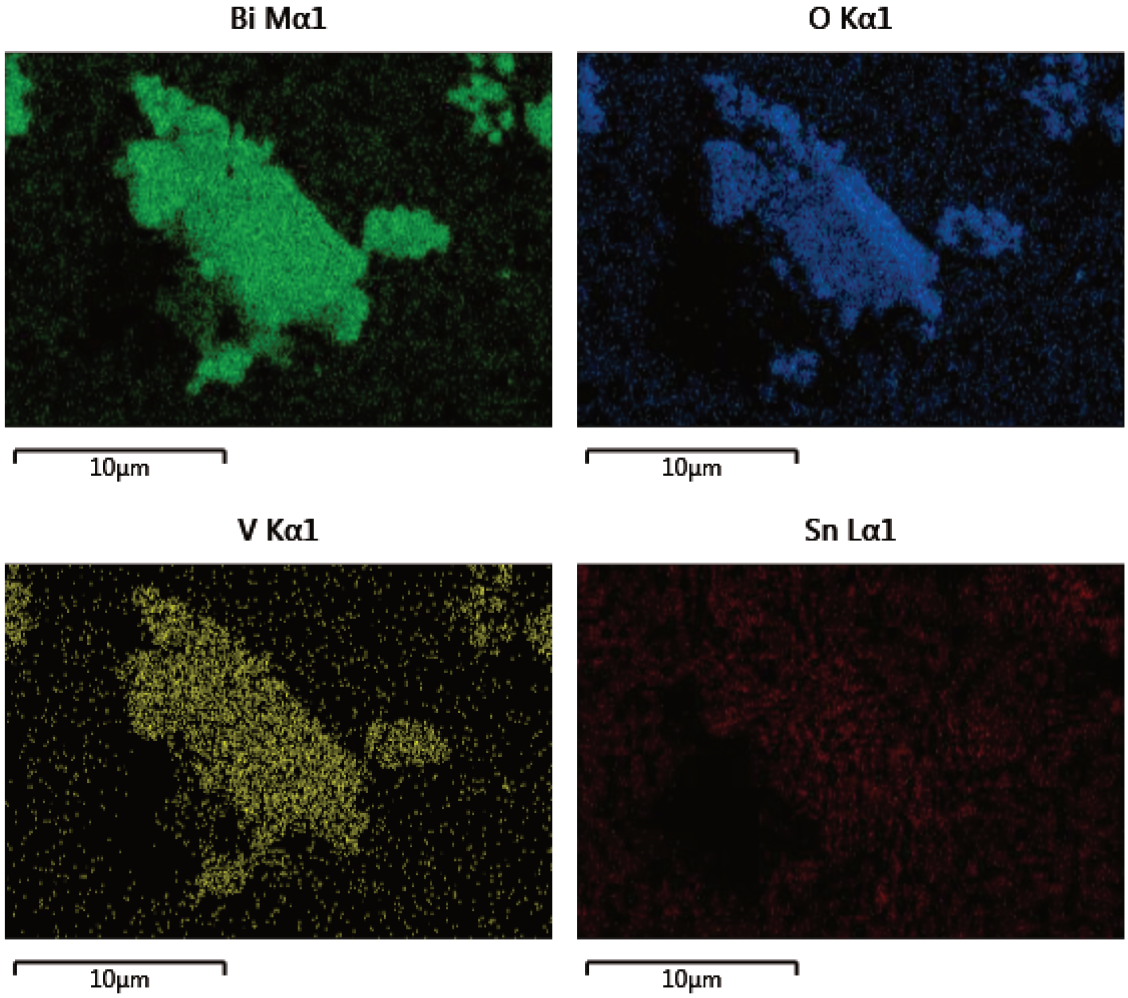


Figure C5: Related element mapping images for Bi, O, V and Sn atoms of $BiVO_4$@SnO_2 3% photocatalyst.